Solid-State NMR Studies on Local and Aggregated Structures of Organic Semiconductor Materials

Tatsuya Fukushima

2013

Contents

Chapter 3

Preparation of Green- and Blue-Emitting Tris(8-hydroxyquinoline) aluminum(III) (Alq_3) Crystalline Polymorphs and Application to Organic Light-Emitting Diodes

Chapter 4

Sensitivity Enhancement in Solid-State NMR of Organic Thin-Film Semiconductors by a Paramagnetic System

Chapter 1

General Introduction

1.1. Backgrounds

Organic electronics such as organic light-emitting diodes (OLEDs) and organic solar cells (OSCs) consisting of organic semiconductor films have attractive features such as lightweight property, flexibility, and low cost productivity not shared by electronics based on inorganic materials. Therefore, the organic electronics are a promising new technology and have been studied energetically [1-59]. Study on electrical conductivity in organic compounds has been reported since early 1900s [1-4]. In 1950, Akamatsu and Inokuchi [5] reported the electrical conductivity of purified violanthrone, iso-violanthrone, and pyranthrone (Fig. 1.1). The three materials are simple organic compounds, and the molecular structures of the materials are similar to those of recently-used materials in organic electronics. Inokuchi also reported the electrical conductivity of other polycyclic aromatic compounds [6-8]. In 1954, Akamatsu et al. [9] found that a complex consisting of perylene (Fig. 1.1) and bromine have good

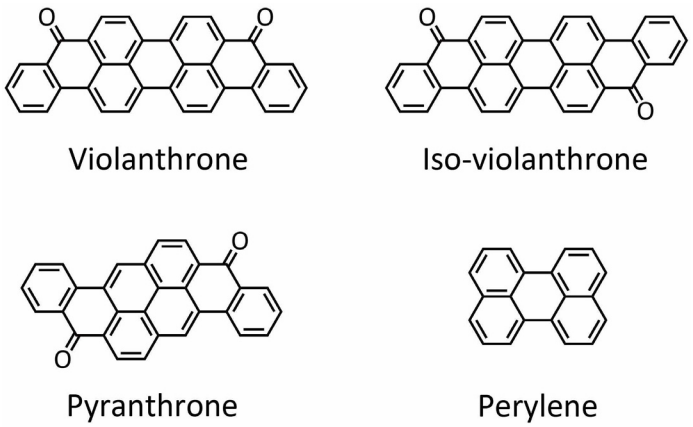

Fig. 1.1. Chemical structures of organic semiconductor materials: violanthrone, iso-violanthrone, pyranthrone, perylene.

electrical conductivity ($1–10^{-3}$ $\Omega^{-1}\cdot cm^{-1}$). Ten years later, Helfrich and Schneider reported electroluminescence (EL) of anthracene crystal (Fig. 1.2) from singlet excitons induced by injected positive and negative charges under high voltages (> 250 V) [11]. Vincett et al. decreased the driving voltage of EL by depositing an anthracene layer with the film thickness of 600 nm, but still, the driving voltage was as high as 30 V [12]. In 1987, Tang and VanSlyke achieved a remarkable breakthrough for OLEDs. The device was composed of amorphous thin-film bilayers; a hole-transport material, 1,1-bis[(di-4-tolylamino)phenyl]cyclohexane (TAPC, Fig. 1.2), and a bifunctional electron-transport and light-emitting material, tris(8-hydroxyquinoline) aluminum(III) (Alq_3). The device with the total thickness of 135 nm provided brightness over 1000 cd/m^2 with the driving voltage below 10 V [14]. In 1988, Adachi et al. proposed a three-layered structure, consisting of a hole-transport material

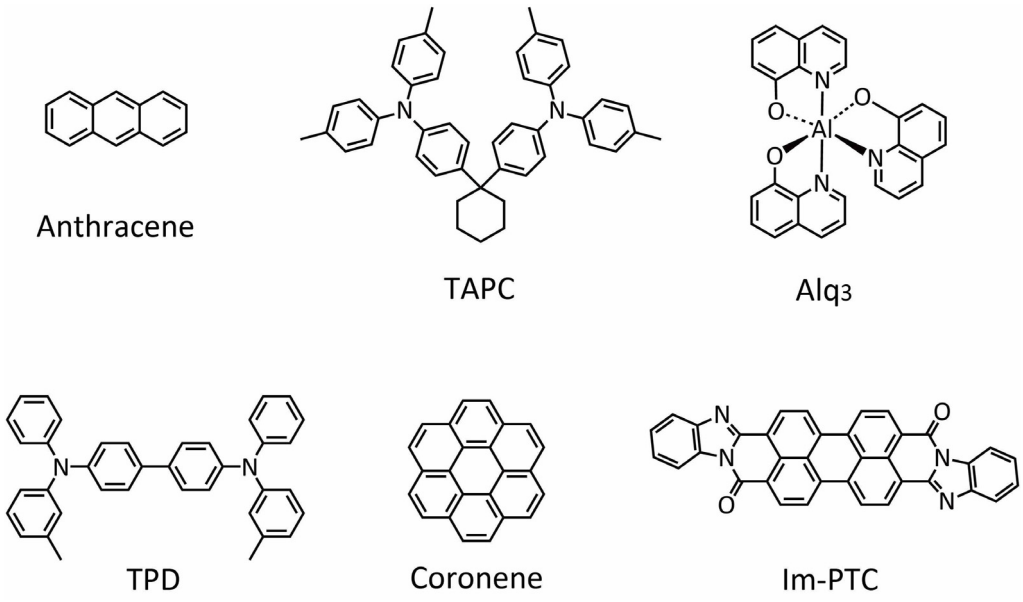

Fig. 1.2. Chemical structures of organic semiconductor materials: anthracene, 1,1-bis[(di-4-tolylamino)phenyl]cyclohexane (TAPC), tris(8-hydroxyquinoline) aluminum(III) (Alq_3), *N,N'*-diphenyl-*N,N'*-di(*m*-tolyl)benzidine (TPD), coronene, and perylene-3,4,9,10-tetracarboxyl-bis-benzimidazole (Im-PTC).

(*N*,*N*'-diphenyl-*N*,*N*'-di(m-tolyl)benzidine, TPD), a light-emitting material (anthracene, coronene, or perylene), and an electron-transport material (perylene-3,4,9,10-tetracarboxyl-bis-benzimidazole, Im-PTC) [15]. The chemical structures of the materials are shown in Fig.1.2.

On OSCs, Kearns and Calvin reported a photovoltaic effect in organic systems composed of magnesium phthalocyanine (MgPc, Fig. 1.3) disks coated with a thin film of air-oxidized tetramethyl *p*-phenylenediamine (TMPD) in 1958 [10]. In 1986, Tang fabricated a OSC with power conversion efficiency (PCE) of about 1 %, which has a two-layered thin films composed of a copper phthalocyanine (CuPc, Fig. 1.3) and the Im-PTC, by vacuum-deposition [13]. The device structure was followed by a new type of three-layered cells, consisting of an *n*-type pigment (Im-PTC or Me-PTC in Figs. 1.2 and 1.3, respectively), an interlayer (co-deposition of a PTC derivative and phthalocyanine, H_2Pc, in Fig. 1.3), and a *p*-type pigment (H_2Pc), proposed by Hiramoto et al. in 1991 [19]. In 1995, Yu et al. reported a bulk-heterojunction (BHJ) OSC composed of a π-conjugated polymer and a fullerene derivative [21]. This polymer-based BHJ OSC has been widely studied because of the high performances and easy wet-fabrication

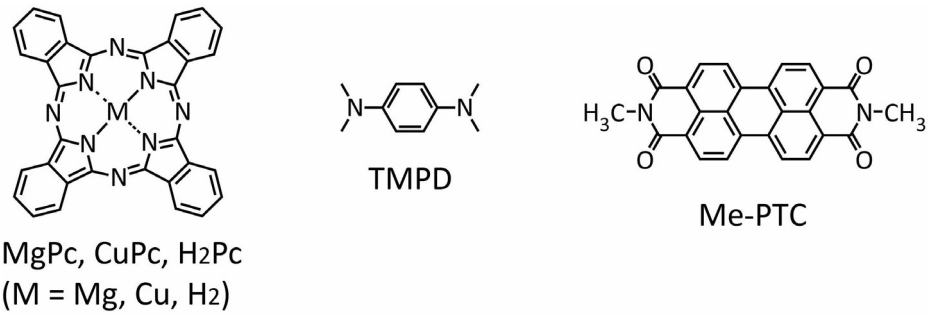

Fig. 1.3. Chemical structures of organic semiconductor materials: phthalocyanine derivatives (MgPc, CuPc, H_2Pc), tetramethyl *p*-phenylenediamine (TMPD), and *N*-methyl-3,4,9,10-perylenetetracarboxyl-diimide (Me-PTC).

processes [32,33,39,43,47-49,52,56,57]. As shown above, performances of organic electronics have been developed steadily by investigations not only of organic semiconductor materials but also of device structures.

In organic electronics, charges are transferred through intermolecular orbital overlaps by hopping mechanism [60-62].

$$M_A + M_B^+ \rightarrow M_A^+ + M_B \quad (1.1)$$

$$M_A + M_B^- \rightarrow M_A^- + M_B \quad (1.2)$$

According to Marcus theory, the rate constant, k_{CT}, for intermolecular hopping charge-transfer process, are expressed as [60, 61]

$$k_{CT} = \frac{4\pi^2}{h} H_{AB}^2 \frac{1}{\sqrt{4\pi\lambda k_B T}} \exp\left[-\frac{(\Delta G_{if} + \lambda)^2}{4\lambda k_B T} \right], \quad (1.3)$$

where H_{AB} is the charge transfer integral, λ is the reorganization energy, and ΔG_{if} is the free energy difference between the initial and final states. The T, h and k_B are the temperature, the Planck constant, and the Boltzmann constant, respectively. When the molecules M_A and M_B in Eqs. 1.1 and 1.2 are the same species, ΔG_{if} is equal to 0. Then, Eq. 1.3 reduces to Eq. 1.4.

$$k_{CT} = \frac{4\pi^2}{h} H_{AB}^2 \frac{1}{\sqrt{4\pi\lambda k_B T}} \exp\left(-\frac{\lambda}{4 k_B T} \right). \quad (1.4)$$

According to Eq. 1.4, the charge-transfer rate constant is a function of the charge transfer

integral and the reorganization energy at a given temperature, and it is expected that the intra- and intermolecular structures in organic thin films are closely related to the hole/electron transporting property. Therefore, it is important to clarify the structures in order to understand the device performances.

Wide angle X-ray diffraction (WAXD) experiment is a representative method to analyze structures of materials. However, the structural analysis in organic materials is often difficult, when the materials have structural disorders. In addition, materials for organic electronics are mostly composed of carbon, nitrogen, and oxygen atoms as shown in Fig. 1.1–1.3. These atoms have similar atomic scattering factors and are difficult to distinguish with each other [63]. Solid-state nuclear magnetic resonance (NMR) is a complementary tool to study structures of organic materials and has been used for the structural analysis of disordered and amorphous materials [64-71]. The application of solid-state NMR to organic semiconductors is also expected to be highly useful [71-75].

1.2. Outline of This Thesis

The aim of this thesis is to analyze the structures of materials in organic semiconductors mainly by solid-state NMR in order to understand the performance of organic semiconductors. The contents of this thesis are as follows.

In Chapter 2, the local structure of Alq_3 in three crystalline polymorphs, α-, γ-, and δ-Alq_3, and melt-quenched amorphous Alq_3 (amorphous-Alq_3), are investigated by two-dimensional ^{27}Al multi-quantum magic-angle spinning (MQMAS) NMR experiments. The MQMAS experiments, which expand one-dimensional MAS NMR spectrum along a new isotropic (ISO) axis, enable precise determination of quadrupolar and chemical shift parameters including the distributions [76, 77]. These parameters reflect local structures of respective samples and it is

found that the γ- and δ-Alq_3 consist of the facial isomer with well-defined crystal structure, whereas the α- and amorphous-Alq_3 consist of the meridional isomer with distributions of quadrupolar coupling constants. It is also found that two distinct sites exist in α-Alq_3.

In Chapter 3, the effect of Alq_3 crystalline polymorphs as source powders on OLED performance is investigated. First, the temperature change in the crystalline forms of α-Alq_3 and δ-Alq_3 is investigated by WAXD experiments in a vacuum. It is found that α-Alq_3 remains in α-form up to 300 °C, immediately before sublimation. In contrast, δ-Alq_3 is found to transform into γ-form at ~180 °C, and remain in γ-form up to 300 °C, immediately before sublimation. Both δ-Alq_3 and γ-Alq_3 are composed of facial isomers and emit blue photoluminescence (PL), which is different from the typical green emissions of α-Alq_3. Second, OLEDs are fabricated from different Alq_3 crystals as source powders; i.e., from 1) α-Alq_3, 2) δ-Alq_3, and 3) a mixture of α-, γ-, and δ-Alq_3. All the OLEDs exhibit green electroluminescence (EL) with almost the same maximum wavelength, although the δ-Alq_3 source powder shows blue PL emission. This suggests that some facial isomers become meridional during the vacuum evaporation process. In contrast, EL efficiency depends on the Alq_3 crystalline polymorph; the OLED fabricated from the mixture of α-, γ-, and δ-Alq_3 has up to 1.4 times the EL efficiency of the OLED fabricated from α-Alq_3 for the same device structure.

In Chapter 4, sensitivity enhancements in solid-state NMR spectra of organic thin-film semiconductors by paramagnetic dopant layers are investigated. One reason for low sensitivity of NMR is the slow relaxation process of nuclear spin systems, which is determined by the longitudinal relaxation time (T_1). To overcome this issue, paramagnetic relaxation reagents have been often used to reduce T_1 relaxation time in solution NMR [78-82]. On the other hand, a paramagnetic dopant is less effective in solid-state NMR. In solid samples, nuclei, which are

close to paramagnetic species, show significant line-broadening because of dipolar shift and paramagnetic relaxation. By contrast, nuclei, which are distant from paramagnetic centers, show almost no reduction of their T_1 relaxation time. These are the reasons why only a small number of solid-state NMR studies have been reported [83-85]. In this chapter, the sensitivity enhancement in solid-state NMR of organic thin-film semiconductor samples by paramagnetic dopant layers assisted by ^{1}H–^{1}H spin diffusion is reported. It is found that a vacuum-deposited paramagnetic dopant, CuPc (Fig. 1.3), on a phenyldipyrenylphosphine oxide ($POPy_2$) films effectively reduces ^{1}H T_1 relaxation time of $POPy_2$ films by using H–^{1}H spin diffusion, enabling faster repetition of NMR measurements. When the thickness of the $POPy_2$ films is between 50 and 100 nm, ^{1}H spins are well polarized by ^{1}H–^{1}H spin diffusion, giving the maximum sensitivity without harmful effects such as paramagnetic shift, broadening, and quenching of cross-polarization (CP)/MAS signals. The binary films consisting of CuPc and $POPy_2$ show a threefold reduction of the NMR measurement time.

In chapter 5, the influence of formation conditions of a self-assembled monolayer (SAM) on ITO on the device performance of OLEDs is investigated. Pentyltriethoxysilane (PTES) and tetrahydrofuran (THF) were used as a surface modifier and a solvent, respectively. The immobilization of PTES on the ITO substrate was performed under both the acidic and basic conditions with various H_2O/PTES ratios, r. The relationship between the resultant SAM structure and the hole-injection property was investigated by using hole only devices (HODs) fabricated on the SAM-modified ITO substrates. It was found that the catalytic condition, the value of r, and the concentration of PTES in THF, C_{PTES}, highly influence the structure of SAM, and thus affect the hole-injection property of the HOD. The SAM formation under the acidic conditions allows homogeneous coverage of a silane layer on the ITO surface, which leads to the improved hole-injection from the anode. On the other hand, the use of basic catalysts

results in the inhomogeneous coverage of a silane layer on the ITO surface and the decreased hole-injection from the anode. The choice of r and C_{PTES} also affect the kinetics of hydrolysis and condensation reactions of PTES, and hence affect the resultant SAM structure and hole-injection property. The results obtained here show that the device performance can be improved drastically by choosing the SAM formation conditions appropriately.

In chapter 6, the origin of the improvement in PCE by the thermal annealing of BHJ OSCs, based on regioregular poly(3-hexylthiophene-2,5-diyl) (rrP3HT) and [6,6]-phenyl-C_{61}-butyric acid methyl ester ($PC_{61}BM$), is analyzed by solid-state NMR. Photoelectric conversion occurs via generation of excitons through the absorption of light, diffusion of excitons toward donor/acceptor interfaces, charge separation at the interfaces and formation of free carriers (hole and electrons), and transport of free carriers toward electrodes. These processes occur at different size scales. Therefore, the analysis of the donor-acceptor structures at hierarchical levels is important to understand the device performance. ^{1}H spin-lattice relaxation experiments in the rotating frame ($T_{1\rho H}$) and the laboratory frame (T_{1H}) in solid-state NMR reveal miscibility on the order of several nanometers and that of several tens of nanometers, respectively. $T_{1\rho H}$ experiments show that rrP3HT and $PC_{61}BM$ are already phase-separated in nonannealed sample on the order of several nanometers. The structures in this size scale do not change significantly with annealing. In contrast, it is found from T_{1H} experiments that the phase-separated structure develops on the order of several tens of nanometers in rrP3HT/$PC_{61}BM$ blend films with thermal annealing at 150 ºC. The increase of the PCE for OSCs from 0.7 % to nearly 3 % by annealing can be explained by the phase-separation.

In Chapter 7, the effect of alkyl-side chain lengths of donor polymers on PCE of BHJ OSCs and the BHJ structures during isothermal annealing is investigated. As donor polymers, regioregular poly(3-alkylthiophene-2,5-diyl) (rrP3AT) with butyl, hexyl, and dodecyl side-chain,

regioregular poly(3-butylthiophene-2,5-diyl) (rrP3BT), rrP3HT, and regioregular poly(3-dodecylthiophene-2,5-diyl) (rrP3DDT), were used. For OSCs in the rrP3BT/$PC_{61}BM$ system, the PCE increases from 0.08 to 0.32 % by 5 min of annealing at 150 ºC. The PCE remains unchanged by prolonged annealing up to 30 min. However, the PCE is found to increase by further annealing; from 0.33 to 0.91 % by 45 min of annealing. Different from the two stage increase of PCEs for the rrP3BT/$PC_{61}BM$ system, the rrP3HT/$PC_{61}BM$ system provides only one stage increase (from 0.38 to 2.18 % by 5 min of annealing). The rrP3DDT/$PC_{61}BM$ system does not show any increase of PCEs; on the contrary, decrease from 0.33 to 0.10 % by 5 min of annealing. These changes of the PCEs mainly originate from the changes of a short-circuit current density. To understand the above results, the structural changes in the BHJ layer of the three OSC systems are analyzed by WAXD, UV-vis absorption, and solid-state NMR measurements. From these measurements, it is found that the structural ordering of rrP3AT and $PC_{61}BM$, and the phase-separated structures between rrP3AT and $PC_{61}BM$ on the order of several tens of nanometers are crucial factors to determine the performance of BHJ OSCs.

References

[1] C.A. Hansen, Trans. Am. Electrochem. Soc., 16 (1909) 329.

[2] E. Ryschewitsch, Zeits. f. Elektrochemie, 29 (1923) 474.

[3] J. Brunner, H. Hammerschmid, Zeits. f. Elektrochemie, 40 (1934) 60.

[4] P.R. Wallace, Phys. Rev., 71 (1947) 622.

[5] H. Akamatu, H. Inokuchi, J. Chem. Phys., 18 (1950) 810.

[6] H. Inokuchi, Bull. Chem. Soc. Jpn., 24 (1951) 222.

[7] H. Inokuchi, Bull. Chem. Soc. Jpn., 25 (1952) 28.

[8] H. Inokuchi, Bull. Chem. Soc. Jpn., 27 (1954) 22.

[9] H. Akamatu, H. Inokuchi, Y. Matsunaga, Nature, 173 (1954) 168.

[10] D. Kearns, M. Calvin, J. Chem. Phys., 29 (1958) 950.

[11] W. Helfrich, W.G. Schneider, J. Chem. Phys., 44 (1966) 2902.

[12] P.S. Vincett, W.A. Barlow, P.A. Hann, G.G. Roberts, Thin Solid Films, 94 (1982) 171.

[13] C.W. Tang, Appl. Phys. Lett., 48 (1986) 183.

[14] C.W. Tang, S.A. VanSlyke, Appl. Phys. Lett., 51 (1987) 913.

[15] C. Adachi, S. Tokito, T. Tsutsui, S. Saito, Jpn. J. Appl. Phys., 27 (1988) L269.

[16] C. Adachi, S. Tokito, T. Tsutsui, S. Saito, Jpn. J. Appl. Phys., 27 (1988) L713.

[17] J.H. Burroughes, D.D.C. Bradley, A.R. Brown, R.N. Marks, K. Mackay, R.H. Friend, P.L. Burns, A.B. Holmes, Nature, 347 (1990) 539.

[18] Y. Ohmori, M. Uchida, K. Muro, K. Yoshino, Jpn. J. Appl. Phys., 30 (1991) L1941.

[19] M. Hiramoto, H. Fujiwara, M. Yokoyama, Appl. Phys. Lett., 58 (1991) 1062.

[20] A.R. Brown, D.D.C. Bradley, J.H. Burroughes, R.H. Friend, N.C. Greenham, P.L. Burn, A.B. Holmes, A. Kraft, Appl. Phys. Lett., 61 (1992) 2793.

[21] G. Yu, J. Gao, J.C. Hummelen, F. Wudl, A.J. Heeger, Science, 270 (1995) 1789.

[22] Y. Shirota, J. Mater. Chem., 10 (2000) 1.

[23] S.E. Shaheen, C.J. Brabec, N.S. Sariciftci, F. Padinger, T. Fromherz, J.C. Hummelen, Appl. Phys. Lett., 78 (2001) 841.

[24] A. Kohler, J.S. Wilson, R.H. Friend, Adv. Mater., 14 (2002) 701.

[25] M. Hiramoto, K. Suemori, M. Yokoyama, Jpn. J. Appl. Phys., 41 (2002) 2763.

[26] B.W. D'Andrade, S.R. Forrest, Adv. Mater., 16 (2004) 1585.

[27] J. Xue, S. Uchida, B.P. Rand, S.R. Forrest, Appl. Phys. Lett., 84 (2004) 3013.

[28] S.J. Yeh, M.F. Wu, C.T. Chen, Y.H. Song, Y. Chi, M.H. Ho, S.F. Hsu, C.H. Chen, Adv. Mater., 17 (2005) 285.

[29] F. Yang, M. Shtein, S.R. Forrest, Nat. Mater., 4 (2005) 37.

[30] G. Li, V. Shrotriya, Y. Yao, Y. Yang, J. Appl. Phys., 98 (2005).

[31] J. Huang, G. Li, E. Wu, Q. Xu, Y. Yang, Adv. Mater., 18 (2006) 114.

[32] Y. Kim, S. Cook, S.M. Tuladhar, S.A. Choulis, J. Nelson, J.R. Durrant, D.D.C. Bradley, M. Giles, I. McCulloch, C.-S. Ha, M. Ree, Nat. Mater., 5 (2006) 197.

[33] D. Mühlbacher, M. Scharber, M. Morana, Z. Zhu, D. Waller, R. Gaudiana, C. Brabec, Adv. Mater., 18 (2006) 2884.

[34] M.C. Scharber, D. Mühlbacher, M. Koppe, P. Denk, C. Waldauf, A.J. Heeger, C.J. Brabec, Adv. Mater., 18 (2006) 789.

[35] J. Huang, T. Watanabe, K. Ueno, Y. Yang, Adv. Mater., 19 (2007) 739.

[36] Y. Shirota, H. Kageyama, Chem. Rev., 107 (2007) 953.

[37] P.W.M. Blom, V.D. Mihailetchi, L.J.A. Koster, D.E. Markov, Adv. Mater., 19 (2007) 1551.

[38] J.Y. Kim, K. Lee, N.E. Coates, D. Moses, T.Q. Nguyen, M. Dante, A.J. Heeger, Science, 317 (2007) 222.

[39] L.H. Nguyen, H. Hoppe, T. Erb, S. Günes, G. Gobsch, N.S. Sariciftci, Adv. Funct. Mater.,

17 (2007) 1071.

[40] J. Peet, J.Y. Kim, N.E. Coates, W.L. Ma, D. Moses, A.J. Heeger, G.C. Bazan, Nat. Mater., 6 (2007) 497.

[41] M. Campoy-Quiles, T. Ferenczi, T. Agostinelli, P.G. Etchegoin, Y. Kim, T.D. Anthopoulos, P.N. Stavrinou, D.D. Bradley, J. Nelson, Nat. Mater., 7 (2008) 158.

[42] B.C. Thompson, J.M. Frechet, Angew. Chem., 47 (2008) 58.

[43] H.Y. Chen, J.H. Hou, S.Q. Zhang, Y.Y. Liang, G.W. Yang, Y. Yang, L.P. Yu, Y. Wu, G. Li, Nat. Photonics, 3 (2009) 649.

[44] S.H. Park, A. Roy, S. Beaupré, S. Cho, N. Coates, J.S. Moon, D. Moses, M. Leclerc, K. Lee, A.J. Heeger, Nat. Photonics, 3 (2009) 297.

[45] J. Wagner, M. Gruber, A. Hinderhofer, A. Wilke, B. Bröker, J. Frisch, P. Amsalem, A. Vollmer, A. Opitz, N. Koch, F. Schreiber, W. Brütting, Adv. Funct. Mater., 20 (2010) 4295.

[46] K.T. Kamtekar, A.P. Monkman, M.R. Bryce, Adv. Mater., 22 (2010) 572.

[47] H.Y. Chen, J.H. Hou, A.E. Hayden, H. Yang, K.N. Houk, Y. Yang, Adv. Mater., 22 (2010) 371.

[48] M.C. Scharber, M. Koppe, J. Gao, F. Cordella, M.A. Loi, P. Denk, M. Morana, H.J. Egelhaaf, K. Forberich, G. Dennler, R. Gaudiana, D. Waller, Z.G. Zhu, X.B. Shi, C.J. Brabec, Adv. Mater., 22 (2010) 367.

[49] H.X. Zhou, L.Q. Yang, S.C. Price, K.J. Knight, W. You, Angew. Chem., Int. Ed., 49 (2010) 7992.

[50] M.C. Gather, A. Koehnen, K. Meerholz, Adv. Mater., 23 (2011) 233.

[51] L. Xiao, Z. Chen, B. Qu, J. Luo, S. Kong, Q. Gong, J. Kido, Adv. Mater., 23 (2011) 926.

[52] Z. He, C. Zhong, X. Huang, W.Y. Wong, H. Wu, L. Chen, S. Su, Y. Cao, Adv. Mater., 23 (2011) 4636.

[53] L.Y. Lin, Y.H. Chen, Z.Y. Huang, H.W. Lin, S.H. Chou, F. Lin, C.W. Chen, Y.H. Liu, K.T. Wong, J. Am. Chem. Soc., 133 (2011) 15822.

[54] H. Hoppe, N.S. Sariciftci, J. Mater. Res., 19 (2011) 1924.

[55] L.Y. Lin, Y.H. Chen, Z.Y. Huang, H.W. Lin, S.H. Chou, F. Lin, C.W. Chen, Y.H. Liu, K.T. Wong, J. Am. Chem. Soc., 133 (2011) 15822.

[56] H.X. Zhou, L.Q. Yang, A.C. Stuart, S.C. Price, S.B. Liu, W. You, Angew. Chem., Int. Ed., 50 (2011) 2995.

[57] T.Y. Chu, J. Lu, S. Beaupre, Y. Zhang, J.R. Pouliot, S. Wakim, J. Zhou, M. Leclerc, Z. Li, J. Ding, Y. Tao, J. Am. Chem. Soc., 133 (2011) 4250.

[58] K.S. Yook, J.Y. Lee, Adv. Mater., 24 (2012) 3169.

[59] G. Chen, H. Sasabe, Z. Wang, X.F. Wang, Z. Hong, Y. Yang, J. Kido, Adv. Mater., 24 (2012) 2768.

[60] R.A. Marcus, J. Chem. Phys., 24 (1956) 966.

[61] R.A. Marcus, N. Sutin, Biochim. Biophys. Acta, 811 (1985) 265.

[62] H. Bassler, Phys. Stat. Sol. (b), 175 (1993) 15.

[63] A.R. West, Basic Solid State Chemistry, John Wiley & Sons Ltd., West Sussex, 1994.

[64] V.J. McBrierty, D.C. Douglass, T.K. Kwei, Macromolecules, 11 (1978) 1265.

[65] K. Schmidt-Rohr, H.W. Spiess, Multidimensional Solid-State NMR and Polymers, Academic Press, London, 1994.

[66] X. Zhang, K. Takegoshi, K. Hikichi, Macromolecules, 24 (1991) 5756.

[67] X. Zhang, K. Takegoshi, K. Hikichi, Polymer, 33 (1992) 712.

[68] A. Asano, K. Takegoshi, K. Hikichi, Polymer, 35 (1994) 5630.

[69] H. Kaji, K. Schmidt-Rohr, Macromolecules, 33 (2000) 5169.

[70] H. Kaji, K. Schmidt-Rohr, Macromolecules, 35 (2002) 7993.

[71] H. Kaji, Y. Kusaka, G. Onoyama, F. Horii, Jpn. J. Appl. Phys., 44 (2005) 3706.

[72] M. Utz, M. Nandagopal, M. Mathai, F. Papadimitrakopoulos, Appl. Phys. Lett., 83 (2003) 4023.

[73] H. Kaji, Y. Kusaka, G. Onoyama, F. Horii, J. Am. Chem. Soc., 128 (2006) 4292.

[74] Y. Nishiyama, T. Fukushima, K. Takami, Y. Kusaka, T. Yamazaki, H. Kaji, Chem. Phys. Lett., 471 (2009) 80.

[75] H. Kaji, H. Hayashi, T. Yamada, M. Fukuchi, S. Fujimura, M. Ueda, S. Kang, T. Umeyama, Y. Matano, H. Imahori, Appl. Phys. Lett., 98 (2011) 113301.

[76] L. Frydman, J.S. Harwood, J. Am. Chem. Soc., 117 (1995) 5367.

[77] M.E. Smith, E.R.H. van Eck, Prog. Nucl. Mag. Res. Sp., 34 (1999) 159.

[78] R. Freeman, K.G.R. Pachler, G.N. Lamar, J. Chem. Phys., 55 (1971) 4586.

[79] D.F.S. Natusch, J. Am. Chem. Soc., 93 (1971) 2566.

[80] O.A. Gansow, A.R. Burke, G.N. Lamar, Chem. Commun., (1972) 456.

[81] O.A. Gansow, W.D. Vernon, A.R. Burke, J. Am. Chem. Soc., 94 (1972) 2550.

[82] L.L. Martin, H.G. Floss, E.W. Hagaman, E. Wenkert, C.J. Chang, J.A. Mabe, J. Am. Chem. Soc., 94 (1972) 8942.

[83] R.H. Meinhold, K.J.D. Mackenzie, Solid State Nucl. Magn. Reson., 5 (1995) 151.

[84] H.W. Long, R. Tycko, J. Am. Chem. Soc., 120 (1998) 7039.

[85] N.P. Wickramasinghe, M. Kotecha, A. Samoson, J. Past, Y. Ishii, J. Magn. Reson., 184 (2007) 350.

Chapter 2

Local Structure Analyses of Crystalline and Amorphous Tris(8-hydroxyquinoline) aluminum(III) (Alq_3) by Solid-State ^{27}Al MQMAS NMR Experiments

2.1. Introduction

Tris(8-hydroxyquinoline) aluminum(III) (Alq_3) is a most successful material for organic light-emitting diodes (OLEDs), which plays dual roles as light-emitter and electron-transfer. The Alq_3 is found to exist in two different isomers; facial and meridional (Fig. 2.1). These different isomeric states are considered to be one of the important factors for the ability of light-emission and electron-transfer. For example, the theoretical calculations show that the facial isomer of Alq_3 is expected to exhibit blue-shifted photoluminescence compared to the meridional isomer [1,2].

So far, five crystalline polymorphs, α, β, γ, δ, and ε-Alq_3, are found, in addition to the commonly-observed amorphous Alq_3 (amo-Alq_3) [3-9]. ^{27}Al one-dimensional (1D) NMR studies have been reported for these Alq_3s [8,9]. The NMR spectra provide the asymmetry parameter η of quadrupolar interactions in ^{27}Al nuclei, which reflect the local structures.

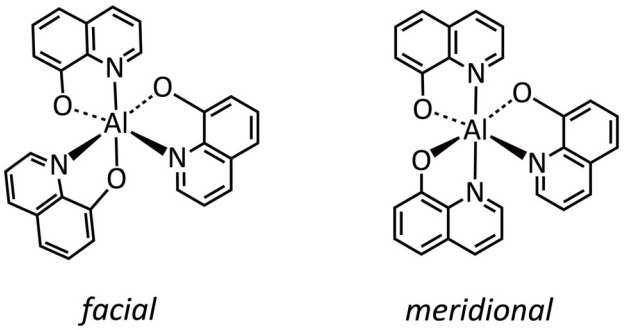

Fig. 2.1. Two isomeric states of Alq_3: facial and meridional.

The crude calculation was done with the point charge model in which the three point charges were located on the oxygen atoms; it was reported $\eta = 0$ for the facial isomer and $\eta = 0.91$ for the meridional isomer both in isolated molecules [8]. The density functional theory (DFT) calculations also exhibited $\eta = 0.00$ for the facial isomer and $\eta = 0.72$ for the meridional isomer both in isolated molecules [9]. Both the calculations resulted in the axially-symmetric interactions or a zero η for the facial isomer and the highly asymmetric interactions or a large η value for the meridional isomer. The experimental ^{27}Al 1D NMR spectrum of γ-Alq_3 was well reproduced by a single set of quadrupolar parameters with $\eta = 0.00$ [9]. For δ-Alq_3, η was not zero but was a small value; Utz et al. [8] reported $\eta = 0.12$ and Kaji et al. [9] reported $\eta = 0.24$. The small discrepancies in the results of δ-Alq_3 could be attributed to the contamination of δ-Alq_3 with γ-Alq_3 in the experiment by Utz et al., as can be seen in their powder X-ray diffraction pattern of δ-Alq_3. In either case, these small η values suggest that the γ- and δ-Alq_3 are constituted by the facial isomer. The non-zero value of η for δ-Alq_3 is ascribed to the inter-molecular interactions of electronic charges [8,9]. On the other hand, the experimental spectra of α- and amo-Alq_3 cannot be reproduced by using a single set of quadrupolar parameters [9,10]. This indicates that the quadrupolar parameters and/or chemical shift parameters are distributed due to the structural disorder. Although the fine fitting cannot be achieved with a single parameter set, the resultant spectra show highly asymmetric quadrupolar interactions for both α- and amo-Alq_3. Utz et al. [10] reported that the NMR spectrum of α-Alq_3 can be reproduced by a single set of quadrupolar parameter and that amo-Alq_3 shows a distribution of the quadrupolar coupling constant χ with a small amount of the facial isomer, by the detailed analysis of the ^{27}Al 1D magic angle spinning (MAS) NMR spectrum. However, the featureless character of the ^{27}Al 1D MAS spectrum causes some ambiguity in determining quadrupolar parameters; α-Alq_3 indeed has substantial distribution of quadrupolar parameter as

will be revealed in the present study. The local disorder in α-Alq_3 is also suggested from the X-ray diffraction experiments [3].

In this study, the analysis of the local structure in Alq_3 by means of two-dimensional (2D) ^{27}Al multi-quantum (MQ) MAS NMR experiments was conducted. The MQMAS experiments, which expand 1D MAS NMR spectrum along a new isotropic (ISO) axis, enable the precise determination of quadrupolar and chemical shift parameters [11,12]. The parameters obtained from the MQMAS experiments are further confirmed by 1D ^{27}Al MAS NMR experiments at various magnetic fields. The coexistence of meridional and facial isomers in amo-Alq_3, which is important from the perspective of device performances, is also reported.

2.2. Experimental procedures

2.2.1. Samples

Three crystalline Alq_3 polymorphs of α, γ, and δ-forms, and one amo-Alq_3 sample were used in this study. These samples were prepared by previously reported procedures [7].

2.2.2. ^{27}Al solid-state NMR experiments

The NMR experiments were performed on a JEOL JNM-ECX400 spectrometer with the magnetic field of 9.4 T, JNM-ECA500 with 11.7 T, and JNM-ECA600 with 14.1 T, and a Chemagnetics Infinity-plus 400 spectrometer with 9.4 T. 4 mm cross-polarization MAS (CP/MAS) probes were used for all the experiments. The ^{27}Al chemical shifts were adjusted to an aqueous solution of 1M $Al(NO_3)_3$. Continuous wave ^{1}H decoupling with a radiofrequency (rf) strength of 78 kHz was applied during evolution and acquisition periods. The 1D NMR spectra were recorded with a single pulse excitation of 0.2 μs to 1.0 μs under the magnetic field

of 9.4 T, 11.7 T, and 14.1 T. The MQMAS spectra were observed under a magnetic field of 9.4 T. A split-t_1 3Q sequence is used to obtain the triple-quantum MAS NMR spectra under a spinning frequency of 15.015 kHz [13]. ^{27}Al rf field strength of 167 kHz and 8 kHz were used for hard pulses and soft pulses, respectively, in the MQMAS experiments. The pulse widths in MQMAS experiments were experimentally optimized to maximize the signal intensity at $t_1 = 0$. The MQMAS spectra are displayed according to the unified representation proposed by Amoureux et al. [14,15].

2.2.3. Numerical simulations

The numerically calculated spectra were obtained by the home built C++ programs based on the GAMMA environment [16]. In order to obtain 1D/2D quadrupolar patterns for randomly oriented powder samples, powder averaging is required; the calculated spectra for various molecular orientations have to be co-add, even if the molecules have a uniform quadrupolar parameter. The calculated spectra with 1000 pairs of REPULSION [16] set, which distributed uniformly over the unit sphere, were summed up for each powder patterns. When the distributions of quadrupolar parameters were included, further spectral summation was needed; the spectra with distribution of quadrupolar parameter were obtained by weighted summation of 80 powder-patterns. A Lorenzian line broadening of 200 Hz was applied to the calculated spectra.

2.3. Results and discussion

2.3.1. ^{27}Al MQMAS NMR of γ- and δ-Alq_3

Figure 2.2(a) and (b) show the ^{1}H decoupled ^{27}Al MAS NMR spectrum of γ- and δ-Alq_3,

respectively. As well known, the ^{27}Al MAS NMR spectra exhibits broad powder patterns due to the second order quadrupolar broadening even if only a single site exits in the sample. The spectra of γ- and δ-Alq_3 exhibit powder patterns with horns near each edge of the powder patterns, which is characteristic of the powder pattern with small η values. This result suggests that γ- and δ-Alq_3 consist of the facial isomers.

The second order quadrupolar broadening can be removed by the 2D MQMAS experiments. The MQMAS experiment provides a correlation between the usual MAS dimension (quadrupolar anisotropy (QA) axis) and an isotropic dimension (ISO axis). The detailed description of MQMAS experiment was provided in Refs [11,12]. Here, we briefly explain spectral patterns obtained by MQMAS experiments. In addition to the vertical ISO axis and the horizontal QA axis, two tilted axes, the chemical shift (CS) axis and the quadrupolar induced shift (QIS) axis, are often shown in MQMAS spectra for guide for eye (ex. Fig. 2.3). If the sample has a single set of quadrupolar parameters, η and χ, and isotropic chemical shift, δ_{cs}, the slice along the ISO axis shows a sharp resonance and that along the QA axis shows a powder pattern which is identical to a typical 1D MAS NMR spectrum. The peak position along the ISO axis is given by [14,15]

$$\delta_{\mathrm{ISO}} = \delta_{\mathrm{CS}} - \frac{10}{17}\delta_{\mathrm{QIS}} \tag{2.1}$$

with

$$\delta_{\mathrm{QIS}} = -\frac{1}{10}\frac{4S(S+1)-3}{[4S(2S-1)]^2}\frac{3+\eta^2}{\nu_0^{\,2}}\chi^2 \cdot 10^6 \ \ [\mathrm{ppm}], \tag{2.2}$$

where δ_{cs} is the isotropic chemical shift, S is the spin quantum number, and ν_0 is the Larmor frequency. Note that the resonance position along the ISO axis includes not only the isotropic

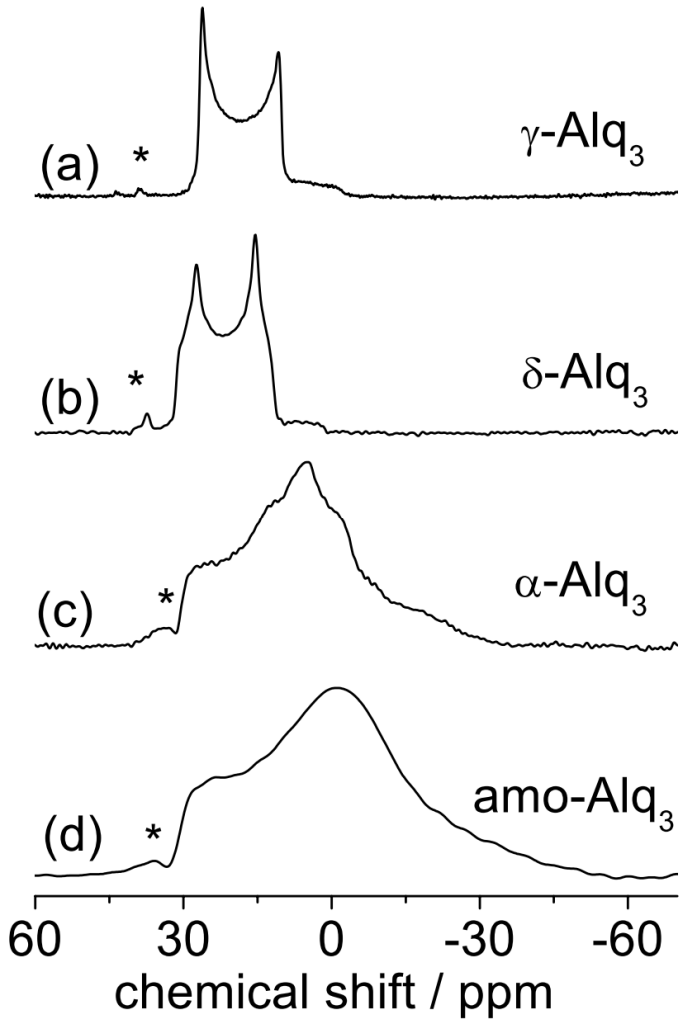

Fig. 2.2. ^{1}H decoupled ^{27}Al MAS NMR spectra of (a) γ-, (b) δ-, (c) α-, and (d) amo-Alq_3 under a sample spinning frequency of 15.015 kHz. The spectra were observed at 9.4 T. The asterisks indicate satellite transition lines.

chemical shift, δ_{cs}, but also the quadrupolar parameters, η and χ. Therefore, eqs. (2.1) and (2.2) indicate that the distribution of quadrupolar and/or chemical shift parameters induces the spectral distribution in the ISO axis, resulting in a two dimensionally distributed powder pattern. When the quadrupolar parameter is distributed, the 2D spectra spread along the QIS axis. In contrast, the 2D spectra spread along the CS axis, when the isotropic chemical shift is distributed.

The left traces in Fig. 2.3(a) and (b) show the experimental ^{1}H decoupled ^{27}Al MQMAS spectra of γ- and δ-Alq_3, respectively. The gravity center of the signals of these Alq_3s, consisting of facial isomers, appear at (QA, ISO) = (~20 ppm, 38 ppm) in the MQMAS spectra. The spectra exhibit sharp resonances in the ISO dimension, which is typically observed for a well-defined crystal sample with a single set of quadrupolar and chemical shift parameters. This clearly shows that γ- and δ-Alq_3 have single quadrupolar and chemical shift parameters and thus an ordered structure. We determined the χ, η, and δ_{cs} values by spectral simulations (right traces in Fig. 2.3). The parameters thus obtained are listed in Table 2.1. Note that the ^{1}H decoupling greatly enhances the resolution of the ^{27}Al MQMAS spectra, although the ^{1}H decoupling does not much affect the lineshape of the ^{27}Al 1D MAS NMR spectra under the present experimental condition (~15 kHz MAS). This is because the MQ coherence is much affected by the ^{1}H–^{27}Al heteronuclear dipolar coupling than the single quantum coherence [18, 19].

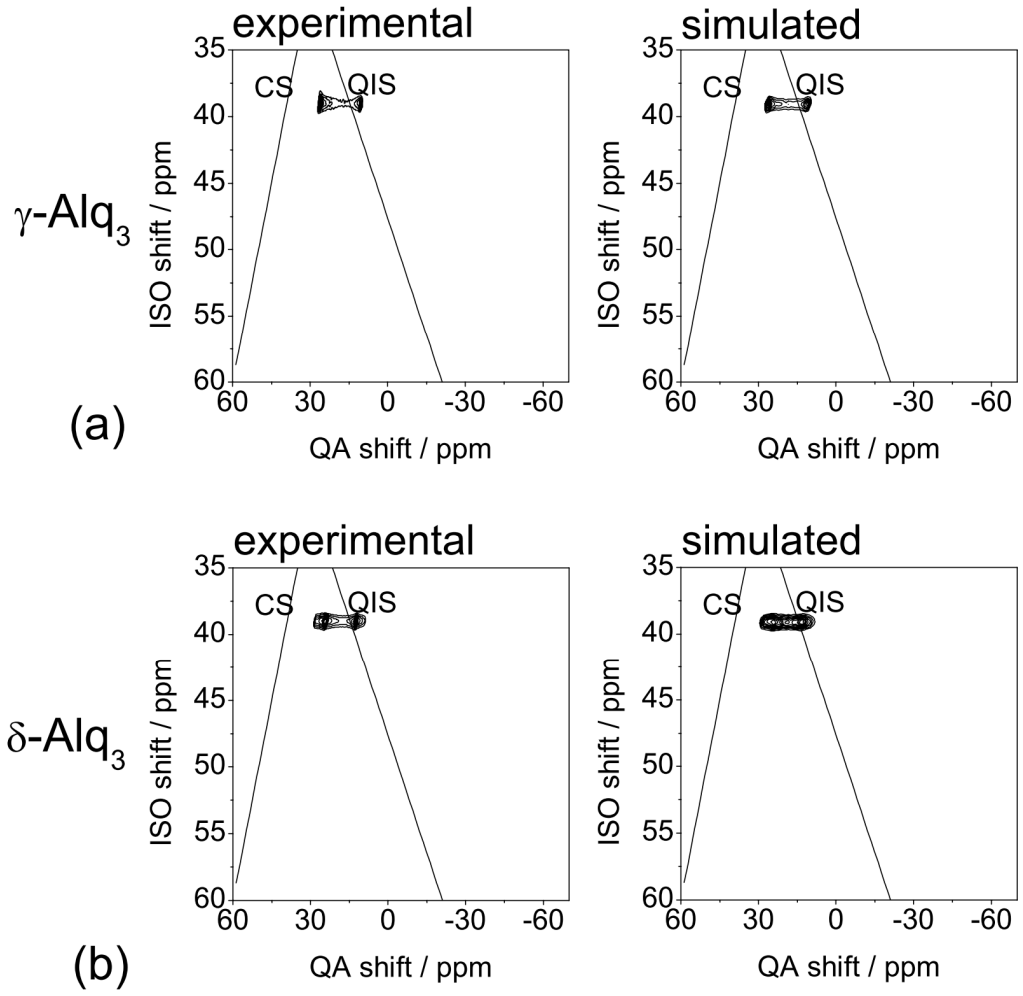

Fig. 2.3. Experimental (left) and simulated (right) ^{1}H decoupled ^{27}Al MQMAS spectra of (a) γ- and (b) δ-Alq_3 under the magnetic field of 9.4 T. The samples were spun with a spinning frequency of 15.015 kHz. The CS and QIS axes are guide for eye. The parameters used in the simulations are shown in Table 2.1.

Table 2.1. Parameters used in calculating the spectra of α-, γ-, δ-, and amo-Alq_3.

	δ_{cs} / ppm	χ_0 / MHz	η	σ^+ / MHz	σ^- / MHz	P
α_1	31.0	5.5	0.70	0.20	0.25	0.33
α_1	30.5	6.4	0.84	0.15	0.35	0.67
γ	31.3	4.90	0.00			
δ	31.0	4.84	0.22			
amorphous	30.5	7.0	0.9	0.4	0.8	

2.3.2. ^{27}Al MQMAS NMR of α- and amo-Alq_3

Figure 2.2(c) and (d) show ^{1}H decoupled ^{27}Al MAS NMR spectra of α- and amo-Alq_3, respectively. Both the spectra exhibit the highest intensity near the center of the powder patterns, which means $\eta > 0.5$. These experimental spectra could not be reproduced by any single set of quadrupolar parameters. Introduction of distributions in quadrupolar/chemical shift parameters is necessary, which reflects some structural distributions in α- and amo-Alq_3.

Left traces of Fig. 2.4(a) and (b) show the experimental ^{1}H decoupled ^{27}Al MQMAS spectra of α- and amo-Alq_3, respectively. It is found that two dimensionally broadened signals both for α- and amo-Alq_3 exist. No signal was found at the area where the signals of γ- and δ-Alq_3 appear. It was also found that the 2D powder pattern in the MQMAS spectrum of the α-Alq_3 is clearly different from that of the amo-Alq_3, although the 1D MAS spectra are very similar to each other as shown in Fig. 2.2(c) and (d). Two distinctly different sites are clearly observed in α-Alq_3, which we refer to as α_1- and α_2-components in α-Alq_3 as shown in Fig. 2.4(a). The powder patterns of the α_1- and α_2-components in the α-Alq_3, and the amo-Alq_3 are extended not along the CS axis but along the QIS axis. This means that the broadening is caused by the distributions of quadrupolar parameter χ and/or η, neither by distribution of δ_{cs} nor by rapid relaxation; rapid relaxation simply broadens the spectra along QA and ISO axis [13]. The calculation with the distribution of η values does not reproduce the experimental spectra at all. We found that the calculated spectra provide excellent agreement with the experimental spectra, assuming a following asymmetric Gaussian distribution of the χ value:

$$P(\chi) = \frac{1}{\sigma^{-} + \sigma^{+}} \sqrt{\frac{2}{\pi}} \exp \frac{(\chi_0 - \chi)^2}{2\sigma(\chi)^2}, \tag{3}$$

where

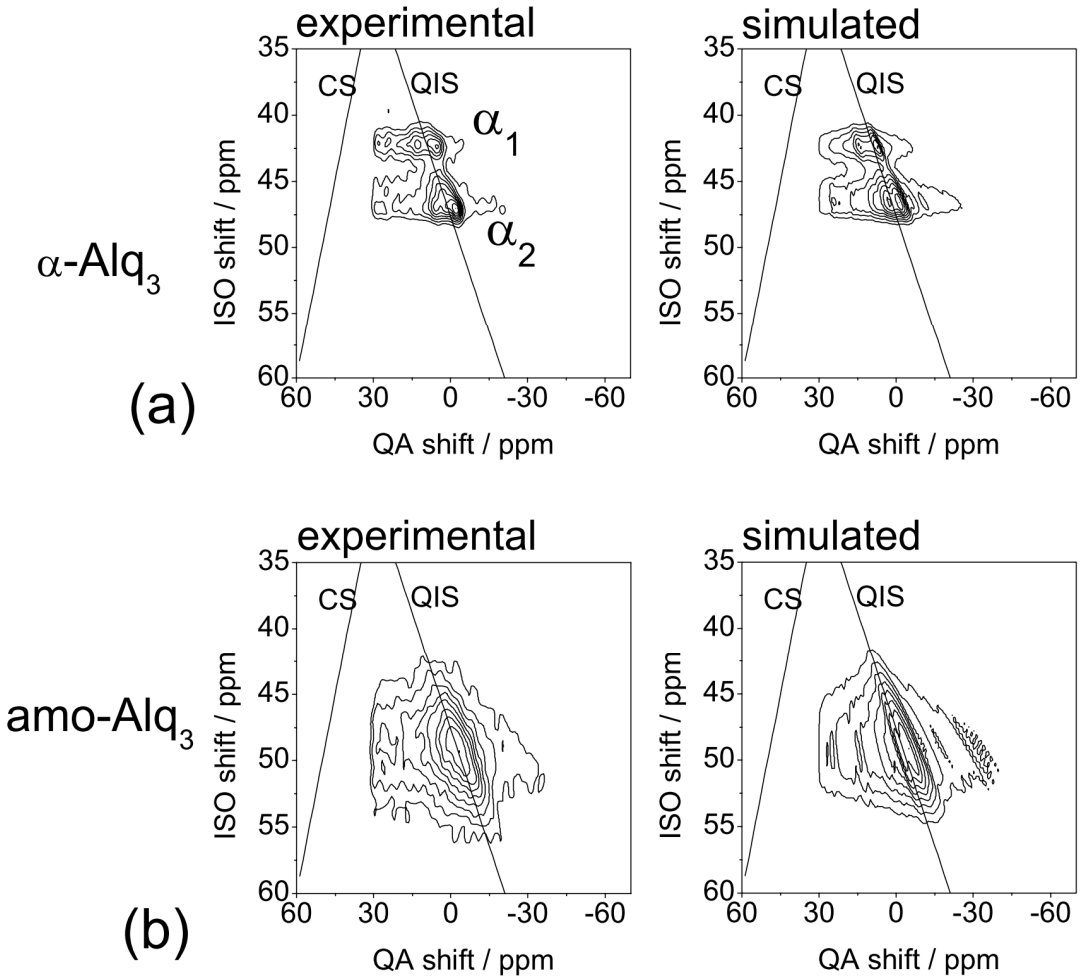

Fig. 2.4. Experimental (left) and simulated (right) ^{1}H decoupled ^{27}Al MQMAS spectra of (a) α- and (b) amo-Alq_3 under the magnetic field of 9.4 T. The samples were spun with a spinning frequency of 15.015 kHz. The CS and QIS axes are guide for eye. The parameters used in the simulations are shown in Table 2.1.

$$\sigma(\chi)=\begin{cases}\sigma^{-} \text{ for } \chi<\chi_0\\ \sigma^{+} \text{ for } \chi\geq\chi_0\end{cases}. \quad (4)$$

The calculated α-Alq_3 spectrum was obtained by adding the two sub-spectra for the α_1-, α_2-components, assuming the probability P_1 for the α_1-components and thus $P_2 = 1 - P_1$ for the α_2-components. Figure 2.4(a) (right) shows the best-fit simulated spectrum for α-Alq_3, where the η values for the α_1-, and α_2-components are 0.70 and 0.84, respectively. The simulated spectrum well agrees with the experimental spectrum. The simulation of the MQMAS spectrum was also carried out for the amo-Alq_3, assuming an asymmetric Gaussian distribution for the parameter, χ. The best-fit 2D pattern for amo-Alq_3 with $\eta = 0.9$ is shown in Fig. 2.4(b) (right). The simulated spectrum provides the excellent agreement with the experimental spectrum. All the parameters for α- and amo-Alq_3 are summarized in Table 2.1.

From the above analysis of the MQMAS spectra, we found that the α_1-, α_2-components in α-Alq_3 and the amo-Alq_3 show the η value larger than 0.7. This result shows that both the α- and amo-Alq_3 consist of the meridional isomer. In Fig. 2.2, the 1D spectra of Alq_3 which consists of the facial isomers (Fig. 2.2(a) and (b)) are not clearly separated from those of the meridional isomers (Fig. 2.2(c) and (d)). Therefore, it has been difficult to estimate the amount of facial isomers in amo-Alq_3 from the 1D spectrum. On the other hand, in MQMAS spectra, the resonance lines for the α- and amo-Alq_3 (meridional) appear at the ISO shift of > 41 ppm (Fig. 2.4) and those for the γ- and δ-Alq_3 (facial) appear at the ISO shift of 38 ppm (Fig. 2.3). Therefore, the resonance lines for the meridional and facial isomers can be clearly distinguished in the MQMAS spectra, which has been impossible in the 1D experiments. Here, we estimated the amount of the facial isomers in amo-Alq_3 from the MQMAS spectra. Qualitatively, judging from Fig. 2.4(b), the contribution of facial isomers was negligible or vary

small for amo-Alq_3. Comparing the experimental spectrum (Fig. 2.4(b)) with the summation of the calculated spectra for amo-Alq_3 and γ- (or δ-) Alq_3, we can conclude that an amount of the facial isomer in amo-Alq_3 is less than 3%.

2.3.3. 1D ^{27}Al MAS NMR under various B_0 fields

We further confirm the parameters for α- and amo-Alq_3 in Table 2.1 by observing 1D ^{27}Al MAS NMR spectra under various B_0 fields. The lineshapes of ^{27}Al MAS NMR spectra depend on the B_0 field. Variable B_0 experiments strongly ensure the parameters in Table 2.1. Figure 2.5 shows the experimental and calculated 1D ^{27}Al MAS NMR spectra of α- and amo-Alq_3 observed under 9.4, 11.7 and 14.1 T. The parameters in Table 2.1 were used to obtain the calculated spectra. The calculated spectra well reproduce the experimental spectra. This confirms the validity of the parameters in Table 2.1. In the calculations of MQMAS spectra, we did not include the imperfection due to the quadrupolar parameter and molecular orientation dependence of multiple-quantum transfer efficiency [12]. Although this imperfection could account for the asymmetric distribution shown in Fig. 2.4, the calculated spectra with symmetric distribution of $P(\chi)$ do not reproduce the experimental 1D MAS NMR spectra. Thus, we can clearly conclude that $P(\chi)$ is asymmetric.

We note that low B_0 field experiments are preferable for the present purpose to investigate the local structures. This is against the common belief in the solid-state NMR field that the higher B_0 field is preferable for the solid-state NMR experiments on quadrupolar nuclei. As well known, the linewidths of ^{27}Al MAS spectra decreases as the B_0 field increases. This feature is desirable in most cases. However, in the present case, all the ^{27}Al MAS and MQMAS spectra of α-, γ-, δ-, and amo-Alq_3 provide sharp peaks at nearly identical positions under the infinite B_0 field, since the isotropic chemical shifts are nearly the same and only the

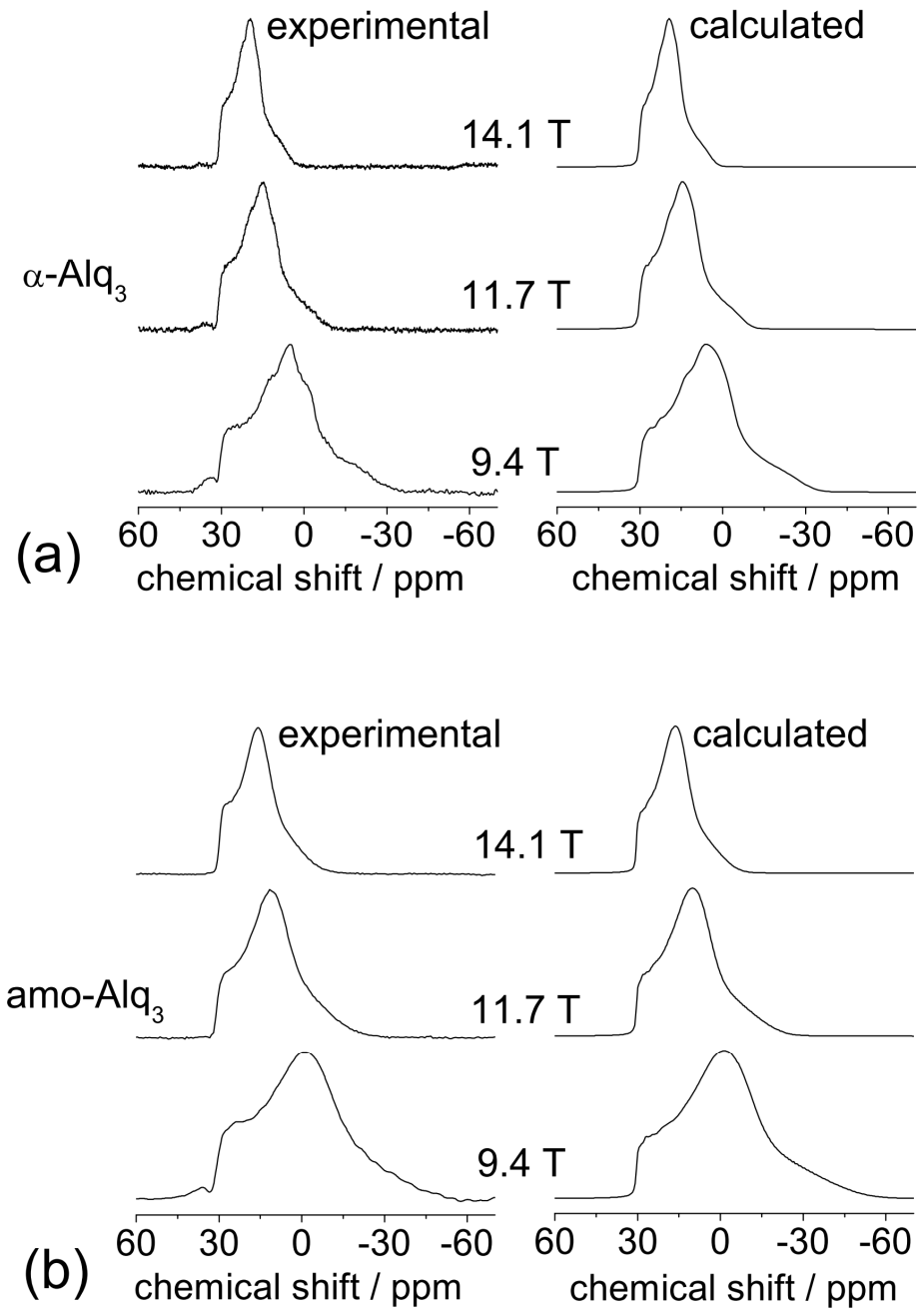

Fig. 2.5. Experimental (left) and calculated (right) ^{1}H decoupled ^{27}Al MAS NMR spectra of (a) α- and (b) amo-Alq_3.

difference between these polymorphs is quadrupolar parameters. Therefore, the distinction of isomeric states and the estimation of the structural distribution become difficult with increasing the B_0 field.

2.4. Conclusions

The local structure, including the structural distribution, of Alq_3s in different crystalline and amorphous states have been investigated by ^{27}Al 1D MAS NMR and 2D MQMAS experiments. By the MQMAS experiments, the resonance lines for Alq_3s with the facial isomers and those with the meridional isomers could be clearly separated from each other, which are overlapped in the ^{27}Al 1D MAS and ^{13}C CP/MAS NMR spectra. The isomeric states of γ- and δ-Alq_3 (facial) and α- and amo-Alq_3 (meridional) are confirmed from the asymmetry parameter η of ^{27}Al quadrupolar interactions. In addition, both the α- and amo-Alq_3 exhibit large distribution of the quadrupolar coupling constant χ. This is in sharp contrast to the γ- and δ-Alq_3; both the spectra can be explained by a single quadrupolar parameter set without considering any distributions. This indicates that the local structures are disordered for the α- and amo-Alq_3, whereas those for the γ- and δ-Alq_3 are well-defined. The MQMAS experiments also exhibit that there are two distinctly different sites in α-Alq_3. This is clearly different from the local structure of amo-Alq_3 consisting of a disordered single site. The difference has not been observed in standard ^{27}Al 1D MAS and ^{13}C CP/MAS NMR spectra. The facial isomer in amo-Alq_3 is estimated less than 3%.

References

[1] A. Curioni, M. Boero, W. Andreoni, Chem. Phys. Lett., 294 (1998) 263.

[2] M. Amati, F. Lelj, Chem. Phys. Lett., 358 (2002) 144.

[3] M. Brinkmann, G. Gadret, M. Muccini, C. Taliani, N. Masciocchi, A. Sironi, J. Am. Chem. Soc., 122 (2000) 5147.

[4] M. Braun, J. Gmeiner, M. Tzolov, M. Coelle, F.D. Meyer, W. Milius, H. Hillebrecht, O. Wendland, J.U.V. Schütz, W. Brütting, J. Chem. Phys., 114 (2001) 9625.

[5] M. Cölle, R.E. Dinnebier, W. Brütting, Chem. Commun., 23 (2002) 2908.

[6] M. Rajeswaran, T. N. Blanton, J. Chem. Crystallogr., 35 (2005) 71.

[7] H. Kaji, Y. Kusaka, G. Onoyama, F. Horii, J. Am. Chem. Soc., 128 (2006) 4292.

[8] M. Utz, M. Nandagopal, M. Mathai, F. Papadimitrakopoulos, Appl. Phys. Lett., 83 (2003) 4023.

[9] H. Kaji, Y. Kusaka, G. Onoyama, F. Horii, J. J. Appl. Phys., 44 (2005) 3706.

[10] M. Utz, M. Nandagopal, M. Mathai, F. Papadimitrakopoulos, J. Chem. Phys., 124 (2006) 034705.

[11] L. Frydman, J.S. Harwood, J. Am. Chem. Soc., 117 (1995) 5367.

[12] M.E. Smith, E.R.H. van Eck, Prog. Nucl. Magn. Reson. Spec., 34 (1999) 159.

[13] S.P. Brown, S. Wimperis, J. Magn. Reson., 128 (1997) 42.

[14] J.P. Amoureux, C. Fernandez, Solid State Nucl. Magn. Reson., 10 (1998) 211.

[15] J.P. Amoureux, C. Huguenard, F. Engelke, F. Taulelle, Chem. Phys. Lett., 356 (2002) 497.

[16] S.A. Smith, T.O. Levante, B.H. Meier, R.R. Ernst, J. Magn. Reson. A, 106 (1994) 75.

[17] M. Bak, N.C. Nielsen, J. Magn. Reson., 125 (1997) 132.

[18] M. Hanaya, R.K. Harris, Solid State NMR, 8 (1997) 147.

[19] S. Ganapathy, L. Delevoye, J.P. Amoureux, P.K. Madhu, Mang. Reson. Chem., 46 (2008)

948.

Chapter 3

Preparation of Green- and Blue-Emitting Tris(8-hydroxyquinoline) aluminum(III) (Alq_3) Crystalline Polymorphs and Application to Organic Light-Emitting Diodes

3.1. Introduction

There has been increasing interest in organic light-emitting diodes (OLEDs) owing to their applications to ultra-thin flat panel displays and lighting. Since Tang and VanSlyke used tris(8-hydroxyquinoline) aluminum(III) (Alq_3) in double-layered OLEDs for the first time in 1987 [1], this material has been widely and continuously used for OLEDs as a light-emitting and/or electron-transporting material. In addition to intensive and extensive research on device fabrication using Alq_3, relatively recently, there has been fundamental research on the crystal and amorphous structures of bulk Alq_3 powders. Studies on the crystal structures revealed that Alq_3 has polymorphs [2-12], and the crystals in different polymorphs consist of Alq_3 molecules in meridional or facial isomeric states, which possess C_1 and C_3 symmetries, respectively (Fig. 3.1). For deposited amorphous films, some researchers have suggested the coexistence of meridional and facial isomers [13-15]. The minor facial isomers are assumed to work as carrier traps in amorphous films in Ref. [14].

The performance of OLEDs is considered to be affected by device-fabrication processes, and various studies have been carried out to clarify the effects. For example, the performance of OLEDs with Alq_3 depends on the Alq_3 deposition rate [16-21]. It has also been reported that the lifetime of an OLED can be improved by decreasing pressure in a vacuum chamber during the deposition, although the initial OLED performance does not change with a difference in pressure [22]. The purity of material is another important factor in OLED fabrication.

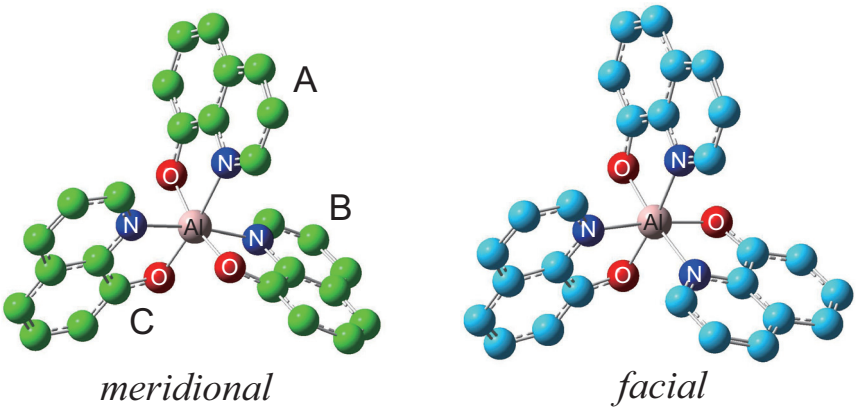

Fig. 3.1. Two isomeric states of Alq_3: meridional and facial. The three ligands in the meridional isomer, labeled A, B, and C, are not equivalent while, those in the facial isomer are equivalent. Hydrogen atoms are omitted for clarity.

Normally-observed dispersive electron transport becomes nondispersive for Alq_3 through repeated purification in train sublimation [15].

In this study, we investigated the effect of crystalline polymorphs as source powders for device fabrication. First, temperature-dependent X-ray diffraction measurements and photoluminescence (PL) measurements were carried out for Alq_3 with different crystalline polymorphs, namely 1) the α-form only, 2) the δ-form only, and 3) a mixture of α-, γ-, and δ-forms. Next, OLEDs were fabricated from the three types of crystalline polymorphs as source powders. The use of different crystal forms as the source powder is an interesting aspect of device fabrication that may affect OLED performance.

3.2. Experimental procedures

3.2.1. Sample preparations

Alq_3 used in this study was synthesized from aluminum isopropoxide and

8-hydroxyquinoline (8-quinolinol) with a molar ratio of 1:3 and dried under vacuum overnight. The crude Alq_3 thus obtained was purified in a temperature-gradient sublimation apparatus with a turbo-molecular pump under vacuum. Alq_3 in α-crystalline form (α-Alq_3) was obtained via this sublimation process. Alq_3 in δ-crystalline form (δ-Alq_3) was prepared as follows. First, we put 170 mg of α-Alq_3 powder in a precleaned and well-dried tube made of quartz glass. Second, the tube was sealed using a gas burner under vacuum created with an oil-sealed rotary vacuum pump through a cold trap (liquid N_2). Third, the α-Alq_3 powder vacuum-encapsulated in the quartz glass tube was thermally annealed at 420 °C for 5 h, and then slowly cooled to room temperature. This sample preparation procedure was different from our previous method [9,11]. By vacuum-encapsulating the sample in the quartz glass tube prior to thermal treatment, we avoid the degradation of the sample by oxygen and other substances. The sample that was a mixture of α-, γ-, and δ-crystalline forms (αγδ-Alq_3) was prepared in a manner similar to that described above for the preparation of δ-Alq_3. The first and second processes were exactly the same; i.e., the α-Alq_3 powder was vacuum-encapsulated in a quartz glass tube. In the third step, the thermal annealing was carried out at 320 °C for 3 h and was followed by quenching of the sample to 0 °C.

3.2.2. Wide-angle X-ray diffraction measurements

The polymorphs were identified by wide-angle X-ray diffraction (WAXD) measurements at room temperature. Temperature-dependent WAXD experiments for α-Alq_3 and δ-Alq_3 under vacuum were carried out to clarify the temperature change of the crystalline form and to determine the crystalline form immediately before vacuum deposition. The measurements were carried out between 30 °C and 300 °C under vacuum produced by an oil-sealed rotary vacuum pump. Prior to the measurements, the sample was held at a given temperature for 10

min. The WAXD data were recorded using a Rigaku RINT-2000 diffractometer with Cu-$K\alpha$ radiation at 300 mA and 40 kV. The scattering angle 2θ was scanned in steps of 0.02° over a range of 3-35°.

3.2.3. Photoluminescence measurements

PL measurements were carried out at room temperature using a Hamamatsu Photonics K. K. absolute PL quantum yield measurement system (C9920-02) with excitation wavelength of 375 nm.

3.2.4. OLED fabrication and characterization

The OLED structure was indium tin oxide (ITO) (55 nm)/*N,N′*-di(1-naphthy)-*N,N′*-diphenylbenzidine (α-NPD) (40 nm)/Alq_3 (60 nm)/cesium carbonate (Cs_2CO_3) (1.5 nm)/aluminum (Al) (80 nm). Here, α-NPD was used as a hole-transporting layer, and Alq_3 was used as an emissive and electron-transporting layer. Cs_2CO_3, which has been reported to enhance electron injection from the Al to the Alq_3 layer [23-28], was used as an electron injection layer. The ITO and Al were used as the anode and cathode material, respectively. For Alq_3, three types of samples were used as source powders; 1) α-Alq_3, 2) δ-Alq_3, and 3) αγδ-Alq_3. It was reported that the evaporation temperature affected the morphology of films and the device performance [19,29], and we should consider the effect. In this study, the applied electric powers were almost same (~ 59 W) for all of the deposition of α-Alq_3, δ-Alq_3, and αγδ-Alq_3. Therefore, the influence of evaporation temperature on the device performance was considered to be negligible. An ITO patterned glass substrate with an active area of 2×2 mm^2 was swabbed with acetone, and then ultrasonically cleaned in detergent, ultrapure water, acetone, and isopropyl alcohol. The substrate was then cleaned with isopropyl alcohol vapor

and ultraviolet-ozone treated. α-NPD, Alq_3, Cs_2CO_3, and Al were deposited at a pressure of 10^{-4} Pa. The current density (*J*)–voltage (*V*)–luminance (*L*) characteristics of the OLEDs were measured with a source measure unit (Keithley 2400) and spectroradiometer (Topcon, SR-3). Personal-computer based software for OLED characterization was kindly provided by Keithley Instruments K. K. Japan.

3.3. Results and discussion

3.3.1. Identification of polymorphs and a new method to obtain pure δ-Alq_3

Figure 3.2 shows the experimental WAXD profiles of Alq_3 samples. Some diffractions assigned to α-Alq_3, γ-Alq_3, and δ-Alq_3 are shown as vertical green, purple, and blue lines in the figure, respectively. The pattern in Fig. 3.2(a) matches the previously reported α-Alq_3 patterns [2,3,9], confirming that the sample is the α-Alq_3. Yellowish α-Alq_3 was obtained in relatively large amounts (several grams) through train sublimation. The pattern in Fig. 3.2(b) matches δ-Alq_3 patterns [4,6,9]. It has been difficult for us to produce pure δ-Alq_3 [9,11], in that the contamination of α-Alq_3 or γ-Alq_3 has been unavoidable. Pure δ-Alq_3 was obtained by washing the crude δ-Alq_3 with an excess of chloroform and drying under vacuum for 1 day in our previous work [9,11]. Fortunately, in this study, the pure δ-Alq_3 could be obtained without contamination of other crystalline forms using the vacuum-encapsulated procedure described in the experimental section. This is an easy way to prepare pure δ-Alq_3 quantitatively. The WAXD pattern for the αγδ-Alq_3 sample is shown in Fig. 3.2(c). The WAXD profile of the αγδ-Alq_3 sample is found to be composed of those of α-Alq_3, γ-Alq_3, and δ-Alq_3. This clearly shows that the three phases are certainly contained in the αγδ-Alq_3 sample. From the WAXD results, the samples for Fig. 3.2(a), (b), and (c) are confirmed to be pure α-Alq_3, pure δ-Alq_3,

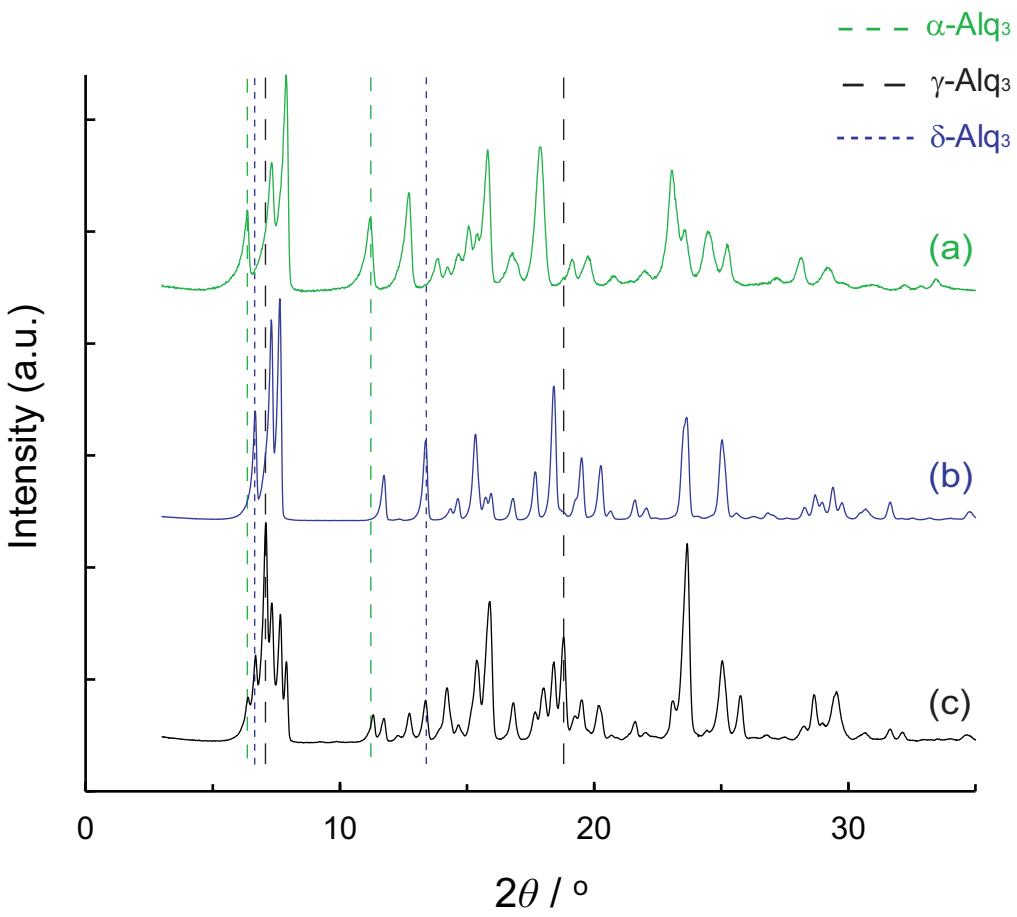

Fig. 3.2. X-ray diffraction profiles of (a) α-Alq_3, (b) δ-Alq_3, and (c) the mixture of α-, γ-, and δ-Alq_3. Some diffraction peaks representative of α-Alq_3, γ-Alq_3, and δ-Alq_3 are indicated by vertical dashed lines in the figure.

and a mixture of α-, γ-, and δ-Alq_3 (αγδ-Alq_3), respectively.

3.3.2. Transformation of polymorphs during thermal annealing

In a vacuum deposition, organic materials are heated in crucibles and the crystalline polymorphs and isomeric states may change. To understand the change due to thermal annealing, we carried out temperature-dependent WAXD experiments under vacuum. The temperature-dependent WAXD patterns for the α-Alq_3 sample are shown in Fig. 3.3. The experiments were carried out from 30 ºC to 300 ºC. Overall patterns appear similar to the patterns of the α-form [2,3,9] and are clearly different from those of all other crystalline forms. Therefore, it is found that the Alq_3 sample remains the α-type polymorph and does not transform into other crystalline forms. In detail, the diffractions shift slightly toward a smaller angle; for example, the diffraction at 11.3º at 30 ºC becomes 11.0º at 300 ºC. This indicates that the crystalline lattice expands with increasing temperature. We should note that the diffraction around 18º in α-Alq_3 splits into two at elevated temperature (above ~175 ºC). The split of the diffraction is considered to originate from the existence of disorder. The local disorder in α-Alq_3 was suggested [2,9,11,30] and some structural modifications may occur by the thermal annealing.

After the WAXD measurements, the Alq_3 molecules were found to be deposited to the chamber of the WAXD apparatus. Therefore, the crystalline form for the α-Alq_3 sample is found to remain in the α-form even immediately before vacuum deposition.

The temperature-dependent WAXD patterns of the δ-Alq_3 sample are shown in Fig. 3.4. The diffraction patterns indicate that the sample remains in δ-form up to 150 °C. An evident change is observed at ~175 °C; the δ-form becomes the γ-form and the sample remains as γ-Alq_3 up to 300 ºC. At $2\theta < 10^{o}$, three diffractions are found below 150 ºC (that is, for

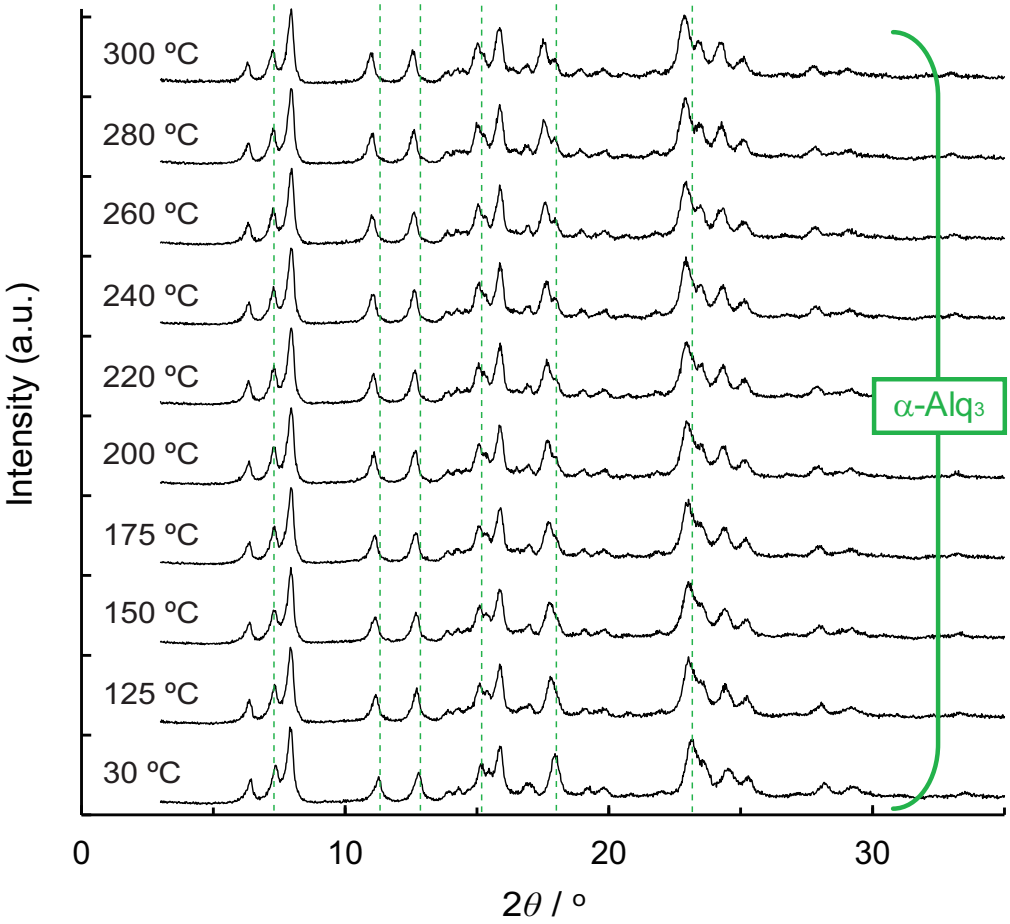

Fig. 3.3. Temperature-dependent X-ray diffraction profiles of Alq_3 powders under vacuum, originally in α-form.

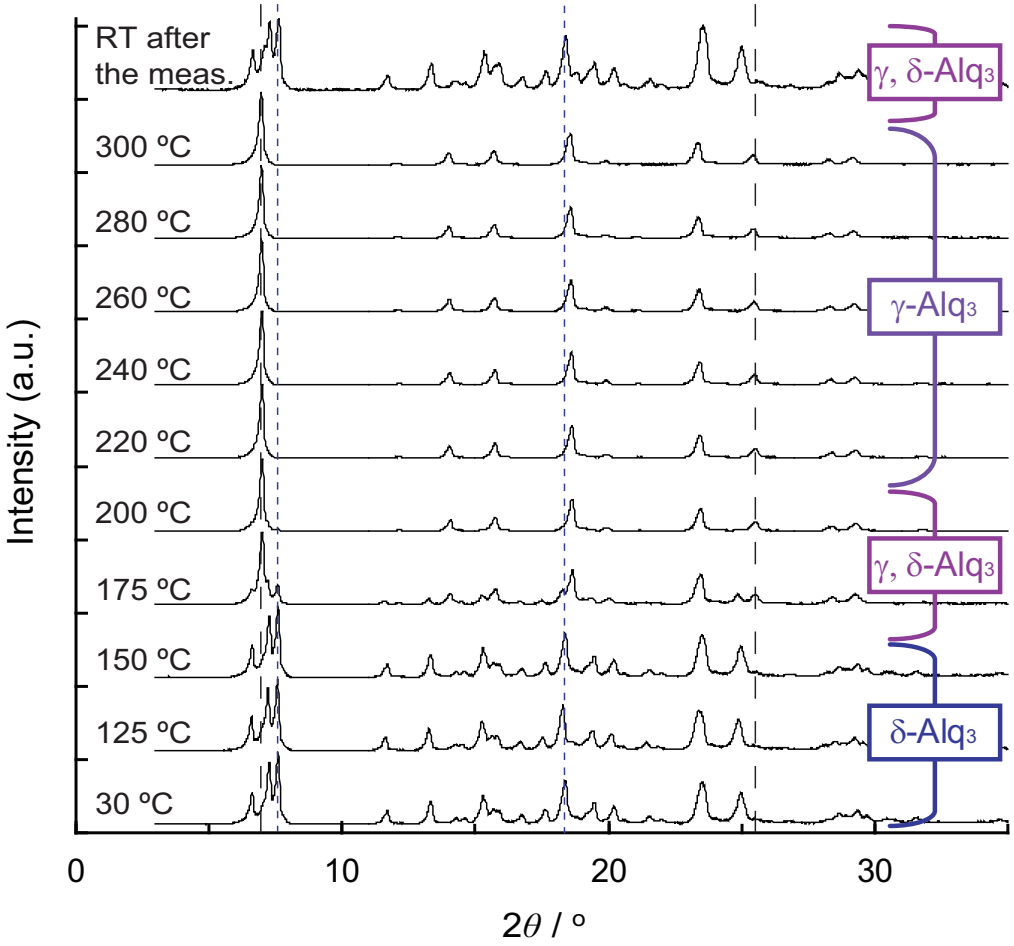

Fig. 3.4. Temperature-dependent X-ray diffraction profiles of Alq_3 powders under vacuum, originally in δ-form.

δ-Alq_3), whereas only one diffraction is observed above 200 °C (that is, for δ-Alq_3), although both of the polymorphs are composed of facial isomers. Bravais lattices of δ-Alq_3 and γ-Alq_3 belong to triclinic (*P*1) [4,31] and trigonal crystals (*P*3) [2,8], respectively. The blue-emitting Alq_3 crystals change to higher symmetric structure above 200 °C, which results in a simpler WAXD profile. Clear lattice expansion is not observed for either δ-Alq_3 or γ-Alq_3. As has been reported [2,8,9,11], γ-Alq_3 can exist at room temperature. However, the transformation from δ-Alq_3 to γ-Alq_3 with heating and that from γ-Alq_3 to δ-Alq_3 with cooling (see below) suggests that δ-Alq_3 is more stable below ~170 ºC and γ-Alq_3 is more stable above ~180 ºC. The result coincides with a suggestion by Brinkmann et al. [2] that γ-Alq_3 is a high-temperature phase. The isomeric states of γ-Alq_3 and δ-Alq_3 are determined to be facial [3,6,8,9,11]. Therefore, the transformation at ~175 °C is a change in crystalline form without ligand exchange (i.e., without a change in the isomeric state). The sample was found to be deposited to the chamber of the WAXD apparatus after the measurements. Therefore, the crystalline form of the δ-Alq_3 sample is found to be γ-Alq_3 immediately before the vacuum deposition. Cölle et al. [6] observed a small transition at 145 ºC for δ-Alq_3 in a differential scanning calorimetry measurement and they stated, “We are not sure about the origin of this transition…”. The origin of the transition is possibly the transition from δ-Alq_3 to γ-Alq_3, as observed in this study.

We previously prepared γ-Alq_3 under atmospheric conditions. Here, we tried to prepare γ-Alq_3 of device-fabrication grade using the vacuum-encapsulated quartz glass tube. From Fig. 3.4, the pure γ-Alq_3 is expected to be prepared by quenching from above 200 ºC to below room temperature. The top of Fig. 3.4 shows the WAXD profile at room temperature after the measurements at 300 ºC. The profile clearly shows that most of the γ-Alq_3 at 300 ºC becomes δ-Alq_3 and only a limited contribution remains as γ-Alq_3. Sufficiently fast quenching could

not be achieved for the sample in the vacuum-encapsulated quartz glass tube. Therefore, high-quality γ-Alq_3, which could be used for device applications, could not be obtained.

3.3.3. Optical properties

Figure 3.5(a) shows PL spectra of the α-Alq_3, δ-Alq_3, and αγδ-Alq_3 powder samples. The α-Alq_3 powders have typical green emission with PL maximum at 520 nm. In contrast, blue emission is observed for δ-Alq_3 powders with PL maximum at 481 nm. The αγδ-Alq_3 powders have green emission with PL maximum at 508 nm. It has been reported that γ-Alq_3 powders have blue emission with PL maximum at 468 nm [9,11]. In comparing the PL spectra of α-Alq_3 and αγδ-Alq_3 in Fig. 3.5(a), there is disagreement on the short wavelength side. This originates from a contribution to the emission by γ- and δ-Alq_3. However, the overall spectral pattern of the PL spectrum of αγδ-Alq_3 mostly agrees with that of α-Alq_3. This indicates that energy transfer occurs from γ- and δ-Alq_3 domains to α-Alq_3 domains. The PL quantum yields (PLQYs) were 36 %, 47 %, and 35 % for α-Alq_3, δ-Alq_3, and αγδ-Alq_3 powder samples, respectively.

Figure 3.5(b) shows PL spectra of the deposited films prepared from α-Alq_3, δ-Alq_3, and αγδ-Alq_3 samples as source powders. We visually confirm that all the deposited films are transparent. The PL spectra are almost indistinguishable; the maximum wavelengths of the PL spectra were 531, 529, and 532 nm for the films prepared from α-Alq_3, δ-Alq_3, and αγδ-Alq_3, respectively. The PLQYs for all of the deposited films were 22 %. The isomeric state of Alq_3 in the deposited films is considered to be predominantly meridional. However, the coexistence of facial isomers in the deposited films cannot be denied, because energy can transfer from Alq_3 in the facial isomer to that in the meridional isomer, as occurs in the PL experiments for the αγδ-Alq_3 powder samples in Fig 3.5(a).

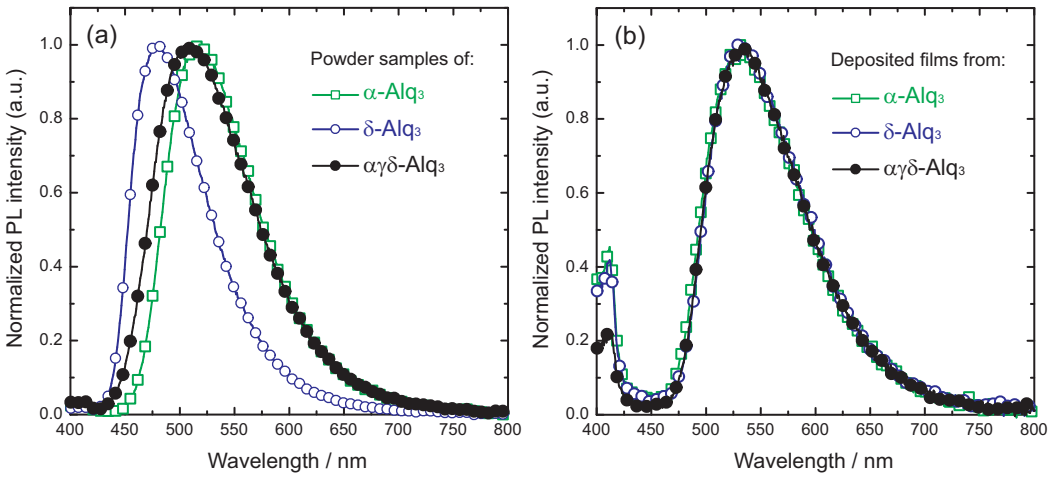

Fig. 3.5. Normalized PL spectra of (a) the three types of Alq_3 powder samples used in this study, α-Alq_3, δ-Alq_3, and the mixture of α-, γ-, and δ-Alq_3, and (b) their deposited films. The excitation wavelength is 375 nm.

3.3.4. Electroluminescence characteristics of OLEDs

Figure 3.6 shows the EL characteristics of OLEDs with a device structure of ITO (55 nm)/α-NPD (40 nm)/Alq_3 (60 nm)/Cs_2CO_3 (1.5 nm)/Al (80 nm). Three types of OLEDs were prepared using 1) α-Alq_3, 2) δ-Alq_3, and 3) αγδ-Alq_3 as source powders. Here, OLEDs prepared from α-Alq_3, δ-Alq_3, and αγδ-Alq_3 are referred to as α-OLED, δ-OLED, and αγδ-OLED, respectively. The *J–V* characteristics are shown in Fig. 3.6(a). The *J–V* curves for all three OLEDs are found to be almost the same, irrespective of the Alq_3 crystalline polymorph before vacuum deposition. The *L–V* characteristics of the three OLEDs are shown in Fig. 3.6(b). As opposed to the case for the *J–V* data in Fig. 3.6(a), distinct differences are observed; the αγδ-OLED provides the highest luminance and the α-OLED the lowest. Figure 3.6(c) shows the current efficiency–current density characteristics of the three OLEDs. Reflecting the *L–V* characteristics, it is found that the current efficiency of the δ-OLED is up to 1.1 times that of the α-OLED. The current efficiency of the αγδ-OLED is much higher, up to 1.4 times that of the α-OLED. The difference is also found in external quantum efficiencies (EQEs)–current density plots in Fig.3.6(d). The EQEs at 1000 cd/m^2 (~ 40 mA/cm^2) were estimated to be 0.75 %, 0.80 %, and 1.0 % for α-OLED, δ-OLED, and αγδ-OLED, respectively. The EQE, η_{exe}, is expressed as $\eta_{exe} = \Gamma \times \beta \times \Phi \times \eta_p$, where Γ is the carrier balance ratio of holes and electrons, β is an exciton generation factor, Φ is a light out-coupling factor, and η_p is the PL quantum efficiency. The emission here is from the excited singlet state. Considering the singlet/triplet branching ratio, the value of β is considered to be 0.25 for electrical excitation. The device structures are the same and the values of Φ (~ 20 % [32]) are considered to be the same for the three OLEDs in this study. The PLQY, η_p, was 22 % for all devices as shown in Section 3.3.3. Therefore, the EQE is found to be directly reflected in the carrier balance ratio; the values of Γ are calculated to be 68 %, 72 %, 90 % for α-OLED, δ-OLED, and αγδ-OLED,

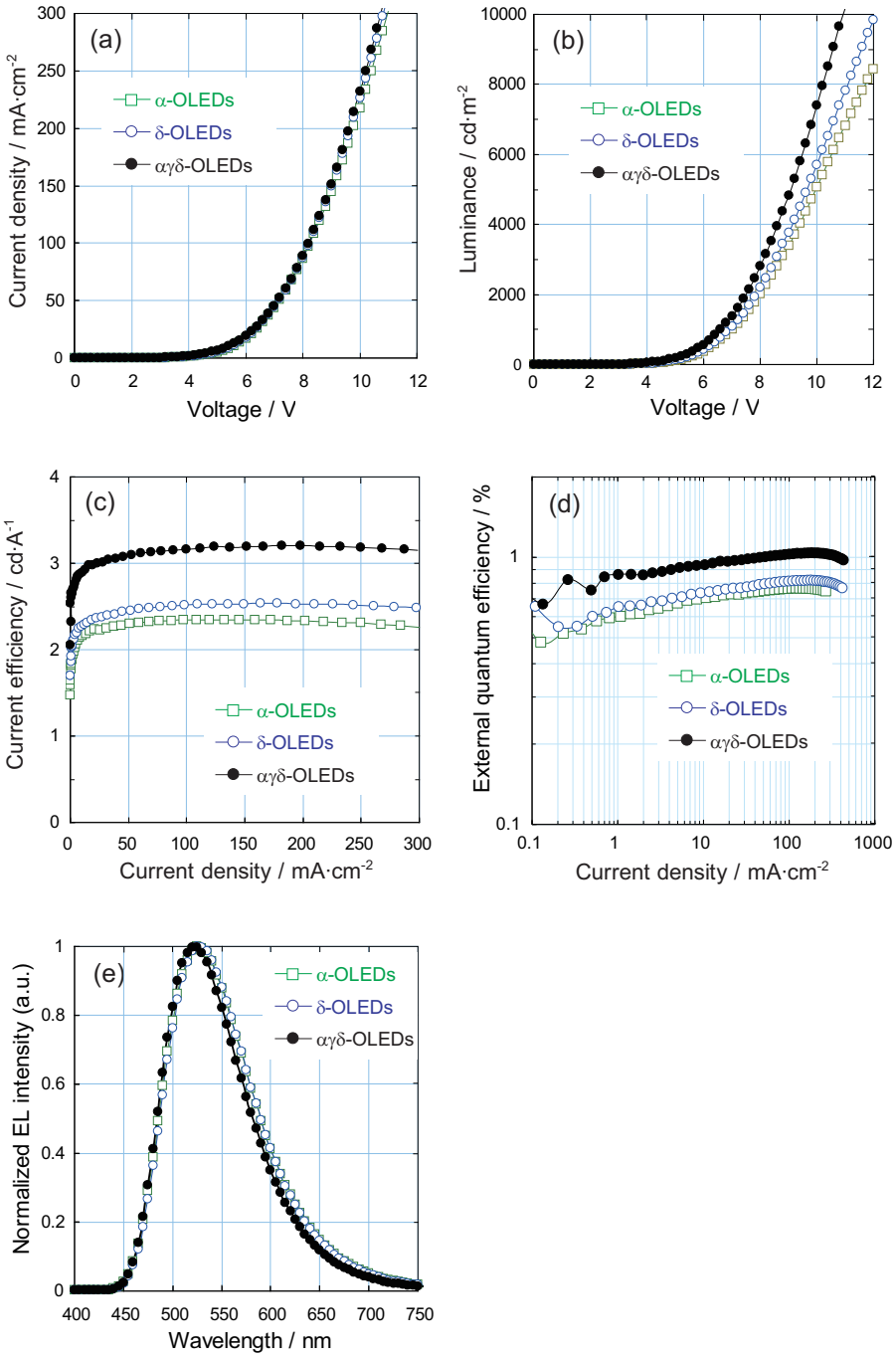

Fig. 3.6. The EL characteristics of OLEDs fabricated from α-Alq_3, δ-Alq_3, and the mixture of α-, γ-, and δ-Alq_3. These OLEDs are denoted α-OLED, δ-OLED, and αγδ-OLED, respectively. (a) Current density–voltage, (b) luminance–voltage, (c) current efficiency–current density, and (d) external quantum efficiencies–current density characteristics are shown. The normalized EL spectra measured at a driving current density of 25 mA/cm^2 are shown in (e).

respectively. The carrier balance for the αγδ-Alq_3 OLED increases to nearly 100 % without a change in the device structure. This is a possible reason for the improved EQEs. Figure 3.6(e) shows the EL spectra of the three OLEDs at a current density of 25 mA/cm^2. All OLEDs exhibit green EL emission with a peak at approximately 525 nm, irrespective of the crystalline polymorph before vacuum deposition. Although the PL spectra of the three deposited films are indistinguishable with each other, the EL spectrum of the αγδ-OLED is slightly narrower than those of the other two devices. The difference of the EQEs in the three devices might originate from the effect of the optical interference, as another possible reason.

3.4. Conclusions

Temperature-dependent WAXD experiments of α-Alq_3 and δ-Alq_3 were performed under vacuum from 30 ºC to 300 ºC to investigate the crystalline transformation and the isomeric state change. For α-Alq_3, the crystalline form does not change and the isomeric state remains meridional up to the sublimation temperature. For δ-Alq_3, the crystalline form becomes the γ-form, but the isomeric state remains facial up to the sublimation temperature. On the basis of these results, we prepared three different Alq_3 samples of device-fabrication grade, namely 1) pure α-Alq_3, 2) pure δ-Alq_3, and 3) a mixture of α-, γ-, and δ-Alq_3, by simple thermal annealing in vacuum-encapsulated quartz glass tubes. Using these samples, we examined the effect of polymorphs as source powders on OLED performance. The EL performance of typical OLEDs consisting of ITO/α-NPD/Alq_3/Cs_2CO_3/Al depended on the polymorphs of source powders; the luminance efficiency of OLEDs fabricated from δ-Alq_3 and that from the mixture of α-, γ-, and δ-Alq_3 were enhanced by factors of 1.1 and 1.4, respectively, compared with the case for α-Alq_3, although the device structure is the same. The origin of the enhancement is not clear at this stage, but the results will be used to improve OLED performance for various

materials with polymorphs. The EL wavelengths do not depend on the polymorphs and isomeric states of source powders; all OLEDs in this study have green emission.

References

[1] C.W. Tang, S.A. VanSlyke, Appl. Phys. Lett., 51 (1987) 913.

[2] M. Brinkmann, G. Gadret, M. Muccini, C. Taliani, N. Masciocchi, A. Sironi, J. Am. Chem. Soc., 122 (2000) 5147.

[3] M. Braun, J. Gmeiner, M. Tzolov, M. Coelle, F.D. Meyer, W. Milius, H. Hillebrecht, O. Wendland, J.U. von Schütz, W. Brütting, J. Chem. Phys., 114 (2001) 9625.

[4] M. Cölle, R.E. Dinnebier, W. Brütting, Chem. Commun., 23(2002) 2908.

[5] M. Cölle, S. Forero-Lenger, J.r. Gmeiner, W. Brütting, Phys. Chem. Chem. Phys., 5 (2003) 2958.

[6] M. Cölle, J. Gmeiner, W. Milius, H. Hillebrecht, W. Brütting, Adv. Funct. Mater., 13 (2003) 108.

[7] M. Brinkmann, B. Fite, S. Pratontep, C. Chaumont, Chem. Mater., 16 (2004) 4627.

[8] M. Muccini, M.A. Loi, K. Kenevey, R. Zamboni, N. Masciocchi, A. Sironi, Adv. Mater., 16 (2004) 861.

[9] H. Kaji, Y. Kusaka, G. Onoyama, F. Horii, Jpn. J. Appl. Phys., 44 (2005) 3706.

[10] M. Rajeswaran, T.N. Blanton, J. Chem. Crystallogr., 35 (2005) 71.

[11] H. Kaji, Y. Kusaka, G. Onoyama, F. Horii, J. Am. Chem. Soc., 128 (2006) 4292.

[12] R. Katakura, Y. Koide, Inorg. Chem., 45 (2006) 5730.

[13] P.E. Burrows, H. Shen, V. Bulovic, D.M. McCarty, S. Forrest, J.A. Cronin, M.E. Thompson, J. Appl. Phys., 79 (1996) 7991.

[14] A. Curioni, M. Boero, W. Andreoni, Chem. Phys. Lett., 294 (1998) 263.

[15] G.G. Malliaras, Y. Shen, D.H. Dunlap, H. Murata, Z.H. Kafafi, Appl. Phys. Lett., 79 (2001) 2582.

[16] B.J. Chen, W.Y. Lai, Z.Q. Gao, C.S. Lee, S.T. Lee, W.A. Gambling, Appl. Phys. Lett., 75

(1999) 4010.

[17] L.F. Cheng, L.S. Liao, W.Y. Lai, X.H. Sun, N.B. Wong, C.S. Lee, S.T. Lee, Chem. Phys. Lett., 319 (2000) 418.

[18] Y. Qiu, D.Q. Zhang, J. Qiao, Y. Shao, Synth. Met., 110 (2000) 241.

[19] T. Kato, T. Mori, T. Mizutani, Thin Solid Films, 393 (2001) 109.

[20] H.C. Mu, H. Shen, D. Klotzkin, Solid-State Electron., 48 (2004) 2085.

[21] Y.H. Lee, W.J. Kim, T.Y. Kim, J.H. Yang, K.S. Cho, J.W. Hong, J.Y. Shin, T.W. Kim, Mol. Cryst. Liq. Cryst., 462 (2007) 143.

[22] T. Ikeda, H. Murata, Y. Kinoshita, J. Shike, Y. Ikeda, M. Kitano, Chem. Phys. Lett., 426 (2006) 111.

[23] C.-I. Wu, C.-T. Lin, Y.-H. Chen, M.-H. Chen, Y.-J. Lu, C.-C. Wu, Appl. Phys. Lett., 88 (2006) 152104.

[24] M.-H. Chen, C.-I. Wu, J. Appl. Phys., 104 (2008) 113713.

[25] M.H. Chen, Y.J. Lu, C.C. Wu, C.I. Wu, Thin Solid Films, 518 (2010) 3942.

[26] M.-H. Chen, Y.-J. Lu, Y.-J. Chang, C.-C. Wu, C.-I. Wu, Electrochem. Solid-State Lett., 13 (2010) H203.

[27] I.W. Wu, Y.-H. Chen, P.-S. Wang, C.-G. Wang, S.-H. Hsu, C.-I. Wu, Appl. Phys. Lett., 96 (2010) 013301.

[28] J.S. Yang, D.C. Choo, T.W. Kim, Y.Y. Jin, J.H. Seo, Y.K. Kim, Thin Solid Films, 518 (2010) 6149.

[29] G.F. Wang, X.M. Tao, H.M. Huang, Appl. Surf. Sci., 253 (2007) 4463.

[30] M. Rajeswaran, T.N. Blanton, R.H. Young, W. Brennessel, J. Chem. Crystallogr., 40 (2010) 195.

[31] M. Rajeswaran, T.N. Blanton, K.P. Klubek, Z. Kristallogr., 218 (2003) 439.

[32] J.S. Kim, P.K.H. Ho, N.C. Greenham, R.H. Friend, J. Appl. Phys., 88 (2000) 1073.

Chapter 4

Sensitivity Enhancement in Solid-State NMR of Organic Thin-Film Semiconductors by a Paramagnetic System

4.1. Introduction

Organic thin-film semiconductors, such as organic light-emitting diodes (OLEDs), organic solar cells (OSCs), and organic thin-film transistors (OTFTs) are promising alternatives to inorganic semiconductors, and are extensively studied because these organic semiconductors are lighter, less expensive, and more flexible than their inorganic counterparts [1-7]. However, the analytical methods of these devices on an atomic level are quite limited. This is because these organic devices, especially OLEDs, are often used in amorphous state, hampering the application of diffraction methods including X-ray and neutron diffraction, because of a lack of long-range periodic structures. By contrast, solid-state nuclear magnetic resonance (solid-state NMR) has great potential for the analysis of amorphous organic materials [8-18]. One practical limitation of NMR is its intrinsically low sensitivity. This is especially true for the analysis of organic devices for which the sample volume is quite limited; most organic devices have a thickness of only 50 to 100 nm to reduce the driving voltage [2,19-24]. The low sensitivity and limited sample volumes hamper the application of solid-state NMR to organic devices.

Substantial efforts have been made to overcome the low sensitivity of NMR. One reason for its low sensitivity is the slow relaxation process of nuclear spin systems, which is described by the longitudinal relaxation time (T_1). The nuclear spin system is well isolated from the thermal bath and most NMR spectrometer time is spent waiting for the spin system to return to the thermal equilibrium state between contiguous observations. One of the most widely used

and cost-effective methods in solution NMR is the use of paramagnetic relaxation reagents, which significantly reduce T_1 relaxation times [25-30]. The unpaired electrons in the paramagnetic species greatly reduce the T_1 relaxation time of neighboring nuclear spin through the interaction between electron and nuclear spins [31]. This uniformly enhances the relaxation process of all the nuclei in a solution sample where the molecules have equal chances of contacting the paramagnetic species by the rapid translational molecular motion observed in solution samples [25-30]. The reduction of T_1 relaxation times allows the quick repetition of solution NMR measurements, i.e., because of the shorter relaxation delay between contiguous scans, leading to sensitivity enhancement in the unit time.

On the other hand, a paramagnetic dopant is less effective in solid-state NMR. In solid samples, neighboring nuclei are affected by paramagnetic species and show significant line-broadening because of dipolar shift and paramagnetic relaxation. This is because of the limited molecular motion in solid samples, which results in significantly strong interactions between electrons and nuclei. By contrast, nuclei, which are distant from paramagnetic centers, show almost no reduction of their T_1 relaxation time. These are the reasons why only a small number of solid-state NMR studies have been reported [32-34]. Relaxation enhancements are reported for ^{29}Si and ^{89}Y nuclei systems doped with lanthanide paramagnetic ions [32] and for a system of frozen Cu-doped peptide aqueous solutions [33]. Recently, a new approach using Cu(II) Na_2 ethylenediaminetetraacetate (Cu-EDTA) doping of microcrystalline protein samples is reported [34]. In this method, ^{1}H–^{1}H spin diffusion is utilized to transfer the ^{1}H magnetization, which is produced by quick paramagnetic relaxation, from the surface to the inside of the crystals. This effectively reduces the ^{1}H T_1 relaxation time, not only of neighboring nuclei, but also of nuclei far from the paramagnetic centers. The key to this approach is transfer of the ^{1}H magnetization from the paramagnetic centers to remote ^{1}H nuclei

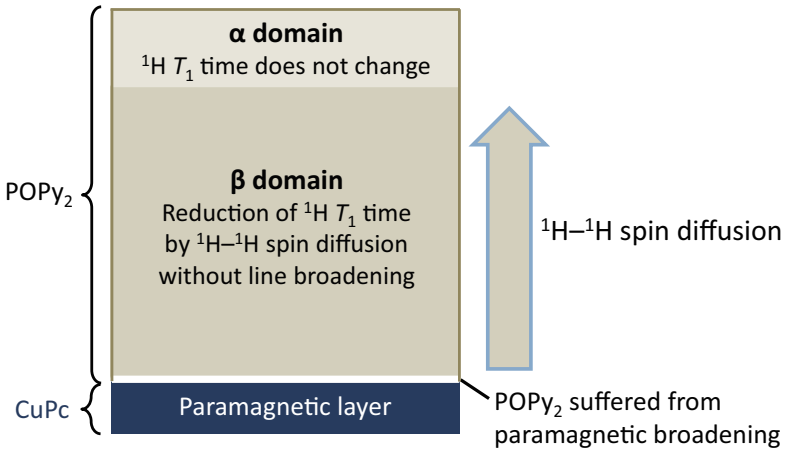

Fig. 4.1. Schematic representation of ^{1}H T_1 reduction in POPy$_2$ thin organic films with paramagnetic dopant (CuPc).

through ^{1}H–^{1}H spin diffusion. This enhances the ^{1}H T_1 relaxation of remote ^{1}H spins without giving rise to paramagnetic broadening.

In this study, the sensitivity enhancement in solid-state NMR of organic thin-film semiconductor samples by paramagnetic dopant layers assisted by ^{1}H–^{1}H spin diffusion is investigated (Fig. 4.1). The samples we used were bilayer thin films; a thin-film sample was deposited on a paramagnetic thin film layer. The following three conditions should be satisfied to bring about ^{1}H T_1 time reduction with minimal effects from harmful paramagnetic broadening:

Condition 1:

The paramagnetic dopant is sufficiently closely attached to the surface of the thin film that ^{1}H magnetization transfer from the dopant to the molecules in the thin film and paramagnetic relaxation on the surface of the film will occur.

Condition 2:

The film is sufficiently thin so that the ^{1}H magnetization from the paramagnetic dopant will diffuse throughout most of the ^{1}H nuclei within the thin film.

Condition 3:

The film is sufficiently thick so that the abundance of those nuclei that are close to the paramagnetic ions and suffer severe paramagnetic broadening, can be safely neglected.

The ^{1}H magnetization in the paramagnetic dopant layers is quickly relaxed by unpaired electron spins. ^{1}H nuclei in thin films closely attached to the paramagnetic dopant layers are polarized by direct interaction with unpaired electrons and by the ^{1}H magnetization of paramagnetic dopant layers through dipolar interaction between ^{1}H nuclei in paramagnetic dopant layers and those in the thin films. ^{1}H nuclei located at the inner part of the thin film are polarized by the ^{1}H–^{1}H spin diffusion among ^{1}H nuclei in the thin film. This efficiently reduces the ^{1}H T_1 relaxation time in the thin films, leading to a reduction of measurement time by shortening the required repetition time. Fortunately, as clarified in the Results and Discussion section, most nuclei in the thin films with thicknesses typical for organic semiconductors are polarized by ^{1}H–^{1}H spin diffusion and are free from paramagnetic broadening, which only appears in the nuclei of neighboring paramagnetic ions. The measurement time reduction in nuclei other than ^{1}H is also realized by magnetization transfer from ^{1}H nuclei to other nuclei via cross polarization (CP) in which intervals between successive observations can be determined by the ^{1}H T_1 relaxation time.

Here we used a binary thin film composed of copper phthalocyanine (CuPc) and phenyldipyrenylphosphine oxide ($POPy_2$) (Fig. 4.2), which is widely used in thin-film organic devices because of its favorable properties allowing for good carrier injection from electrodes

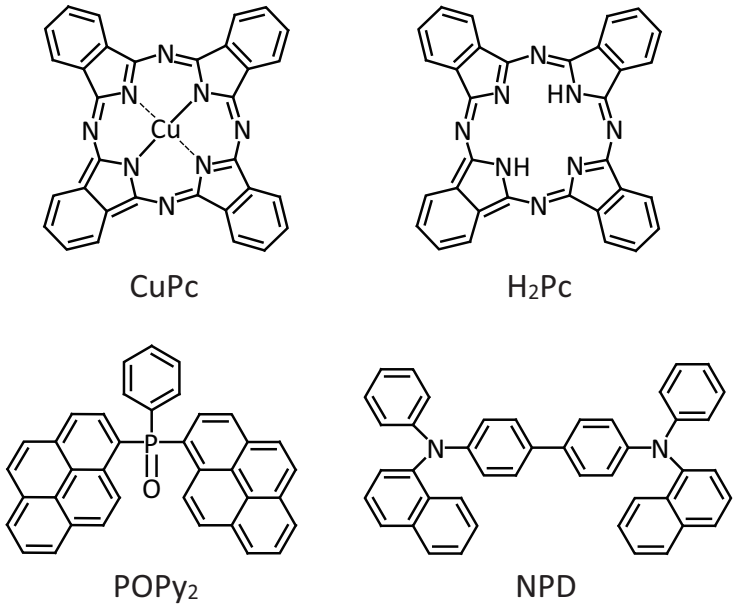

Fig. 4.2 Chemical structure of the materials used in this study.

and having good carrier transporting characteristics, respectively [19,20,35–38]. The carrier injection material, CuPc, is expected to work as a paramagnetic dopant for $POPy_2$ to enhance the ^1H T_1 relaxation in $POPy_2$. As shown below, a vacuum-deposited film ensures close contact between CuPc and $POPy_2$ (condition 1), and a $POPy_2$ thickness of 50–100 nm, which is widely used in devices, is suitable for ^1H–^1H spin diffusion (conditions 2 and 3). Sensitivity enhancement of ^{31}P CP magic-angle spinning (MAS) NMR of $POPy_2$ is demonstrated.

4.2. Experimental procedures

4.2.1. Sample preparations

Six different samples, schematically shown in Fig. 4.3, were vacuum-deposited on glass substrates measuring 145×145 mm^2:

A: *N,N′*-di(1-naphthyl)-*N*,*N′*-diphenylbenzidine (NPD) 400 nm/$POPy_2$ 1200 nm

B: CuPc 1200 nm

C: NPD 400 nm/$POPy_2$ 200 nm/(CuPc 30 nm/$POPy_2$ 400 nm)×2)/CuPc 30 nm/$POPy_2$ 200 nm

D: NPD 400 nm/$POPy_2$ 100 nm/(CuPc 30 nm/$POPy_2$ 200 nm)×5)/CuPc 30 nm/$POPy_2$ 100 nm

E: NPD 400 nm/$POPy_2$ 50 nm/(CuPc 30 nm/$POPy_2$ 100 nm)×11)/CuPc 30 nm/$POPy_2$ 50 nm

F: NPD 400 nm/$POPy_2$ 50 nm/(H_2Pc 30 nm/$POPy_2$ 100 nm)×11)/H_2Pc 30 nm/$POPy_2$ 50 nm.

The materials used in this study were purified by vacuum sublimation. Glass substrates were pre-cleaned using acetone and chloroform. NPD, CuPc, H_2Pc, and $POPy_2$ (Fig. 4.2) were deposited under a pressure less than 3×10^{-4} Pa. Samples A and C–F had a total $POPy_2$ thicknesses of 1200 nm. The samples deposited were scraped off the glass substrates using a sharp blade from an area of about 60×80 mm^2 where the samples were deposited to give a homogeneous thickness. About 12–17 mg of the samples was thus obtained from the respective thin films. All of the samples except for sample B were deposited on NPD, which is commonly used as a hole-transport material in OLEDs [3,4,7,35]. By using an NPD layer, we could scratch off all of the $POPy_2$ and CuPc (or H_2Pc) layers without loss of the $POPy_2$ and CuPc (or H_2Pc) samples. Note that the NPD layer does not affect the solid-state NMR spectra in this study. Samples B, C, D, and E mimic the $POPy_2$/CuPc layers with a $POPy_2$ thickness of 200 nm, 100 nm, and 50 nm, respectively. We deposited multiple thin-film layers of $POPy_2$/CuPc for samples C–F to increase the amounts of respective samples. The inner $POPy_2$ layer had twice the thickness of the outer $POPy_2$ layers, because the inner $POPy_2$ layers faced two CuPc layers on the top and underneath. All of the CuPc layers in samples C–F were deposited with a thickness of 30 nm. Sample F was prepared to confirm the effect of paramagnetic relaxation, which originates from the CuPc layers. Sample F had the same structure as sample E except that metal-free phthalocyanine (H_2Pc) substituted for CuPc. From

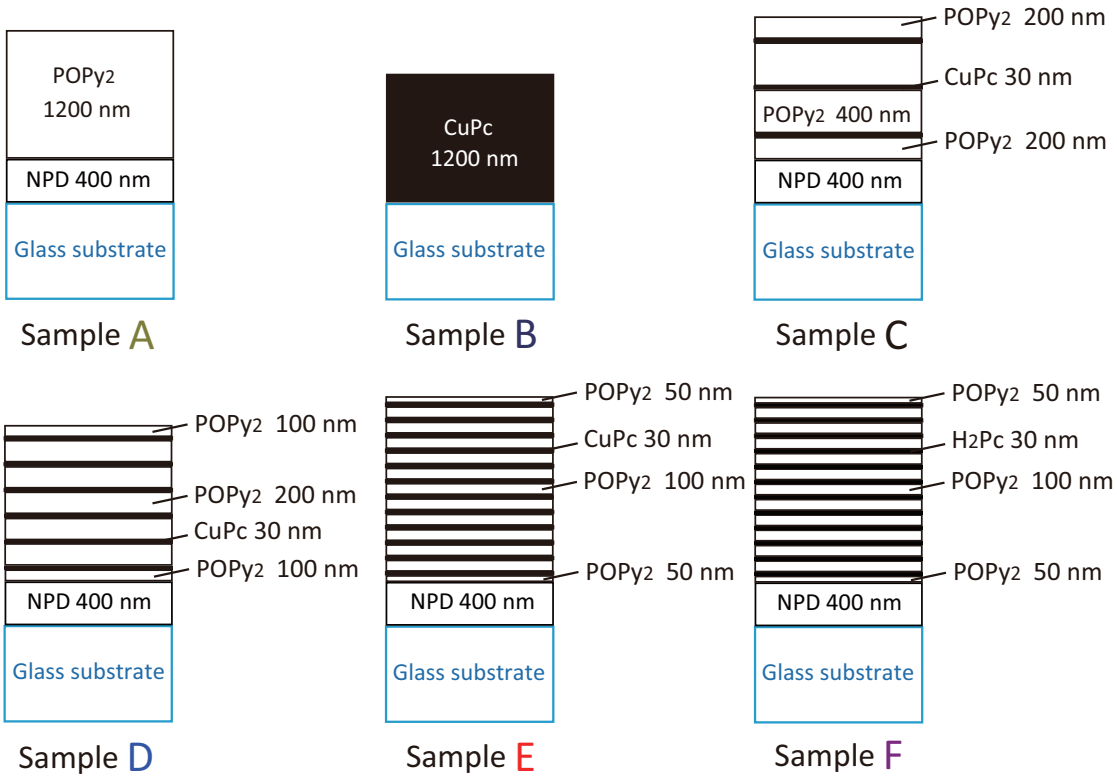

Fig. 4.3. Detailed configurations of the thin-film samples used in this study. Sample A was composed of $POPy_2$ (and NPD). Sample B was composed only of CuPc. Samples C, D, and E mimic the $POPy_2$/CuPc layers with a $POPy_2$ thickness of 200 nm, 100 nm, and 50 nm, respectively. Sample F has the same configuration as sample E except that H_2Pc substitutes for CuPc.

a comparison made of samples E and F, the contribution of the effect of paramagnetic Cu^{2+} ions and that of the heterosurface between phthalocyanine and $POPy_2$ to the relaxation behaviors can be distinguished. The details are described in Section 4.3.1.

4.2.2. Solid-state NMR analysis of organic thin films

All of the solid-state NMR measurements were conducted using a Bruker Avance III 400 MHz spectrometer operating under a static magnetic field of 9.4 T. A double-resonance probe with a 4.0 mm MAS stator was used. ^{1}H and ^{31}P radiofrequency (rf) field strengths $\gamma B_1/2\pi$ of 80 kHz were used for all pulses. The MAS spinning speed was set to 15 kHz and the experiments were conducted at 300 K. The longitudinal relaxation times T_1 for ^{1}H of $POPy_2$ in samples A–F were measured using a saturation recovery type sequence; in which the initial ^{1}H magnetization is saturated by a rf comb of twenty 3.13 μs 90° pulses and recovered ^{1}H magnetization after relaxing periods were monitored as ^{31}P signal intensity via CP under MAS. For comparison, the ^{1}H T_1 time of $POPy_2$ powder crystals was measured using the same pulse sequence. The ^{1}H T_1 times of CuPc in sample B and CuPc needle crystals were obtained by directly measuring the ^{1}H signal intensity with the saturation recovery methods without using CP. Conventional CP scheme with a contact time of 4.5 ms was used for all CP processes in this study. Four dummy scans were applied before signal acquisition to stabilize the spin system.

4.3. Results and discussion

4.3.1. ^{1}H T_1 relaxation behaviors of organic thin films

^{1}H relaxation curves for samples A–F are shown in Fig. 4.4. The relaxation behavior for

the saturation recovery experiment is described as

$$M(\tau) = M_{\infty}\left(1 - \exp\left(-\frac{\tau}{T_1}\right)\right), \tag{4.1}$$

and the relaxation curves in Fig. 4.4 are plotted as

$$1 - \frac{M(\tau)}{M_{\infty}} = \exp\left(-\frac{\tau}{T_1}\right), \tag{4.2}$$

Here, $M(\tau)$ is the magnetization observed for the saturation–recovery experiment and $M_{\infty} = M(\infty)$ is the magnetization at the thermal equilibrium. The experimental curve for sample A is easily reproduced using a single exponential decay curve with a T_1 relaxation time of 2.42 s. The ^{1}H T_1 value is significantly shorter than that for powder crystal $POPy_2$ (57 s), as shown in Table 4.1. The vacuum-deposited $POPy_2$ is in an amorphous state, which is the origin of the short ^{1}H T_1 value. The ^{1}H relaxation times of the CuPc samples, both deposited (sample B) and in the powder poly-crystalline form, are significantly quicker than those of common organic compounds because of the paramagnetic relaxation (Table 4.1). The ^{1}H T_1 is too fast to be determined exactly and was roughly estimated to be less than 1 ms.

Samples C–E with CuPc show clearly different ^{1}H relaxation curves from those of sample A, which consists of a $POPy_2$ thin film without CuPc; the relaxation curves for samples C–E show a steeper slope than that for sample A. In particular, the ^{1}H T_1 relaxation curves for samples C–E do not correspond with any calculated curve with a single T_1 value. Assuming that $POPy_2$ has two domains α and β (Fig. 4.1), we can obtain satisfactory matching using the sum of two exponential functions with two different relaxation times,

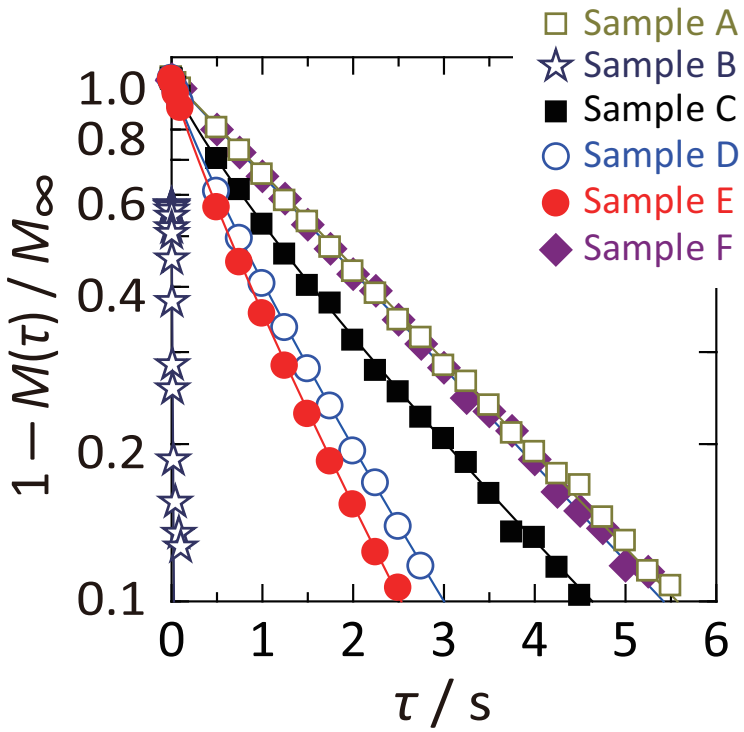

Fig. 4.4. ^{1}H T_1 relaxation curves for samples A–F. The experimental data for samples A, B, and F are fitted with single exponential functions and those for samples C–E are fitted with double exponential functions as described in the text. The simulated curves are plotted with solid lines.

$$1-\frac{M(\tau)}{M_{\infty}}=f_{\alpha}\exp\left(-\frac{\tau}{T_{1,\alpha}}\right)+f_{\beta}\exp\left(-\frac{\tau}{T_{1,\beta}}\right), \tag{4.3}$$

where $T_{1,i}$ is the T_1 relaxation time of the domain i ($i = \alpha$ or β) and f_i is the fraction of the domain i with $f_{\alpha}+f_{\beta}=1$. The α domain is composed of $POPy_2$ located too far from CuPc to bring ^1H magnetization from the heterointerface by ^1H–^1H spin diffusion. We assume that $POPy_2$ in the α domain has the same ^1H T_1 relaxation time as that of sample A. The β domain is located close to the heterointerface between $POPy_2$ and CuPc. In the β domain, the ^1H T_1 relaxation process is dominated by the ^1H–^1H spin diffusion. Although the ^1H T_1 rate should depend on the distance from the heterointerface, we assume a single ^1H T_1 rate in this domain for simplicity. We fitted the experimental curves of samples C–E to Eq. (4.3), while varying

Table 4.1. ^1H T_1 relaxation times by saturation recovery experiments.

	^1H T_1/s (single exponential)	^1H T_1/s (double exponential)
Sample A	2.42	
Sample B	<0.001	
Sample C		2.42 (69%), 0.68 (31%)
Sample D		2.42 (27%), 0.86 (73%)
Sample E		2.42 (18%), 0.81 (82%)
Sample F	2.35	
$POPy_2$ (powder crystal)	57	
CuPc (needle crystal)	<0.001	

the two fitting parameters f_β and $T_{1,\beta}$. The results are shown in Fig. 4.4 with solid lines and also in Table 4.1. As the thickness of the $POPy_2$ layers decreases, f_β, i.e. the share of the β domain that is affected by CuPc, increases. This is the natural consequence of the increase of heterointerface per unit volume of $POPy_2$. Table 4.1 shows that most (more than 70%) $POPy_2$ in samples D and E can be classified into the β domain, indicating that ^1H magnetization penetrates about 50 to 100 nm into the thin films. This means that condition 2 as described in Section 4.1 is satisfied if the organic film thickness is less than 50 to 100 nm. The average displacement $\langle d \rangle$ of ^1H magnetizations during $T_{1,\beta}$ can be estimated by

$$\langle d \rangle = \sqrt{DT_{1,\beta}}\,, \tag{4.4}$$

where D is the spin diffusion coefficient. Inserting D = 1 nm^2/ms, which is a typical value for organic solids [39], we obtain $\langle d \rangle$ of a few tens of nanometers. This qualitatively supports the satisfaction of condition 2 for the 50 to 100 nm organic films.

Sample F had the same layer structure as sample E. The only difference was that CuPc was used in sample E, whereas H_2Pc was used in sample F. However, the relaxation behavior of sample F was significantly different from that of sample E. Sample F showed a ^1H T_1 value of 2.35 s, which is close to that of sample A (2.42 s). This shows that the heterointerface between phthalocyanine and $POPy_2$ produces only a minor effect on the ^1H T_1 relaxation process. The heterointerface may possibly enhance the ^1H T_1 relaxation. For example, the heterointerface might induce a structural or dynamic disorder. The paramagnetic oxygen might be contaminated at the heterointerface. However, we can safely neglect these effects by

comparing the results for samples E and F. The findings confirm that the faster ^{1}H relaxations of $POPy_2$ for samples C–E were induced by close contact with the paramagnetic species, Cu^{2+}, at the molecular level. Condition 1 described in Section 4.1 is satisfied in these films containing vacuum-deposited $POPy_2$/CuPc.

4.3.2. CP/MAS spectra of $POPy_2$ and CuPc/$POPy_2$ films

Figure 4.5(a) and (c) shows ^{31}P CP/MAS spectra of samples A and C–E with a recycle delay of 1 s. Those with a recycle delay of 15 s are shown in Fig. 4.5(b) and (d). Figure 4.5(a) and (b) shows normalized spectra for each peak intensity. From these normalized spectra, it is found that all the spectra show essentially identical line shapes. No detectable paramagnetic shift or broadening was found. Figure 4.5(c) and (d) shows the spectra after division by the total weight of $POPy_2$. These procedures allow us to compare the intensities of the ^{31}P CP/MAS spectra quantitatively. Samples A and C–E showed identical spectra when a relaxation delay of 15 s was employed (Fig. 4.5(d)). This delay is much longer than 5 times of the longest ^{1}H T_1 relaxation times (2.42 s) and allows all of the ^{1}H nuclei to fully relax to the thermal equilibrium state. We did not find significant intensity losses for samples of $POPy_2$ with CuPc (samples C–E) compared with that without CuPc (sample A), indicating that the effect of paramagnetic quenching on signal intensity is negligible and that almost all of the ^{31}P NMR signals of $POPy_2$ are detected. Based on these experimental findings, we can safely neglect the effect of paramagnetic shift, broadening, and quenching of NMR signals by the paramagnetic dopant; and condition 3 described in the Introduction is satisfied if the thickness is greater than 50 nm. This is because these unfavorable effects are only detectable very close to the paramagnetic center and are rapidly suppressed with increasing distance from the paramagnetic center; the dipolar shift and the paramagnetic relaxation are inversely proportional

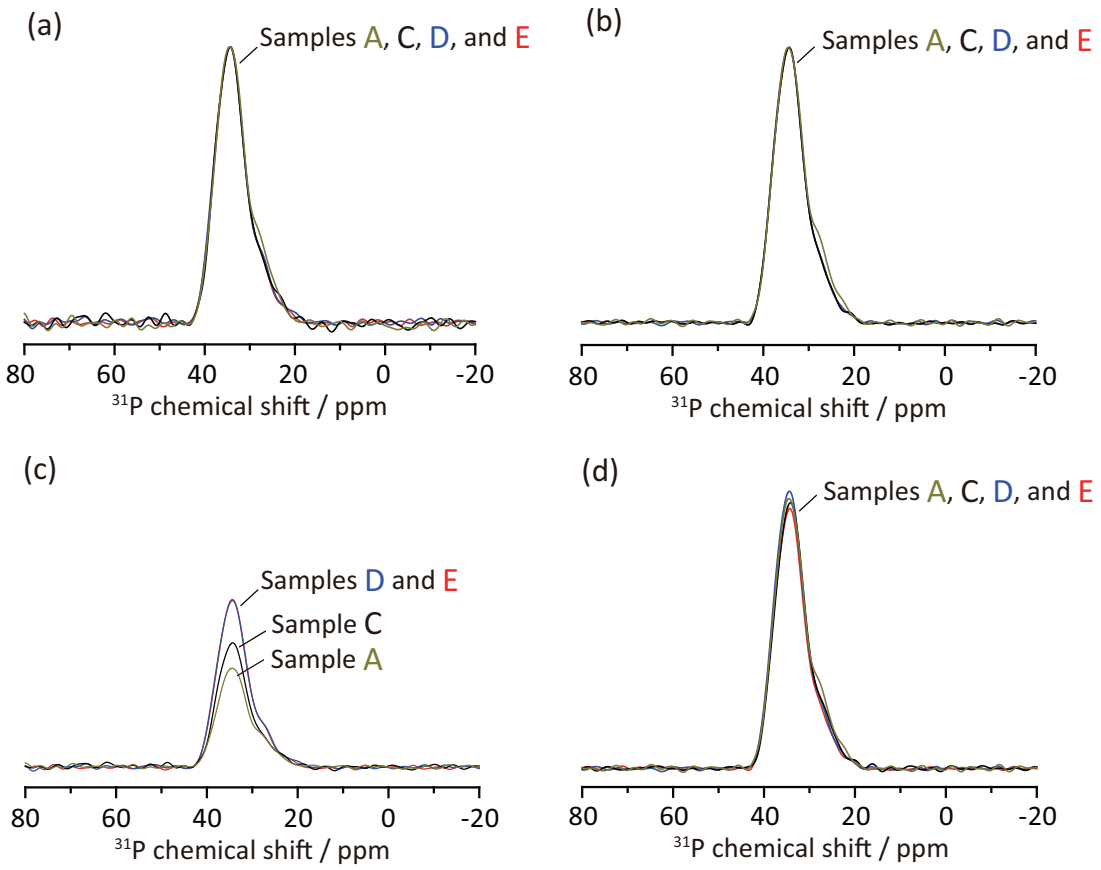

Fig. 4.5. ^{31}P CP/MAS spectra of samples A, C, D and E observed with repetition delays of 1 s (a, c) and 15 s (b, d). The 64 transients for each spectrum were accumulated. The total measuring time is 64 s (a, c) and 960 s (b, d). The spectral intensity is shown after it was normalized with the maximum peak height (a, b) and divided by the total weight of $POPy_2$ for quantitative comparisons of signal intensities (c, d).

to the cube and sixth power, respectively, of the distance between the nuclei and paramagnetic center. In Fig. 4.5(c), sample D shows an almost identical spectrum to that of sample E. This indicates that we can obtain maximum sensitivity enhancement by paramagnetic ion doping if the thickness of the sample is less than 100 nm. The ^{1}H–^{1}H spin diffusion is also utilized in dynamic nuclear polarization (DNP) experiments [40]. The ^{1}H magnetization is produced by polarization transfer from electrons in DNP instead of paramagnetic relaxation and diffused by ^{1}H–^{1}H spin diffusion similarly with the current method. This indicates that the same order of thickness, i.e. 50 to 100 nm, is also optimum for DNP experiments of thin organic films, where the polarization reagent is a thin layer like CuPc.

Figure 4.5(c) demonstrates a 1.7 times signal enhancement by the paramagnetic doping. This decreases the experiment time by 1.7^2 or approximately threefold. This enhancement originates from a shorter ^{1}H T_1 relaxation time of the β domain. The T_1 reduction is much more effective in organic semiconductors where the T_1 times of pristine samples are longer. One example is in OTFTs where organic materials are in crystalline states. The organic materials in such devices have much longer ^{1}H T_1 relaxation times than those in this study. For these samples, extreme effects will be expected. In this study, signal enhancements of ^{31}P CP/MAS are demonstrated. The present method can be applied any CP based experiments and is especially useful for low-sensitivity nuclei such as ^{13}C and ^{15}N, which usually require very long accumulation time or isotopic labeling. For example, ^{13}C CP/MAS measurements, which typically take several hours, can be observed less than one hour if 1.7 times enhancement is achieved.

Signals are enhanced by factors from 1.4 to 4 using recently developed cryogenic probes, both for solution NMR and solid-state NMR [41-43]. According to the empirical equation for the static magnetic field B_0 dependence of the signal-to-noise ratio (SNR), SNR $\propto {B_0}^{3/2}$, the

SNR is enhanced by a factor of 1.8 when comparing the use of 600 and 400 MHz NMR. The use of 800 MHz NMR provides a signal enhancement of 1.5 times in comparison with 600 MHz NMR. Considering this, the method reported in this study is a cost-effective and useful way to enhance the SNR. The methods used in this study can be combined with cryogenic probes and high-field magnets to provide significantly higher SNRs than those provided using those techniques alone.

4.4. Conclusions

A method for enhancing the sensitivity of solid-state NMR, which is very useful for NMR measurements of organic thin-film semiconductors, is proposed. A 1.7 times ^{31}P CP/MAS signal enhancement for $POPy_2$, which is a routinely used material in organic thin-film semiconductors, is achieved by vacuum-deposition of CuPc. The ^{1}H spin bath in $POPy_2$ is composed of α and β domains. In the α domain, the ^{1}H T_1 relaxation time is the same as for pristine $POPy_2$ amorphous thin films without CuPc and the ^{1}H T_1 time in the β domain is dominated by the diffused ^{1}H magnetization from the paramagnetic center of CuPc. No detectable paramagnetic shift, broadening, or quenching was observed. This sensitivity enhancement is satisfactory if the thickness of the organic films is between 50 and 100 nm, as normally used in the organic semiconductors.

Acknowledgments

This study was conducted using the solid-state NMR spectrometer in the Joint Usage/Research Center (JURC) at the Institute for Chemical Research, Kyoto University.

References

[1] C.W. Tang, Appl. Phys. Lett., 48 (1986) 183.

[2] C.W. Tang, S.A. VanSlyke, Appl. Phys. Lett., 51 (1987) 913.

[3] D.W. Andrade, S.R. Forrest, Adv. Mater., 16 (2004) 1585.

[4] Y. Shirota, J. Mater. Chem., 15 (2005) 75.

[5] A.W. Hains, Z. Lianq, M.A. Woodhouse, B.A. Greqq, Chem. Rev., 110 (2010) 6689.

[6] K.T. Kamtekar, A.P. Monkman, M.R. Bryce, Adv. Mater., 22 (2010) 572.

[7] M.C. Gather, A. Köhnen, K. Meerholz, Adv. Mater., 23 (2011) 233.

[8] K. Schmidt-Rohr, Macromolecules, 29 (1996) 3975.

[9] K. Schmidt-Rohr, W. Hu, N. Zumbulyadis, Science, 280 (1998) 714.

[10] A. Lesage, M. Bardet, L. Emsley, J. Am. Chem. Soc., 121 (1999) 10987.

[11] H. Kaji, K. Schmidt-Rohr, Macromolecules, 33 (2000) 5169.

[12] H. Kaji, K. Schmidt-Rohr, Macromolecules, 34 (2001) 7368.

[13] M. Utz, M. Nandagopal, M. Mathai, F. Papadmitrakopoulos, Appl. Phys. Lett., 83 (2003) 4023.

[14] H. Kaji, Y. Kusaka, G. Onoyama, F. Horii, J. Am. Chem. Soc., 128 (2006) 4292.

[15] Y. Nishiyama, T. Fukushima, K. Takami, Y. Kusaka, T. Yamazaki, H. Kaji, Chem. Phys. Lett., 471 (2009) 80.

[16] H. Kaji, H. Hayashi, T. Yamada, M. Fukuchi, S. Fujimura, M. Ueda, S. Kang, T. Umeyama, Y. Matano, H. Imahori, Appl. Phys. Lett., 98 (2011) 113301.

[17] T. Fukushima, H. Kimura, Y. Shimahara, H. Kaji, Appl. Phys. Lett., 99 (2011) 223301.

[18] M. Deschamps, S. Cadars, E. Gilbert, P. Azaïs, E. Raymundo-Pinero, F. Béguin, D. Massiot, Solid State Nucl. Magn. Reson., 42 (2012) 81.

[19] Y. Hamada, H. Kanno, T. Tsujioka, H. Takahashi, T. Usuki, Appl. Phys. Lett., 75 (1999)

1682.

[20] L.-H. Chan, R.-H. Lee, C.-F. Hsieh, H.-C. Yeh, C.-T. Chen, J. Am. Chem. Soc., 124 (2002) 6469.

[21] G. Li, V. Shrotriya, Y. Yao, Y. Yang, J. Appl. Phys., 98 (2005) 043704.

[22] S. van Bavel, E. Sourty, G. de With, K. Frolic, J. Loss, Macromolecules, 42 (2009) 7396.

[23] Y. Min Nam, J. Huh, W. Ho Jo, Sol. Energy Mater. Sol. Cells, 94 (2010) 1118.

[24] L. Xiao, Z. Chen, B. Qu, J. Luo, S. Kong, Q. Gong, J. Kido, Adv. Mater., 23 (2011) 926.

[25] G.N. LaMar, Chem. Phys. Lett., 10 (1971) 230.

[26] R. Freeman, K.G.R. Pachler, G.N. LaMar, J. Chem. Phys., 55 (1971) 4586.

[27] D.S.F. Natusch, J. Am. Chem. Soc., 93 (1971) 2566.

[28] O.A. Gansow, A.R. Burke, G.N. LaMar, J. Chem. Soc. Commun., 8 (1972) 456.

[29] O. A. Gansow, A.R. Burke, W.D. Venon, J. Am. Chem. Soc., 94 (1972) 2550.

[30] L.L. Martin, C.-J. Chang, H.G. Floss, J.A. Mabe, E.W. Hagaman, E. Wenkert, J. Am. Chem. Soc., 94 (1972) 8942.

[31] A. Abragam, The Principles of Nuclear Magnetism, Oxford University Press, London, 1961.

[32] R.H. Meinhold, K.J.D. MacKenzie, Solid State Nucl. Magn. Reson., 5 (1995) 151.

[33] H.W. Long, R. Tycko, J. Am. Chem. Soc., 120 (1998) 7039.

[34] N.P. Wickramasinghe, M. Kotecha, A. Samoson, J. Past, Y. Ishii, J. Magn. Reson., 184 (2007) 350.

[35] P.N.M. Anjos, H. Aziz, N.-X. Hu, Z.D. Popovic, Org. Electron., 3 (2002) 9.

[36] S.M. Tadayyon, H.M. Grandin, K. Griffiths, P.R. Norton, H. Aziz, Z.D. Popvic, Org. Electron., 5 (2004) 157.

[37] T. Oyamada, H. Sasabe, C. Adachi, S. Murase, T. Tominaga, C. Maeda, Appl. Phys. Lett.,

86 (2005) 033503.

[38] T. Matsushima, C. Adachi, Jpn. J. Appl. Phys., 46 (2007) L861.

[39] K. Schmidt-Rohr, H.W. Spiess, Multidimensional Solid-State NMR and Polymers, Academic Press, London, 1994.

[40] P.C.A. van der Wel, K.-N. Hu, J. Lewandowski, R.G. Griffin, J. Am. Chem. Soc., 128 (206) 10840.

[41] P. Styles, N.F. Soffe, C.A. Scott, D.A. Cragg, F. Row, D.J. White, P.C.J. White, J. Magn. Reson., 60 (1984) 397.

[42] P.F. Flynn, D.L. Mattiello, H.D.W. Hill, A.J. Wand, J. Am. Chem. Soc., 122 (2000) 4823.

[43] T. Mizuno, K. Hioka, K. Fujioka, K. Takegoshi, Rev. Sci. Instrum., 79 (2008) 044706.

Chapter 5

Enhancement of Hole Injection in Organic Light-Emitting Diodes by Self-Assembled Monolayer

5.1. Introduction

Since the demonstration of electroluminescence (EL) from the innovative layered organic thin film [1], organic light-emitting diodes (OLEDs) have drawn increasing attention for their practical use as EL devices. As well as the researches pursuing excellent properties of the respective layers, the modification of the interfaces has been a key research topic, because the interfaces considerably influence the charge-injection, charge-confinement, and driving voltage. For the enhanced hole-injection and the reduced turn-on voltage, self-assembled monolayers (SAMs) have been used as modifiers of indium tin oxide (ITO) anode. Nüesch et al. [2] reported a reduced turn-on voltage of single-layered devices using α-carboxylated oligophenylene, where the ITO electrode was covered with oligophenylene via physical adsorptions between the carboxylic acid moiety and the ITO surface. The enhanced hole-injection was explained by the dipole moments of the molecules adsorbed on the ITO surface; the dipole moments can reduce the effective work function of ITO and hence the turn-on voltage [2,3]. Huang et al. [4] demonstrated an enhanced luminance even using a non-conjugated alkylsilane as a modifier chemically attachable to the ITO surface. The enhanced luminance was explained by the increased electron-blocking property owing to the modifiers introduced between the ITO electrode and hole-transport layer (HTL). Even though the non-conjugated alkyl layer works as an insulator for the hole-injection, it can reduce the mismatch of the surface energy between the hydrophilic ITO surface and the hydrophobic HTL [5], allowing a good compatibility of the ITO surface and HTL, and hence a reduced turn-on

voltage. The SAM-modified interface suppresses the crystallization of the overlaying HTL upon heating even above the glass transition temperatures of HTL materials [6]. The suppression of crystallization is an additional advantage brought about by using SAMs as a modifier.

As physically-adsorbed modifiers, chloride and acid derivatives, including phosphonic, sulfonic, and carboxylic acids, have been used [3,7-9]. For more stable SAM−ITO interfaces, chemically-bonded modifiers are considered to be preferable, because the rigid covalent bond prevents the exfoliation at the interface. Organo-alkoxysilane [4,13-19], silazane [20], and chlorosilane [21-23] have been used as modifiers, for which facile sol-gel reactions have often been used. Vapor phase reactions are also often used for the silanization [24]. However, they require high temperatures in many cases. This also limits kinds of modifiers, since the modifier should have a high thermal stability and a sufficiently high vapor pressure. In the sol−gel silanization, diluted silane molecules are immobilized on ITO surface in organic solvents, such as toluene [13-16,19], ethanol [16], and hexane [22]. The silanization includes two reaction steps [24-26]. The first step is the hydrolysis of silanes with water molecules adsorbed on a substrate surface or incorporated in a solvent to generate a silanol (Si-OH). The second step is the condensation of two silanols to form a siloxane bond on the ITO surface. The rate of hydrolysis significantly depends on the amount of water, and hence, the amount of water considerably influences on the resultant SAM structure on the ITO surface. Also, pH in a reaction solution has a significant impact on the SAM structure, because the mechanism and the kinetics of condensation reaction are completely different between under acidic and basic conditions [27,28]. When the hydrolysis and the condensation proceed via base-catalyzed mechanism, ramified silane polymers with widely-distributed molecular weights are formed, and the polymers subsequently form isolated particles. On the other hand, when the hydrolysis

and the condensation proceed via acidic-catalyzed mechanism, homogeneous polymerization leads to mostly linear silane polymers with narrowly-distributed molecular weights. In addition to these factors, the rate of the condensation also depends on the amount of the silane molecule in a system. Therefore, the control of the three factors, i.e., catalytic condition, water amount, and the concentration of silane, is crucial for precise formation of SAMs and, therefore, for achieving excellent charge-injection properties of devices.

As described above, there are a number of studies targeting superior device performances by using novel modifiers. However, the systematic studies on preparation conditions for the SAM formation on ITO have not been reported. This may partly be because the amount of water and the pH are hardly controllable in hydrophobic solvents frequently used in the previous studies, such as toluene and hexane, which are immiscible with water. In this study, we investigated SAM formations of an alkylsilane, pentyltriethoxysilane (PTES), on ITO in an amphiphilic solvent, tetrahydrofuran (THF), which is miscible with water and can precisely control the amount of water and catalytic conditions. We, for the first time, systematically studied how the SAM structure and the resultant hole-injection property depend on amount of water, concentration of PTES, and catalytic condition in the reaction solution. The results obtained here would provide knowledge on the conditions of SAM formation for the high-performance OLEDs.

5.2. Experimental procedures

5.2.1. Substrate preparation

An ITO patterned glass substrate, 55 nm ITO deposited on a soda-lime-silica glass with 0.7 mm thickness covered with 23 nm SiO_2 layer, sheet resistance of 50 Ω /sq, was used as a

cathode. The substrate was swabbed with acetone, followed by ultrasonic cleaning in detergent, ultrapure water, acetone, and isopropyl alcohol. The substrate was then boiled in isopropyl alcohol and placed in an ultraviolet−ozone treatment chamber (PL16-110, Sen Lights Co.). For the silane SAM formation, a freshly treated substrate was used without storage.

5.2.2. Silane SAM formation

Nitric Acid (HNO_3: Nacalai Tesque Inc., 0.1 M) and ammonium hydroxide (NH_3: Hayashi Pure Chemical Industries, 28 wt%) were used as catalysts after being diluted with ultrapure water. Tetrahydrofuran (THF: Wako Pure Chemicals Industries, dehydrated, no stabilizer) and pentyltriethoxysilane (PTES: Tokyo Chemical Industry Co. Ltd.) were used as a solvent and a silica source, respectively.

First, THF and a given concentration of HNO_3 or NH_3 aqueous solution were mixed in a glass vessel. Under stirring in an ice water bath, PTES was added and kept stirring for 5 min. After stirring was stopped, the freshly treated ITO substrate was soaked in the solution, sealed, and kept at 40 °C for 24 h. The substrate was retrieved, rinsed with chloroform, and supersonically cleaned in chloroform for 10 min. Finally, the substrate was baked at 100 °C under vacuum to remove volatile residuals. The SAM-modified ITO substrates were used for device fabrication immediately. Hereafter, a H_2O/PTES ratio and a PTES concentration in a THF solvent are denoted as r and C_{PTES}, respectively. The value of r was controlled with the amount of catalytic aqueous solution, and thus the catalytic aqueous solutions were employed as a water source as well as a catalyst. In the present study, the sample prepared with C_{PTES} = 0 mM denoted as bare-ITO.

5.2.3. Silane SAM characterization

Contact angles, θ, of SAM-modified ITO substrates were measured with a contact-angle meter (Drop Mater 700, Kyowa Interface Science Co. Ltd.) using distilled water. The measurements were performed at five different points for respective substrates and the data were averaged. Surface morphology of the substrates was observed by an atomic force microscope (AFM: SPA400+SPI3800N, SII Nano Technology Inc.) operating in a dynamic force mode (DFM).

5.2.4. Device fabrication and characterization

We used *N*,*N*′-di(1-naphthy)-*N*,*N*′-diphenylbenzidine (α-NPD) as a hole-transport layer, tris(8-hydroxyquinoline) aluminum(III) (Alq_3) as emissive and electron-transport layer, lithium fluoride (LiF: Furuuchi Chemical Co. Ltd, 99.99%) as an electron-injection layer, and aluminum (Al: Kojundo Chemical Lab. Co. Ltd., 99.999%) as a cathode material. All the reagents were used as received.

Hole only devices (HODs) and OLED devices were fabricated on the SAM-modified ITO substrate by successive vapor deposition of organic layers, followed by the deposition of LiF and Al. HODs were composed of ITO-SAM/NPD 100 nm/Al 100nm, whereas OLED devices were composed of ITO-SAM/NPD 50 nm/Alq_3 50 nm/ LiF 0.6 nm/Al 100 nm. The deposition was carried out under 10^{-5} Pa. The deposition rates were 3 Å·s^{-1} for the organic layers and Al, and 0.1 Å·s^{-1} for LiF. The devices thus fabricated have four active areas with 4 mm^2 each. Current density−voltage−luminance ($J-V-L$) characterization was performed using a computer-controlled source meter (Source Meter 2400, Keithley Instruments Inc.) equipped with a spectroradiometer (SR-3, TOPCON Co.). The characterization was carried out on all of the four active areas, providing information about reproducibility of the SAM formation on the

ITO surfaces.

5.3. Results and Discussion

5.3.1. SAM formations under acid and basic conditions

First, we examined a surface modification of ITO substrates with SAM and fabricated OLEDs with using the modified substrates. Figure 5.1 shows the optical microscope images of the electroluminescence from the OLEDs. The images clearly indicate that in-plane uniformity of emission was considerably influenced by the catalytic condition for the SAM formation. Homogeneous emission was observed when the SAM was formed under the acidic condition (Fig. 5.1(a)), while significantly inhomogeneous emission was observed when it was formed under the basic condition (Fig. 5.1(b)). The luminance for the acidic condition (601

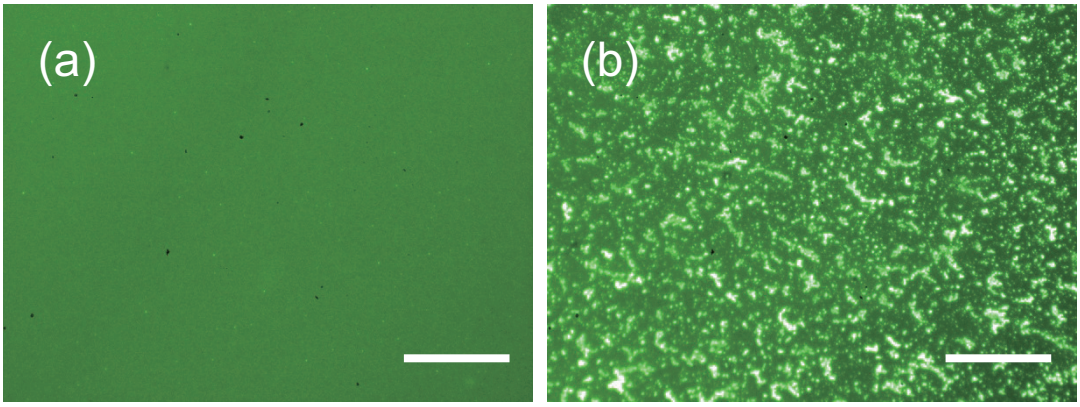

Fig. 5.1. Optical microscope images of the OLEDs under the applied voltage of 9 V. The SAM layers were formed with (a) acidic (0.01 M HNO_3) and (b) basic (0.01 M NH_3) catalysts under the condition of r = 15 and C_{PTES} = 250 mM. The OLEDs consist of ITO-SAM/NPD 50 nm/Alq_3 50 nm/ LiF 0.6 nm/Al 100 nm. White bar = 100 μm in both the images.

cd/m^2) was much larger than that for the basic condition (<100 cd/m^2) at an applied voltage of 6 V for the devices. Namely, the luminescence was stronger and more homogeneous for the acidic condition than the basic condition. Figure 5.2 shows the current density−voltage ($J-V$) and luminance−voltage ($L-V$) characteristics of the two OLEDs shown above (with the SAM formation under the acidic and basic conditions). For each sample, the measurements were performed on the four active areas (2 mm x 2 mm) and all the four data are plotted. The $J-V$ (Fig. 5.2(a)) and $L-V$ (Fig. 5.2(b)) plots reveal that the acidic condition led to lower turn-on voltages and higher luminance than the basic condition. Moreover, the four data for the basic condition were scattered, while those for the acidic condition were more reproducible. Thus, the in-plane uniformity of $J-V$ and $L-V$ characteristics highly depends on the catalytic conditions.

Figure 5.3 shows the $J-V$ plots of HODs for the 0.1, 0.01, and 0.001 M HNO_3, and 0.1 and 0.01 M NH_3 catalytic conditions. The acidic conditions exhibited higher hole-injection properties than the basic conditions, as in the case of OLEDs. In the studied case, the highest hole-injection property was achieved with 0.01 M HNO_3. The difference in the hole-injection property would be related to the surface morphologies of SAM-modified ITO substrates, as discussed below.

Figure 5.4 shows the AFM images of the SAM-modified ITO substrates prepared with (a) acidic (0.01 M HNO_3) and (b) basic (0.01 M NH_3) catalysts. In the acidic condition (Fig. 5.4(a)), the roughness of the SAM was virtually the same as that of the bare ITO, indicating the coverage of a homogeneous silane layer on the ITO substrate. On the other hand, the basic condition (Fig. 5.4(b)) resulted in an inhomogeneous formation of coarse particles with the size of several micrometers in length and 30 nm in thickness. This confirms that the different luminance in Fig. 5.1 originates from the different homogeneity of the silane layers on the respective ITO surfaces. The contact angle of the modified surface was 93.6 ± 1.8° and 84.4 ±

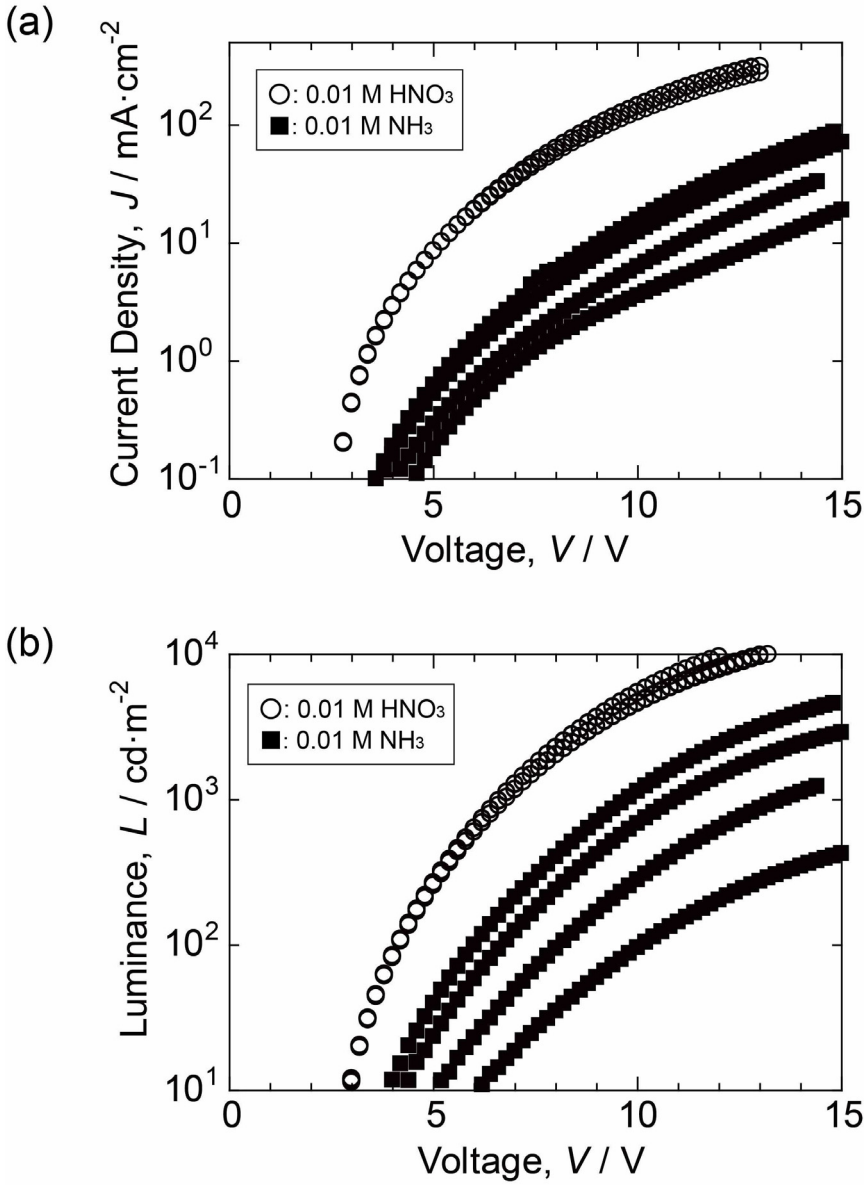

Fig. 5.2. (a) $J-V$ and (b) $L-V$ characteristics of the OLEDs composed of ITO-SAM/NPD 50 nm/Alq_3 50 nm/ LiF 0.6 nm/Al 100 nm. The SAM layers were prepared with 0.01 M HNO_3 (open circles) and 0.01 M NH_3 (closed squares) as catalysts, under the condition of r = 15 and C_{PTES} = 250 mM. The measurements were performed on the four active areas and all the data are plotted for both the devices.

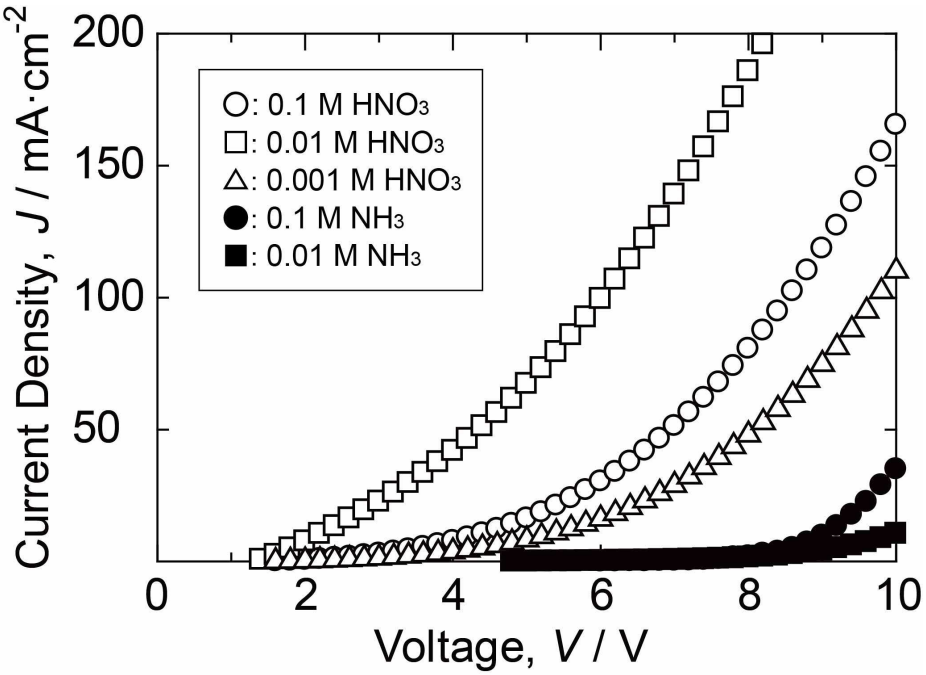

Fig. 5.3. $J-V$ characteristics of HODs composed of ITO-SAM/NPD 100 nm/Al 100 nm. SAM formation was performed with the condition of r = 10 and C_{PTES} = 250 mM using various catalysts; open circles: 0.1 M HNO_3, open squares: 0.01 M HNO_3, open triangles: 0.001 M HNO_3, closed circles: 0.1 M NH_3, closed squares: 0.01 M NH_3.

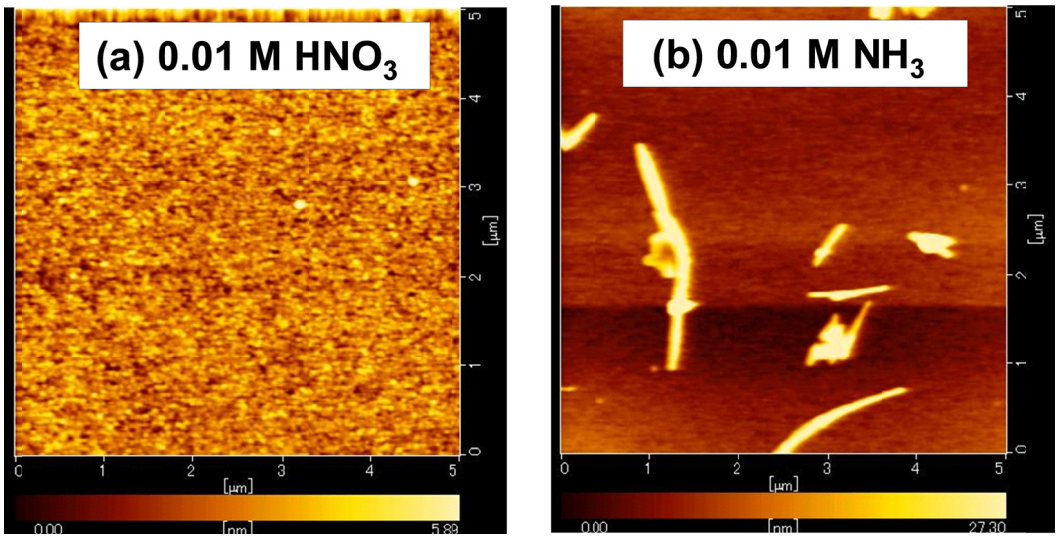

Fig. 5.4. AFM images of SAM-modified ITO substrates prepared under the condition of r = 10 and C_{PTES} = 250 mM with (a) acidic (0.01 M HNO_3) and (b) basic (0.01 M NH_3) catalysts. The image areas correspond to 5 μm × 5 μm.

0.5° with 0.01 M HNO_3 and 0.01 M NH_3, respectively, confirming a higher coverage of hydrophobic PTES on the ITO substrate under the acidic condition. The observation of coarse particles in Fig. 5.4(b) is explained by the fact that base-catalyzed condensation of silicate species produces ramified polymers with widely-distributed molecular weights [27,28]. The coarse particles are derived from the well-grown polymeric silicates which are formed on the ITO surface and/or attached onto the surface. On the other hand, acid-catalyzed condensation of silicate species is favorable for the formation of homogenous polymer networks [27,28], which leads to the coverage of SAM on the ITO surface without segregation. Moreover, it is well-known that the rate of condensation is minimized around isoelectric point (IEP) of polymerizing silicates [29,30]. For example, the rate of condensation becomes extremely slow at pH = 2.0−2.5 and 4 for silica and methylsilsesquioxane ($MeSiO_{1.5}$), respectively. In this study, the use of the condition, 0.01 M HNO_3, realized a relatively moderate condensation reaction of PTES, leading to the formation of a homogeneous silane layer.

5.3.2. Dependence of the H_2O/PTES ratio, *r*

Figure 5.5 shows the *J*−*V* plots of the HODs at various *r* values under an acidic (0.01 M HNO_3) condition. With an increase of *r*, the hole-injection property was improved gradually from *r* = 3 to *r* = 15. The *J* increased from 11.9 mA·cm^{-2} at *r* = 3 to 219 mA·cm^{-2} at *r* = 15 at an applied voltage of 6 V. Further increase in *r* lowered the hole-injection property. For PTES, *r* = 1.5 is the stoichiometric condition for hydrolysis and condensation. However, the reactions generally take long reaction times to complete at *r* = 1.5 [27]. Thus, the excessive amount of water (*r* > 1.5) was required for the complete coverage of the ITO surface for the present reaction time, 24 h, and at the present reaction temperature, 40 °C. The best *r* was 15 in this case. The contact angle was 93.6 ± 1.8° at *r* = 15 and 79.9 ± 0.5 ° at *r* = 30. The

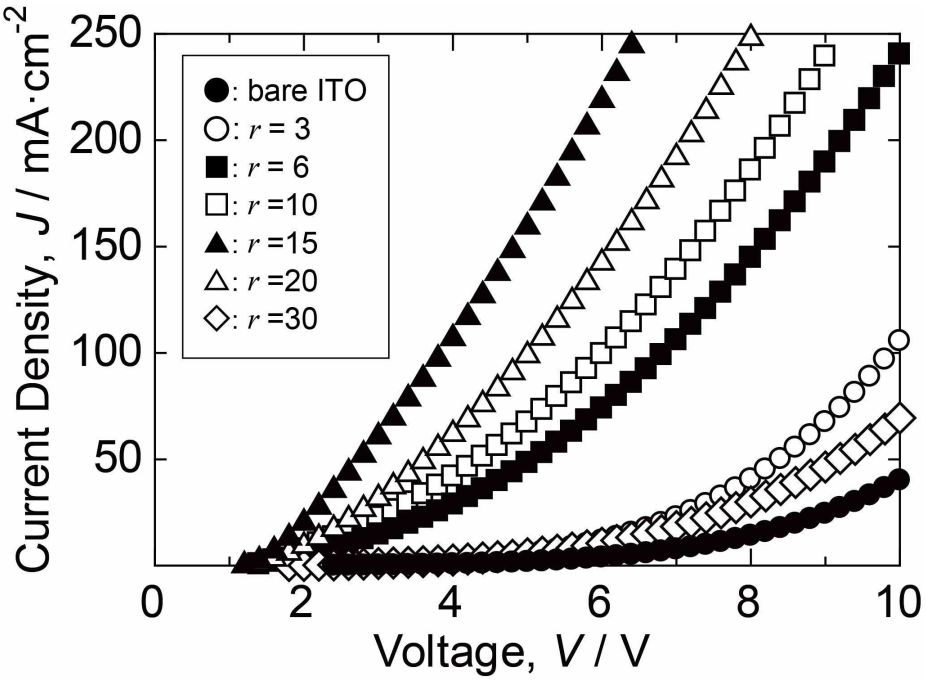

Fig. 5.5. The r-dependence of $J-V$ characteristics of HODs composed of ITO-SAM/NPD 100 nm/Al 100 nm. 0.01 M HNO_3 was used as a catalyst and C_{PTES} = 250 mM for all the devices. closed circle: bare ITO, open circle: r = 3, closed square: r = 6, open square: r = 10, closed triangle: r = 15, open triangle: r = 20, open rhombus: r = 30.

smaller contact angle at r = 30 suggests that the condensation reaction occurred in the solvent phase rather than the ITO surface. The enhanced condensation in the solvent phase can be related to the formation of oligomers with the low connectivity to an ITO surface. A previous report [31] revealed that the oligomers with a cage structure tended to form with increasing r in organosiloxane sol−gel systems. Since the oligomers with a cage structure have no contribution to the formation of SAMs, they are isolated in solvents. The insufficiently-modified ITO would explain the observed decrease in the hole-injection property at r > 15. Also, the small contact angle at r = 30 would be related to the increased silanols on the immobilized modifiers. An increase in r enhances the hydrolysis of PTES and produces hydrophilic silanols more effectively, leading to the small contact angle of ITO surface. The small contact angles provided by the non-condensed silanols are further discussed below based on the results of Fig. 5.7.

5.3.3. Influence of the PTES concentration, C_{PTES}

Figure 5.6 shows the $J-V$ plots of the HODs at various C_{PTES} values in an acidic (0.01 M HNO_3) condition at r = 15. The hole-injection property was improved with an increase of C_{PTES}. The J at applied voltage of 6 V increased from 3.94 to 206 mA·cm^{-2}, as C_{PTES} increased from 0 to 250 mM. Figure 5.7 shows the contact angle, θ, of the SAM-modified ITO surface as a function of C_{PTES}. The θ decreased from C_{PTES} = 0 to 42 mM and increased from C_{PTES} = 42 to 250 mM. The decrease in θ in the low C_{PTES} regime suggests the immobilization of hydrophilic species on ITO surface. Since the low C_{PTES} is an insufficient condition for the SAM formation, the silane layer unlikely developed on the entire surface of ITO. Thus, the immobilization of hydrolyzed PTES with hydrophilic silanols would decrease θ, as depicted in the inset of Fig. 5.7. In fact, the presence of silanols in silica networks was evidenced in the

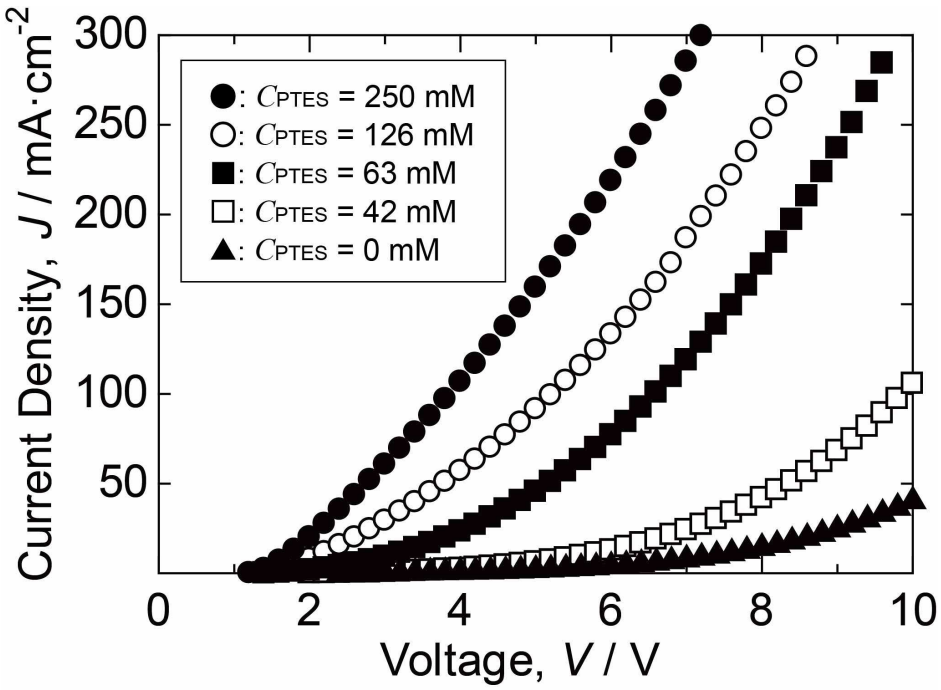

Fig. 5.6. Influence of C_{PTES} on $J-V$ characteristics of HODs composed of ITO-SAM/NPD 100 nm/Al 100 nm; closed circles: 250 mM, open circles: 126 mM, closed squares: 63 mM, open squares: 42 mM, closed triangles: 0 mM. 0.01 M HNO_3 was used as a catalyst and r = 15 for all the devices.

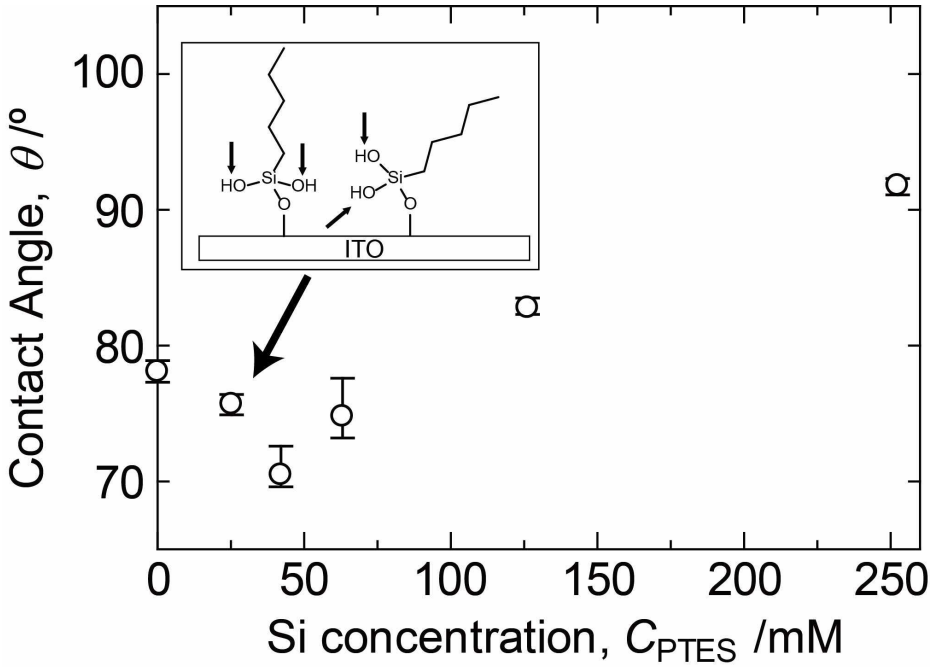

Fig. 5.7. Contact angles as a function of C_{PTES}.

silica gels prepared under the acid-catalyzed condensations [27,32,33]. Whereas, in the condition of C_{PTES} from 42 to 252 mM, θ increased due to the formation of siloxane network and the coverage of the ITO surface with the hydrophobic silane layer. At C_{PTES} = 250 mM, θ value virtually reached a value expected for the full coverage of PTES [4,34], meaning that 250 mM is large enough to fully cover the ITO surface.

In this way, with an appropriate pH (0.01 M HNO_3), water amount (r = 15), and PTES concentration (C_{PTES} = 250 mM), the acidic condition reproducibly provided a remarkably uniform PTES-modified ITO surface, which cannot be achieved in basic conditions. The OLEDs fabricated under this condition exhibited excellent *J-V* and *L-V* characteristics. The homogeneous PTES layer covalently-bonded to the ITO surface works as a good compatible layer with HTL, helping the hole-injection significantly. Thus, the acid-catalyzed silanization can be a very useful method for the precise modification of ITO substrates for the applications to OLED and other electronic devices. We used THF as a solvent in this work. PTES forms organosiloxane network on ITO with the formula of $RSiO_{1.5}$ through the hydrolysis and condensation reactions. Due to its hydrophobicity, oligomeric compounds of organosiloxanes easily phase separate from an aqueous solution or lower alcohols, resulting in the precipitation of amorphous compounds [35,36]. The use of THF as a solvent allows an accurate control of the water content without the precipitation of silane compounds. Although the variation of the hole-injection property can be explained on the basis of the coverage of SAM on the ITO surface, the thickness of the silane layer should also influence on the hole-injection property; the silane layer on the ITO surface works as an insulator, and hence, the formation of a thick silane layer is undesirable. Considering the reaction mechanisms of PTES, the formation of a thick silane layer is unavoidable in the case of the base-catalyzed reactions. Therefore, the acid-catalyzed reactions would be preferable also in this sense.

5.4. Conclusions

By using facile sol−gel route, the conditions for SAM formation on ITO were systematically studied. The relationship between the preparation conditions of SAM and the resultant device properties was investigated by using OLEDs and HODs fabricated on SAM-modified ITO substrates. The emissions from OLEDs and the hole-injection properties of HODs revealed that the acidic conditions are favorable for the reproducible formation of SAM on the ITO surface. The SAM formation under the acidic conditions allows the homogeneous coverage of a silane layer on the ITO substrates, which leads to improved hole-injection properties from the anode. On the other hand, the use of basic conditions results in the inhomogeneous coverage of a silane layer on the ITO substrates and the decreased hole-injection from the anode. The choice of r and C_{PTES} also affect the kinetics of hydrolysis and condensation reactions of PTES, and hence the resultant SAM structures and hole-injection properties. The hole-injection property of HODs depends on the coverage of SAM on the ITO surface; the hole-injection property improved with increased coverage of SAM on the ITO surface. As a result, the highest hole-injection was achieved when SAM formation was performed under r = 15 and C_{PTES} = 250 mM, with 0.01 M HNO_3 as a catalyst. The results obtained here suggest that the device performance of OLEDs and HODs can improve drastically by choosing appropriate SAM formation conditions.

References

[1] C. W. Tang, S. A. VanSlyke, Appl. Phys. Lett., 51 (1987) 913.

[2] F. Nüesch, L. Si-Ahmed, B. François, L. Zuppiroli, Adv. Mater., 9 (1997) 222.

[3] F. Nüesch, F. Rotzinger, L. Si-Ahmed, L. Zuppiroli, Chem. Phys. Lett., 288 (1998) 861.

[4] Q. Huang, G. A. Evmenenko, P. Dukka, P. Lee, N. R. Armstrong, T. J. Marks, J. Am. Chem. Soc., 127 (2005) 10227.

[5] H. Klauk, Chem. Soc. Rev., 39 (2010) 2643.

[6] J. G. C. Veinot, T. J. Marks, Acc. Chem. Res., 38 (2005) 632.

[7] S. F. J. Appleyard, S. R. Day, R. D. Pickford, M. R. Willis, J. Mater. Chem., 10 (2000) 169.

[8] C. Ganzorig, K.-J. Kwak, K. Yagi, M. Fujihira, Appl. Phys. Lett., 79 (2001) 272.

[9] M. Carrara, F. Nüesch, L. Zuppiroli, Synth. Met., 121 (2001) 1633.

[10] J. Morgado, N. Barbagallo, A. Charas, M. Matos, L. Alcácer, F. Cacialli, J. Phys. D: Appl. Phys., 36 (2003) 434.

[11] S. Khodabakhsh, D. Poplavskyy, S. Heutz, J. Nelson, D. D. C. Bradley, H. Murata, T. S. Jones, Adv. Funct. Mater., 14 (2004) 1205.

[12] S. Besbes, H. Ben Ouada, J. Davenas, L. Ponsonnet, N. Jaffrezic, P. Alcouffe, Mater. Sci. Eng. C, 26 (2006) 505.

[13] J. Lee, B.-J. Jung, J.-I. Lee, H. Y. Chu, L.-M. Do, H.-K. Shim, J. Mater. Chem., 12 (2002) 3494.

[14] P. Sigaud, J.-N. Chazalviel, F. Ozanam, J. Appl. Phys., 92 (2002) 992.

[15] Q. Huang, J. Li, G. A. Evmenenko, P. Dutta, T. J. Marks, Chem. Mater., 18 (2006) 2431.

[16] L.-W. Chong, Y.-L. Lee, T.-C. Wen, Thin Solid Films, 515 (2007) 2833.

[17] T. Mori, S. Nishino, T. Nishikawa, S. Ogawa, Org. Electron., 9 (2008) 63.

[18] O. P. Khatri, K. Murase, H. Sugimura, Jpn. J. Appl. Phys., 47 (2008) 5048.

[19] O. P. Khatri, K. Murase, H. Sugimura, Langmuir, 24 (2008) 3787.

[20] C.-C. Hsiao, C.-H. Chang, M.-C. Hung, N.-J. Yang, S.-A. Chen, Appl. Phys. Lett., 86 (2005) 2235051.

[21] Y. Koide, Q. Wang, J. Cui, D. D. Benson, T. J. Marks, J. Am. Chem. Soc., 122 (2000) 11266.

[22] R. A. Hatton, S. R. Day, M. A. Chesters, M. R. Willis, Thin Solid Films, 394 (2001) 292.

[23] B. Choi, J. Rhee, H. H. Lee, Appl. Phys. Lett., 79 (2001) 2109.

[24] J. Duchet, B. Chabert, J. P. Chapel, J. F. Gérard, J. M. Chovelon, N. Jaffrezic-Renault, Langmuir, 13 (1997) 2271.

[25] M. E. McGovern, K. M. R. Kallury, M. Thompson, Langmuir, 10 (1994) 3607.

[26] A. Ulman, An Introduction to Ultrathin Organic Films from Langmuir−Blodgett to Self-Assembly, Academic Press, San Diego, 1991.

[27] C. J. Brinker, G. W. Scherer, Sol–Gel Science: The Physics and Chemistry of Sol–Gel Processing, Academic Press, San Diego, 1990.

[28] R. K. Iler, The Chemistry of Silica, Willy, New York, 1979.

[29] A. H. Boonstra, J. M. E. Baken, J. Non-Cryst. Solids., 122 (1990) 171.

[30] H. Dong, M. A. Brook, J. D. Brennan, Chem. Mater., 17 (2005) 2807.

[31] L.-H. Lee, W.-C. Chen, W.-C. Liu, J. Polym. Sci., Part A: Polym. Chem., 40 (2002) 1560.

[32] H. Kaji, K. Nakanishi, N. Soga, T. Inoue, N. Nemoto, J. Non-Cryst. Solids, 181 (1995) 16.

[33] H. Kaji, K. Nakanishi, N. Soga, J. Non-Cryst. Solids, 185 (1995) 18.

[34] A. V. Rao, M. M. Kulkarni, D. P. Amalnerkar, T. Seth, Appl. Surf. Sci., 206 (2003) 262.

[35] M. Park, S. Komarneni, J. Choi, J. Mater. Chem., 33 (1998) 3817.

[36] D. A. Loy, B. M. Baugher, C. R. Baugher, D. A. Schneider, K. Rahimian, Chem. Mater., 12 (2000) 3624.

Chapter 6

Phase Separation Behavior of Regioregular Poly(3-hexylthiophene) and [6,6]-Phenyl-C_{61}-Butyric Acid Methyl Ester in Bulk Heterojunction Organic Solar Cells Analyzed by Solid-State NMR

6.1. Introduction

Organic solar cells (OSCs) have attracted significant attention for their low-cost solar energy conversion. In extensive research on various OSCs, bulk heterojunction OSCs consisting of regioregular poly(3-hexylthiophene-2,5-diyl) (rrP3HT) and [6,6]-phenyl-C_{61}-butyric acid methyl ester ($PC_{61}BM$) have shown excellent performance as donors and acceptors, respectively, and have been widely studied (Fig. 6.1) [1-6]. One point of interest for the OSC systems is the effect of thermal annealing treatments. Padinger et al. found that the power conversion efficiency (PCE) increases from 0.4 % to 2.5 % by annealing at 75 °C for 4 min [1]. Ma et al. reported a drastic increase in PCE from 0.8 % to 5.1 % by annealing at 150 °C for about 30 min [2]. Similar trends have also been reported in refs 3–6. According to these studies, thermal annealing treatment is a very easy and inexpensive way to improve the performance of OSCs. Scientifically, it is important to understand what

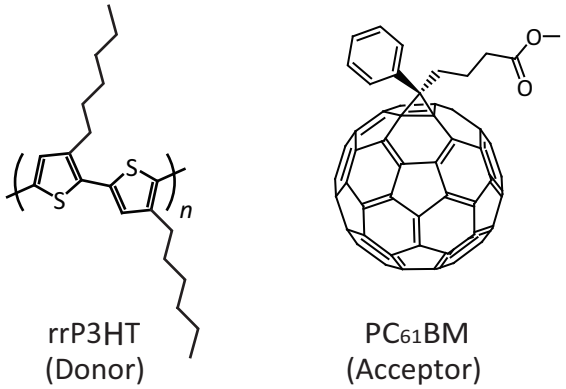

Fig. 6.1. Chemical structures of rrP3HT and $PC_{61}BM$.

happens in the films during thermal annealing. Photoelectric conversion occurs via generation of excitons through the absorption of light, diffusion of excitons toward donor/acceptor interfaces, charge separation at the interface and formation of free carriers (holes and electrons), and transport of free carriers toward electrodes. During the processes, back electron transfer (recombination of holes and electrons) also occurs, which degrades the performance of OSCs. These processes occur at different size scales. Therefore, investigation of donor–acceptor structures at different size scales is important in understanding the efficiency of OSCs.

Solid-state nuclear magnetic resonance (NMR) is a useful tool to study local structures in organic materials [7]. Recently, it has also been applied to the analysis of materials for organic light-emitting diodes [8-10] and organic solar cells [11-14], and it is expected to provide important knowledge on the abovementioned thermal annealing effect [13-18]. In this study, we investigated the change in the donor–acceptor structure in rrP3HT/$PC_{61}BM$ systems during thermal annealing by spin-lattice relaxation measurements in solid-state NMR, which reveals the miscibility between rrP3HT and $PC_{61}BM$ at different hierarchical levels. A clear relationship is found between the PCE of the OSC systems and the donor–acceptor structure revealed by solid-state NMR.

6.2. Experimental procedures

6.2.1. Fabrications of Organic solar cells

Poly(3,4-ethylene dioxythiophene):poly(styrenesulfonate) (PEDOT:PSS) (CLEVIOS™ P VP AI 4083, HC Starck) was spin-coated with 40 nm thickness from aqueous solution on indium–tin–oxide (ITO) substrate (the thickness of the ITO was 150 nm). The substrate was dried at 110 °C for 30 min in vacuum. An active layer of 120 nm, consisting of rrP3HT and

$PC_{61}BM$ at a weight ratio of 1:1, was spin-coated on the PEDOT:PSS layer using chloroform. The molar ratio of the monomer unit of rrP3HT and $PC_{61}BM$ was 4.4:1. Here, the as-cast sample is referred to as the nonannealed sample. For annealed samples, the ITO substrates with the PEDOT:PSS and the active layers were isothermally annealed at 150 °C for 5, 15, and 30 min in vacuum. Subsequently, 0.6 nm of lithium fluoride (LiF) and a 100 nm thick Al electrode were deposited onto the active layer of the nonannealed and the three annealed samples in this order by thermal evaporation at 2.5×10^{-5} Pa. The current density–voltage (*J*–*V*) characteristics of the OSCs were measured using a solar simulator (OTENTOSUN II) under 100 mW cm^{-2} white-light illumination (air mass 1.5 conditions).

6.2.2. Sample preparations

Samples for wide-angle X-ray diffraction (WAXD) and solid-state NMR experiments were prepared by drop casting a mixed solution of 1:1 (w/w) rrP3HT:$PC_{61}BM$ in chloroform onto a Petri dish and drying at room temperature. Annealed samples were isothermally annealed at 150 °C for 5, 15, and 30 min under an N_2 atmosphere. The nonannealed and annealed films were scraped off using a sharp blade and approximately 300 mg of the samples were obtained for the respective films. Nonannealed films and films isothermally annealed at 150 °C for 30 min consisting only of rrP3HT (pure rrP3HT) or only of $PC_{61}BM$ (pure $PC_{61}BM$) were also prepared by the same procedure.

6.2.3. Structural analyses

WAXD data were recorded at room temperature on a Rigaku RINT 2000 diffractometer using Cu-*K*α radiation and operating at 300 mA and 40 kV. Solid-state NMR measurements were conducted on a Chemagnetics CMX-400 Infinity spectrometer operating under a static

magnetic field of 9.4 T. A double-resonance probe with a 7.5 mm magic-angle spinning (MAS) probehead was used. ^{1}H and ^{13}C field strengths $\gamma B_1/2\pi$ of 62.5 kHz were used for all pulses. The MAS spinning speed was set to 6 kHz and the experiments were carried out at 23 °C. The ^{1}H spin-lattice relaxation times in the laboratory frame (T_{1H}) and those in the rotating frame ($T_{1\rho H}$) were measured employing the saturation recovery method and by applying a ^{1}H spin-locking pulse before the cross-polarization (CP) process of the standard CP/MAS pulse sequence, respectively, as described in Section 6.2.4. The T_{1H} and $T_{1\rho H}$ experiments reveal miscibility on the order of several tens of nanometers and on the order of several nanometers, respectively [15-17]. Typical thicknesses of OSCs in the thin films are about 100 nm. Diffusion lengths of excitons in OSCs are considered to be ~8.5 nm [19]. The length of the monomer unit of rrP3HT and the dimension of $PC_{61}BM$ are roughly 0.4 and 1.0 nm, respectively. T_{1H} and $T_{1\rho H}$ experiments are important to understand the performance of OSCs because the dimensions analyzed in these experiments are related to percolation path lengths toward the electrodes, exciton diffusion lengths, charge separations (charge transfer), and back electron transfer (recombination of holes and electrons).

6.2.4. Pulse sequences and analysis of T_{1H} and $T_{1\rho H}$ experiments

Pulse sequences used in this study for T_{1H} and $T_{1\rho H}$ experiments are shown in Fig. 6.2. The T_{1H} experiments were carried out employing the saturation recovery method, and the signal intensity $M(\tau)$ relaxes as a function of time τ, from zero to $M_\infty = M(\tau = \infty)$, according to

$$M(\tau) = M_\infty \left\{ 1 - \exp\left(-\frac{\tau}{T_{1H}} \right) \right\}. \tag{6.1}$$

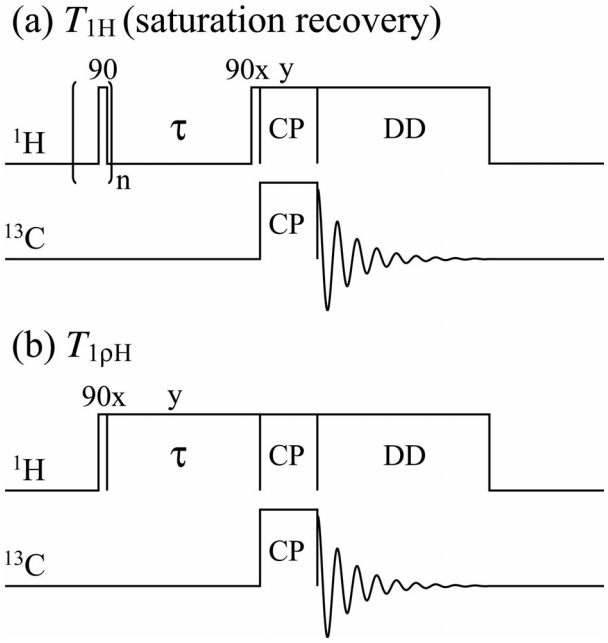

Fig. 6.2. Pulse sequences for (a) T_{1H} (saturation recovery) and (b) $T_{1\rho H}$ experiments.

This equation can be rewritten as

$$\log\left(1-\frac{M(\tau)}{M_\infty}\right)=-\frac{\tau}{T_{1H}}, \tag{6.2}$$

and the values of T_{1H} are obtained from plots of $\log\left(1-M(\tau)/M_\infty\right)$ versus τ.

In the $T_{1\rho H}$ experiments, the signal intensity $M(\tau)$ decays as a function of time τ, according to the following equation in the case of single exponential decays

$$M(\tau)=M_0\exp\left(-\frac{\tau}{T_{1\rho H}}\right), \tag{6.3}$$

where $M_0 = M(\tau = 0)$. The values of $T_{1\rho H}$ are obtained from the plots of $\log\left(M(\tau)/M_0\right)$ versus τ. However, in this study, the relaxation behavior for the $T_{1\rho H}$ experiments could not be explained by a single exponential decay, and introduction of the distribution of correlation times was necessary for the analysis. Therefore, we introduced the correlation time distribution using the Kohlrausch–Williams–Watts (KWW) function [20,21]:

$$\frac{M(\tau)}{M_0} = \exp\left\{-\left(\frac{\tau}{T_{1\rho H}}\right)^{\beta}\right\}, \tag{6.4}$$

where β represents the breadth of the distribution ($0 < \beta \leq 1$).

6.2.5. Estimation of domain sizes

Domain sizes, $\langle r \rangle$, estimated by a spin diffusion equation

$$\langle r \rangle = \sqrt{6DT_{1(\rho)H}}, \tag{6.5}$$

where D is the spin-diffusion coefficient, and $T_{1(\rho)H}$ is the relaxation times obtained by the T_{1H} and $T_{1\rho H}$ experiments.

6.2.6. Effect of molecular dynamics

T_{1H} and $T_{1\rho H}$ values are affected not only by miscibility but also by molecular dynamics. Therefore, we should also consider the effect of dynamics. To eliminate the effect of miscibility and consider the effect of dynamics solely, we calculated the average relaxation

behavior for rrP3HT and $PC_{61}BM$. The average of the $T_{1(\rho)H}$ values for rrP3HT and $PC_{61}BM$, $T_{1(\rho)H,\ average}$, was obtained with the equation:

$$\frac{1}{T_{1(\rho)H,\ average}} = \frac{N_{rrP3HT}}{N_{rrP3HT} + N_{PC_{61}BM}} \frac{1}{T_{1(\rho)H,\ rrP3AT}} + \frac{N_{PC_{61}BM}}{N_{rrP3HT} + N_{PC_{61}BM}} \frac{1}{T_{1(\rho)H,\ PC_{61}BM}}, \quad (6.6)$$

where N_{rrP3HT} is the number of protons in rrP3HT monomer, 14, N_{PC61BM} is the number of protons in $PC_{61}BM$, 14, $T_{1(\rho)H,\ rrP3HT}$ is the ^1H spin-lattice relaxation time of rrP3HT, and $T_{1(\rho)H,\ PC_{61}BM}$ is the ^1H spin-lattice relaxation time of $PC_{61}BM$. For the $T_{1\rho H}$ experiments, the values of β are also averaged.

6.3. Results and discussion

6.3.1. OSCs performance with different thermal annealing times

Figure 6.3 shows current density–voltage characteristics of the OSCs. Photoelectric conversion characteristics are also summarized in Table 6.1. Without annealing, the OSCs have a short-circuit current density (J_{sc}) of 2.42 mA/cm^2, an open-circuit voltage (V_{oc}) of 0.65 V, and a fill factor (FF) of 0.42, which results in PCE of 0.67 %. The OSC characteristics drastically increase with annealing for only 5 min; J_{sc} and FF increase to 8.59 mA/cm^2 and 0.58, respectively. Although V_{oc} decreases to 0.53 V, the PCE significantly increases to 2.65 %. Compared with the drastic increase, the PCE values were similar to those obtained with further annealing (2.87 % and 2.36 % with 15 min and 30 min annealing, respectively).

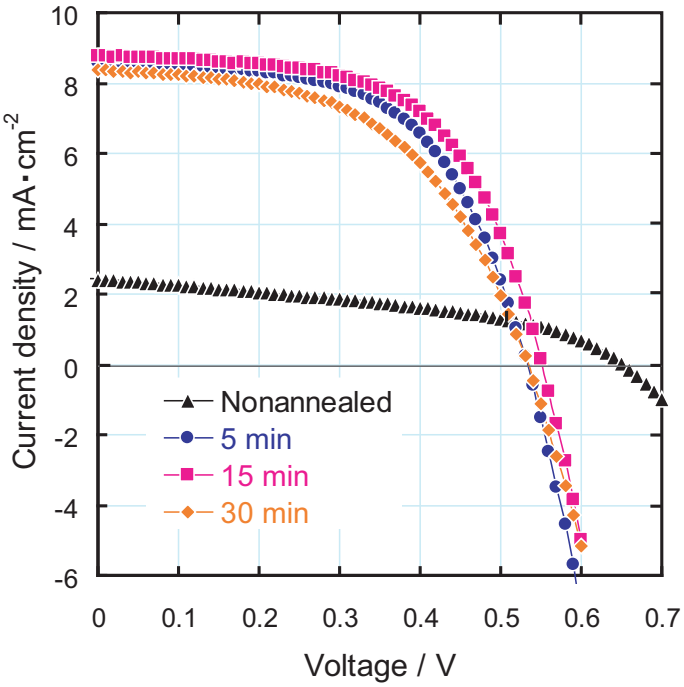

Fig. 6.3. Current density–voltage characteristics obtained from rrP3HT/$PC_{61}BM$ bulk heterojunction OSCs under AM 1.5 illumination at an irradiation intensity of 100 mW/cm^2. The annealing times are shown in the figure.

Table 6.1. Summary of photoelectric conversion characteristics for rrP3HT/$PC_{61}BM$.

Annealing time / min	J_{sc} / mA·cm^{-2}	V_{oc} / V	FF	PCE / %
0 (Nonannealed)	2.42	0.65	0.42	0.67
5	8.59	0.53	0.58	2.65
15	8.77	0.55	0.59	2.87
30	8.37	0.53	0.53	2.36

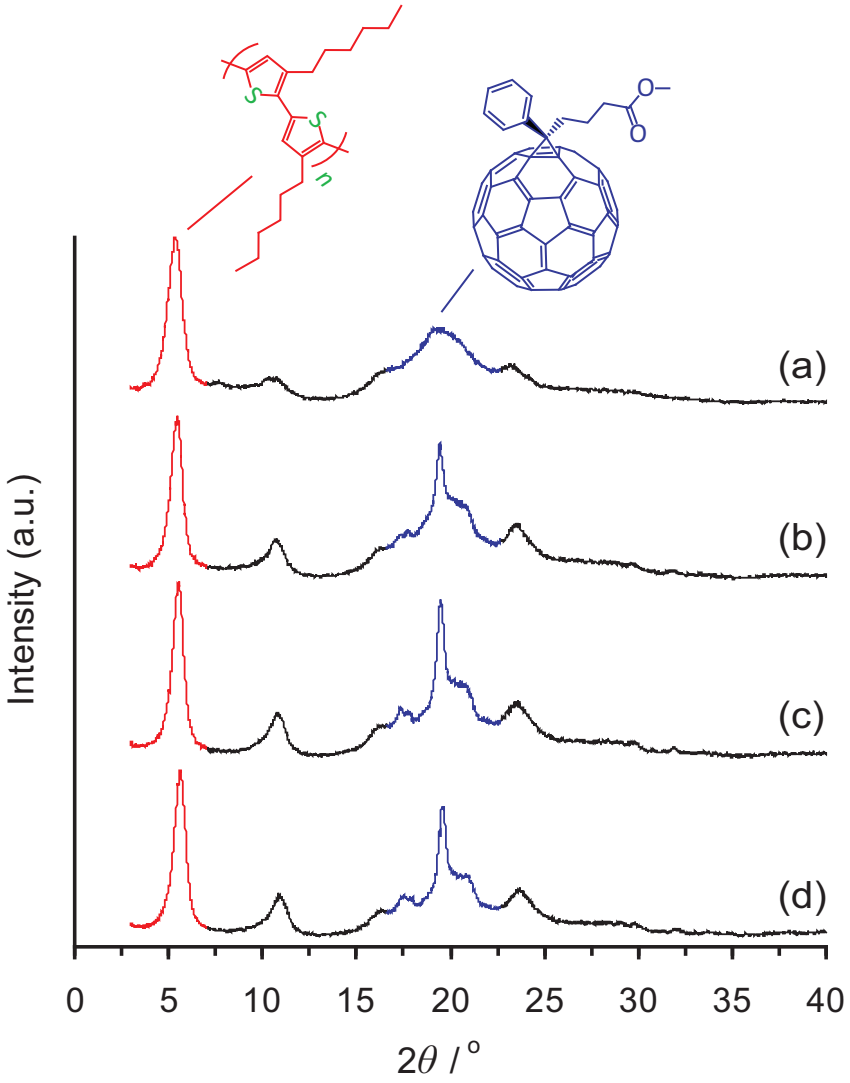

Fig. 6.4. WAXD profiles of rrP3HT/$PC_{61}BM$ blends: (a) nonannealed, annealing at 150 °C for (b) 5 min, (c) 15 min, and (d) 30 min.

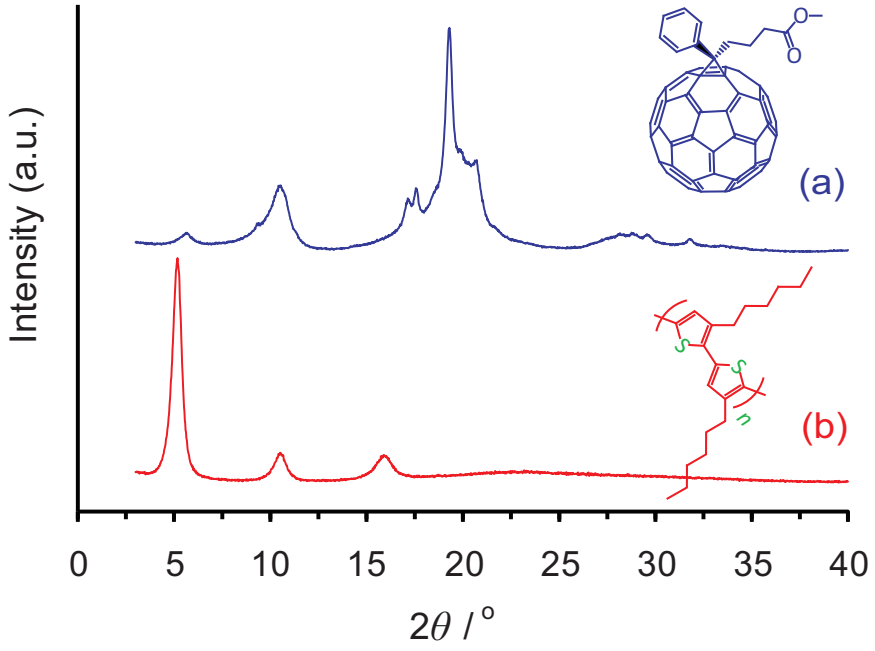

Fig. 6.5. WAXD profiles of (a) pure $PC_{61}BM$ and (b) pure rrP3HT annealed at 150 °C for 30 min.

6.3.2. Change of structural order in rrP3HT/$PC_{61}BM$ by thermal annealing

The origin of the effect of the thermal annealing was investigated in WAXD experiments. Figure 6.4 shows the experimental WAXD profiles of the nonannealed and annealed samples in rrP3HT/$PC_{61}BM$. A definite change is found at a diffraction angle of ~19°; the diffraction becomes significantly sharp with the first 5 min of annealing. The diffraction at ~19° purely originates from the $PC_{61}BM$, as shown in Fig. 6.5(a). Therefore, the obvious change in Fig. 6.4(a) and (b) is related to some structural order of $PC_{61}BM$ aggregates. Compared with the drastic change, the change for rrP3HT is small. The diffractions at ~6°, which originate from rrP3HT (Fig. 6.5(b)), become only slightly sharp with annealing (the half-widths are 1.01°, 0.83°, 0.78°, and 0.77° for the annealing times of 0, 5, 15, and 30 min, respectively).

6.3.3. Development of phase-separation by thermal annealing

Figure 6.6 shows the results of T_{1H} experiments for the nonannealed and annealed samples. For the nonannealed samples (Fig. 6.6(a)), the T_{1H} relaxation behaviors of rrP3HT and $PC_{61}BM$ agree with each other within experimental error; the T_{1H} values are 0.84 ± 0.01 s for both rrP3HT and $PC_{61}BM$. This indicates that rrP3HT and $PC_{61}BM$ are mixed with each other on the order of several tens of nanometers. The size range, $\langle r \rangle$, is calculated using the diffusion equation, the spin-diffusion coefficients (rrP3HT: 0.3 nm^2/ms, $PC_{61}BM$: 0.05 nm^2/ms) [13], and the T_{1H} values. The size is estimated to be 16–40 nm; the details are given in Table 6.2. The agreement of the T_{1H} values for rrP3HT and $PC_{61}BM$ indicates that the two constituents are homogeneously mixed within the 16–40 nm size range and no detectable domains larger than those are present in the nonannealed sample. The relaxation behaviors drastically change with isothermal annealing for only 5 min. As shown in Fig. 6.6(b), rrP3HT and $PC_{61}BM$ in the sample annealed at 150 °C for 5 min have significantly different T_{1H} relaxation behaviors.

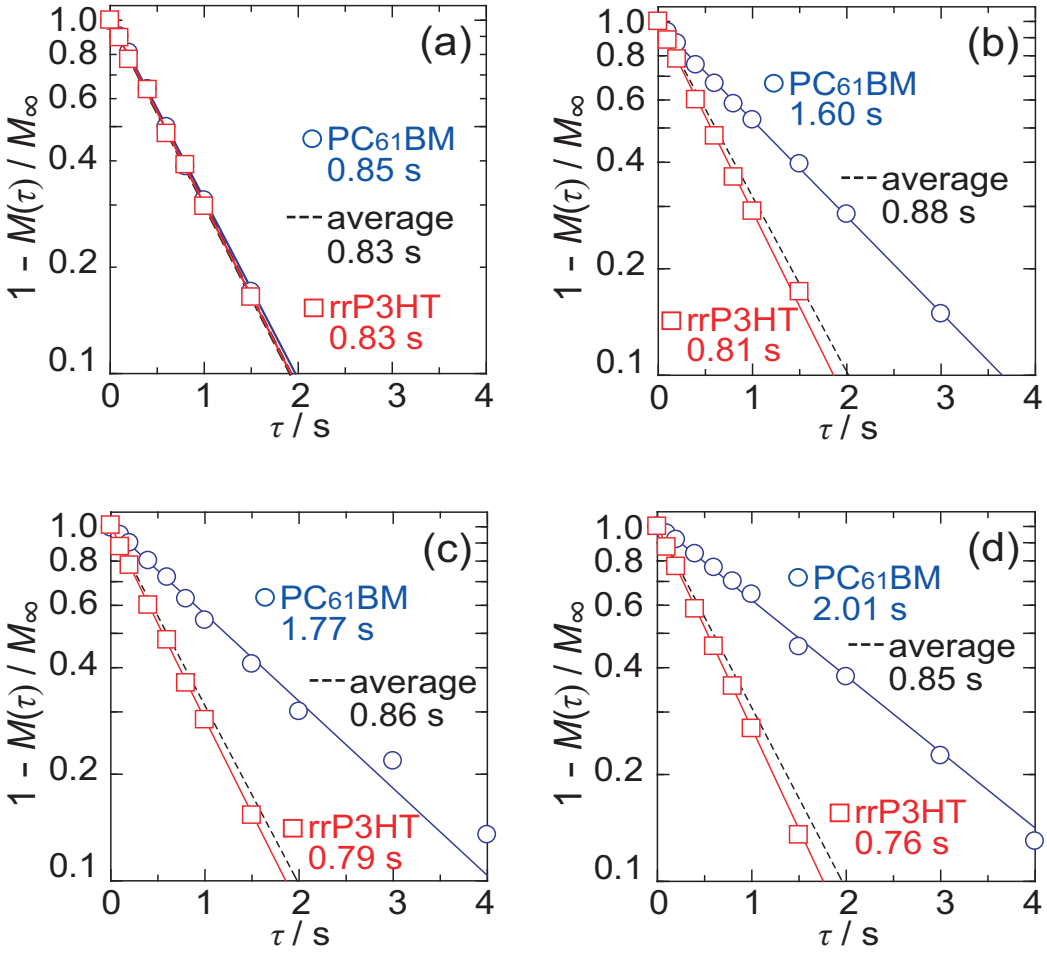

Fig. 6.6. T_{1H} relaxation curves of rrP3HT (open squares) and $PC_{61}BM$ (open circles) components in rrP3HT/$PC_{61}BM$ blends; (a) nonannealed, annealed at 150 °C for (b) 5 min, (c) 15 min, and (d) 30 min. The average relaxation curves for rrP3HT and $PC_{61}BM$ are calculated and shown as broken lines.

Table 6.2. Domain sizes observed in T_{1H} experiments.

Components	Domain sizes / nm			
	Nonannealed	Annealed at 150 °C		
		5 min	15 min	30 min
rrP3HT	39	38	38	37
$PC_{61}BM$	16	22	23	25

The T_{1H} values of rrP3HT and $PC_{61}BM$ are 0.81 and 1.60 s, respectively. This result clearly indicates that a phase-separated heterogeneous structure develops with annealing for only 5 min. The rrP3HT-rich and $PC_{61}BM$-rich domains larger than 16–40 nm form in the films. Further development of the phase separation is expected with annealing for 15 and 30 min (Fig. 6.6(c) and (d)). The T_{1H} values of rrP3HT (0.79 s and 0.76 s for 15 and 30 min of annealing) come close to that of pure rrP3HT (0.73 s for annealing at 150 °C for 30 min). Similarly, the T_{1H} values of $PC_{61}BM$ (1.77 s and 2.01 s for 15 and 30 min of annealing) come close to that of pure $PC_{61}BM$ (2.29 s for annealing at 150 °C for 30 min). However, the change from 5 to 30 min of annealing is small compared with that from 0 to 5 min. It is found that the structural change in this size range is closely related to the change in OSC performance shown in Fig. 6.3. The formation of rrP3HT-rich and $PC_{61}BM$-rich domains with 5 min annealing provides effective percolation paths for charge transport toward the electrodes. The phase separation is considered to contribute also to quenching the back electron transfer. These effects act as the improvement in cell performance, especially J_{sc}. Further phase separation would provide larger domains with decreased interfacial area, which may annihilate the excitons before they

reach the donor–acceptor interfaces and also prohibit the generation of free carriers. However, the PCE does not decrease significantly with annealing up to 30 min and the undesirable effects are not observed. Such effects, which decrease the PCE, would appear at longer annealing times and/or higher annealing temperatures. The average T_{1H} values are 0.83, 0.88, 0.86, and 0.85 s when annealing for 0, 5, 15, and 30 min, respectively, and no obvious change in the dynamics is found.

Figure 6.7 shows the results of $T_{1\rho H}$ experiments. In the experiments, the relaxation behavior cannot be explained by a single exponential decay, and a distribution of correlation times is required for the analysis by the KWW function, as described in Section 6.2.4. All the data in Fig. 6.7 were well reproduced by the KWW function with similar β values (0.8–0.9; the details are given in Table 6.3.). Different from the above T_{1H} experiments, rrP3HT and $PC_{61}BM$ in the nonannealed sample had different $T_{1\rho H}$ relaxation behaviors (Fig. 6.7(a)). This indicates that rrP3HT and $PC_{61}BM$ are phase separated even in the nonannealed samples on the order of several nanometers. The size range corresponding to the $T_{1\rho H}$ experiments was estimated to be 2–7 nm from the spin diffusion equation, spin-diffusion coefficients, and the above $T_{1\rho H}$ values (the details are given in Table 6.4.). Figure 6.7(b)–(d) shows the results of $T_{1\rho H}$ experiments for the annealed samples. Although the $T_{1\rho H}$ value of rrP3HT changes from 23 to 31 ms with the first annealing of 5 min, the relaxation behaviors essentially remain the same, irrespective of annealing up to 30 min. The $T_{1\rho H}$ values of the respective components in the blend samples are close to those of single-component samples annealed for 30 min (28 and 18 ms for pure rrP3HT and pure $PC_{61}BM$, respectively). This confirms that rrP3HT and $PC_{61}BM$ are phase separated on the 2–7 nm scale irrespective of the annealing condition. The average $T_{1\rho H}$ values are 21, 25, 27, and 26 ms for the 0, 5, 15, and 30 min annealed samples, respectively. Little dynamic change is observed for the averaged $T_{1\rho H}$ values, except for the

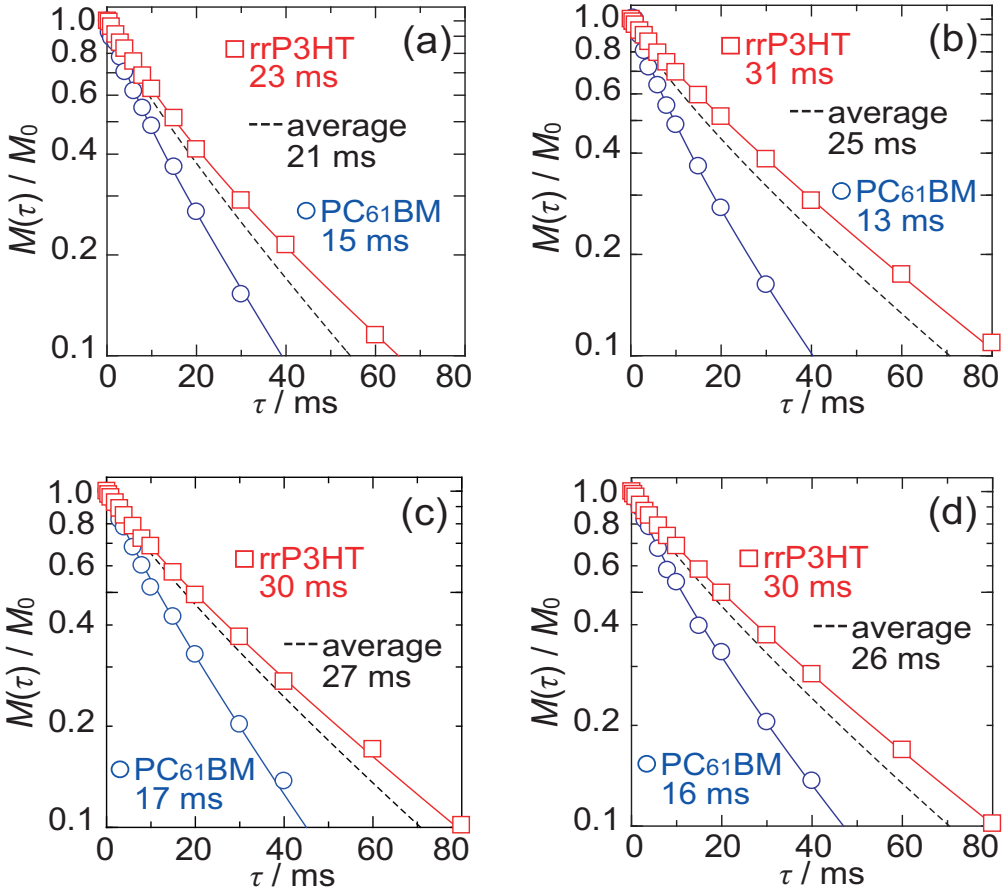

Fig. 6.7. $T_{1\rho H}$ relaxation curves of rrP3HT (open squares) and $PC_{61}BM$ (open circles) components in rrP3HT/$PC_{61}BM$ blends; (a) nonannealed, annealed at 150 °C for (b) 5 min, (c) 15 min, and (d) 30 min. The average relaxation curves for rrP3HT and $PC_{61}BM$ are calculated and shown as broken lines.

first 5 min of annealing. Only for the first 5 min of annealing is a slight increase in the averaged $T_{1\rho H}$ value found (from 21 to 25 ms). The origin is the change in dynamics of rrP3HT; $T_{1\rho H}$ for rrP3HT increases from 23 to 31 ms whereas that for $PC_{61}BM$ remains almost unchanged (from 15 to 13 ms), indicating that the molecular motion of rrP3HT is slightly restricted by the 5 min of annealing. The restricted molecular motion may also slightly contribute to the change in PCE.

.

Table 6.4. Domain sizes observed in $T_{1\rho H}$ experiments.

Components	Domain sizes / nm			
	Nonannealed	Annealed at 150 °C		
		5 min	15 min	30 min
rrP3HT	6.4	7.4	7.4	7.3
$PC_{61}BM$	2.1	2.0	2.3	2.2

Table 6.3. Values of β for the analysis of $T_{1\rho H}$ curves with the KWW function.

Components	β			
	Nonannealed	Annealed at 150 °C		
		5 min	15 min	30 min
rrP3HT	0.86	0.87	0.86	0.86
$PC_{61}BM$	0.85	0.77	0.86	0.79

6.4 Conclusions

In summary, we investigated the change in the donor–acceptor heterojunction structure of rrP3HT/$PC_{61}BM$ OSC systems during annealing mainly through solid-state NMR. The structures at different hierarchical levels, which are considered to be related to charge separation, back electron transfer, exciton diffusion, and charge transport, were analyzed in $T_{1\rho H}$ and T_{1H} experiments. The phase-separated structure analyzed in $T_{1\rho H}$ experiments does not significantly change with annealing. In contrast, it is clearly found in the T_{1H} experiments that a phase-separated heterojunction structure develops on the order of several tens of nanometers through thermal annealing of the rrP3HT/$PC_{61}BM$ systems. The structure change provides percolated carrier paths and can accelerate charge transport in OSCs. The phase-separated structure is also expected to prohibit back electron transfer. This results in the improvement of the J_{SC} and hence the PCE.

Acknowledgments

This study was conducted using the solid-state NMR spectrometer in the Joint Usage/Research Center (JURC) at the Institute for Chemical Research, Kyoto University.

References

[1] F. Padinger, R.S. Rittberger, N.S. Sariciftci, Adv. Funct. Mater., 13 (2003) 85.

[2] W.L. Ma, C.Y. Yang, X. Gong, K. Lee, A.J. Heeger, Adv. Funct. Mater., 15 (2005) 1617.

[3] M. Al-Ibrahim, O. Ambacher, S. Sensfuss, G. Gobsch, Appl. Phys. Lett., 86 (2005) 201120.

[4] M. Reyes-Reyes, K. Kim, D.L. Carroll, Appl. Phys. Lett., 87 (2005) 083506.

[5] Y. Kim, S. Cook, S.M. Tuladhar, S.A. Choulis, J. Nelson, J.R. Durrant, D.D.C. Bradley, M. Giles, I. Mcculloch, C.S. Ha, M. Ree, Nat. Mater., 5 (2006) 197.

[6] M. Campoy-Quiles, T. Ferenczi, T. Agostinelli, P.G. Etchegoin, Y. Kim, T.D. Anthopoulos, P.N. Stavrinou, D.D.C. Bradley, J. Nelson, Nat. Mater., 7 (2008) 158.

[7] K. Schmidt-Rohr, H.W. Spiess, Multidimensional Solid-State NMR and Polymers, Academic Press, London, 1994.

[8] H. Kaji, Y. Kusaka, G. Onoyama, F. Horii, Jpn. J. Appl. Phys., 44 (2005) 3706.

[9] H. Kaji, Y. Kusaka, G. Onoyama, F. Horii, J. Am. Chem. Soc., 128 (2006) 4292.

[10] Y. Nishiyama, T. Fukushima, K. Takami, Y. Kusaka, T. Yamazaki, H. Kaji, Chem. Phys. Lett., 471 (2009) 80.

[11] C.Y. Yang, J.G. Hu, A.J. Heeger, J. Am. Chem. Soc., 128 (2006) 12007.

[12] R. Mens, P. Adriaensens, L. Lutsen, A. Swinnen, S. Bertho, B. Ruttens, J. D'Haen, J. Manca, T. Cleij, D. Vanderzande, J. Gelan, J. Polym. Sci. A: Polym. Chem., 46 (2008) 138.

[13] R.C. Nieuwendaal, C.R. Snyder, R.J. Kline, E.K. Lin, D.L. VanderHart, D.M. DeLongchamp, Chem. Mater., 22 (2010) 2930.

[14] H. Kaji, H. Hayashi, T. Yamada, M. Fukuchi, S. Fujimura, M. Ueda, S. Kang, T. Umeyama, Y. Matano, H. Imahori, Appl. Phys. Lett., 98 (2011) 113301.

[15] V.J. McBrierty, D.C. Douglass, T.K. Kwei, Macromolecules, 11 (1978) 1265.

[16] X. Zhang, K. Takegoshi, K. Hikichi, Polym. J., 23 (1991) 87.

[17] X. Zhang, K. Takegoshi, K. Hikichi, Macromolecules, 24 (1991) 5756.

[18] A. Asano, K. Takegoshi, K. Hikichi, Polym. J., 24 (1992) 555.

[19] P.E. Shaw, A. Ruseckas, I.D.W. Samuel, Adv. Mater., 20 (2008) 3516.

[20] G. Williams, D.C. Watts, Trans. Faraday Soc., 66 (1970).

[21] G. Williams, D.C. Watts, S.B. Dev, A.M. North, Trans. Faraday Soc., 67 (1971) 1323.

Chapter 7

Solid-State NMR Analysis of Donor/Acceptor Bulk Heterojunction Structures in Organic Solar Cells: Importance of Side Chain Lengths in Donor Polymers

7.1. Introduction

Organic solar cells (OSCs) could potentially reduce the dependence on the fossil fuel. Among them, polymer bulk-heterojunction OSCs (polymer BHJ solar cells), which consist of donor polymers and acceptors, have attracted attention as a low-cost energy source because of easy fabrications of wet processes [1-14]. In donor polymers, alkyl side-chain substituents are certainly attached in main chain to improve the solubility in organic solvents [15-18]. Longer alkyl side-chains lead to the higher solubility, and probably affect the carrier mobility. Extensive research has been carried out on polymer BHJ solar cells to improve power conversion efficiencies (PCEs). Among the conclusions, the thermal annealing treatment is easy and inexpensive way to improve the PCE [19-25]. The effects of alkyl side chain and the thermal annealing treatment on PCE are important topics in polymer BHJ solar cells. OSCs work via sun-light absorption, generation of excitons, diffusion of excitons, charge separation between donor and acceptor interfaces, charge transport toward electrodes, and pass through an external circuit. The photoelectric conversion process occurs at different size scales. Therefore, it is essential for understanding the above effects on polymer BHJ solar cells to investigate the donor-acceptor structures.

In this chapter, the effect of alkyl side-chain lengths of the donor polymers on the photoelectric conversion characteristics and on the BHJ structures during isothermal annealing was investigated by same analyses in chapter 6. As the donor polymers, three types of

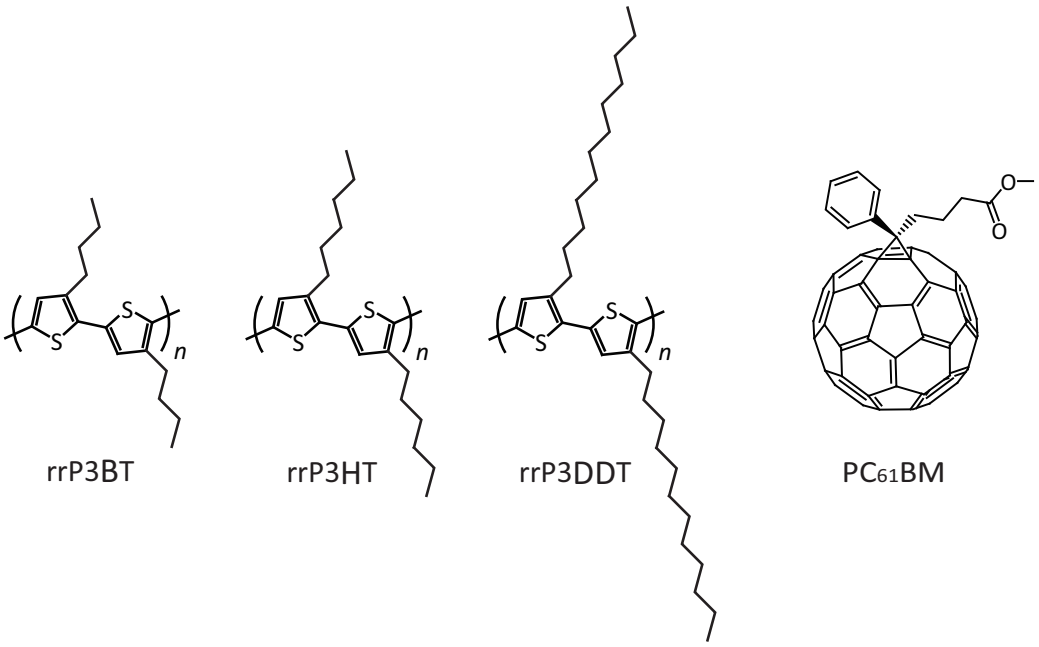

Fig. 7.1. Chemical structures of the materials used in this study.

regioregular poly(3-alkylthiophene-2,5-diyl) (rrP3AT) with different alkyl side-chain lengths were used; regioregular poly(3-butylthiophene-2,5-diyl) (rrP3BT), poly(3-hexylthiophene-2,5-diyl) (rrP3HT), and poly(3-dodecylthiophene-2,5-diyl) (rrP3DDT). $PC_{61}BM$ was used as acceptor. The materials are shown in Fig. 7.1. From this study, it is found that the alkyl side-chains significantly affect the donor-acceptor phase-separated structures, which result in the change of photoelectric conversion characteristics.

7.2. Experimental procedures

7.2.1. Fabrication of polymer BHJ solar cells

Regioregular (rr) P3BT, rrP3HT, and rrP3DDT were purchased from Aldrich Chemical Co. $PC_{61}BM$ was also purchased from Frontier Carbon Co. Poly(3,4-ethylene dioxythiophene):poly(styrenesulfonate) (PEDOT:PSS) (CLEVIOS™ P VP AI 4083, HC Starck) was spin-coated with 40 nm thickness from aqueous solution on indium–tin–oxide (ITO) substrates. The thickness of the ITO was 150 nm. ITO substrate with spin-coated PEDOT:PSS were dried at 110 °C for 30 min in vacuum and were used for all the devices in this study. An active layer consisting of rrP3AT and $PC_{61}BM$ at a weight ratio of 1:1, was spin-coated with the thickness of 110 nm on the PEDOT:PSS layer using chloroform as a solvent. For annealed samples, the ITO substrates with the PEDOT:PSS and the active layer were isothermally annealed at 150 °C for designated times in vacuum. Subsequently, a 0.6 nm of lithium fluoride (LiF, 4N grade, Kojundo Chemical Lab. Co., Ltd.) and a 100 nm thick aluminium (Al, 5N grade, Kojundo Chemical Lab. Co., Ltd.) electrode were deposited onto the active layer of all the devices in this study by vacuum evaporation at $< 4.0\times10^{-5}$ Pa. The current density–voltage (*J–V*) characteristics of the polymer BHJ solar cells were measured

using a solar simulator (OTENTOSUN II, BUNKOUKEIKI Co. Ltd.) under 100 mW/cm^2 white-light illumination (air mass 1.5G illumination).

7.2.2. Structural analyses

Samples for wide-angle X-ray diffraction (WAXD) and solid-state NMR experiments were prepared by drop casting of rrP3AT/$PC_{61}BM$ mixed solution with 1:1 wt% on a glass substrate using chloroform as a solvent. Here, the as-casted sample is referred to as the nonannealed sample. Annealed samples were isothermally annealed at 150 ^{o}C at designated times in vacuum. Pure rrP3BT, pure rrP3HT, pure rrP3DDT, and pure $PC_{61}BM$ samples were also prepared by the same procedure. WAXD data were recorded at room temperature on a Rigaku RINT 2000 diffractometer using Cu-K_α radiation and operating at 300 mA and 40 kV. Solid-state NMR measurements were conducted on a Bruker AVANCEIII 400 MHz spectrometer operating under a static magnetic field of 9.4 T. A double-resonance probe with a 4.0 mm magic-angle spinning (MAS) stator was used. The above samples were scrapped off using a sharp blade and were packed into zirconia rotors. ^{1}H and ^{13}C radiofrequency (rf) field strengths $\gamma B_1/2\pi$ of 80 kHz were used for all pulses. The MAS spinning speed was set to 15 kHz and the experiments were carried out at 300 K. The ^{1}H spin-lattice relaxation times in the rotating frame ($T_{1\rho H}$) were measured by applying a ^{1}H spin-locking pulse before the cross-polarization (CP) process of the standard CP/MAS pulse sequence. The ^{1}H spin-lattice relaxation times in the laboratory frame (T_{1H}) were measured employing the saturation recovery method. The pulse sequences for the $T_{1\rho H}$ and T_{1H} experiments are shown in Section 6.2.4.

7.2.3. Optical and electrochemical measurements

Samples for optical and electrochemical measurements were prepared by spin-coating on

fused quartz substrates. Annealed samples were isothermally annealed at 150 °C at designated times in vacuum. UV-vis absorption spectra were measured using a Shimazu UV-3600. Optical band gaps (E_g) were estimated from the lowest-energy absorption edge of the UV-vis absorption spectra of pure rrP3ATs and pure $PC_{61}BM$. Ionization potentials were determined by an atmospheric ultraviolet photoelectron spectroscopy (AC-3, RIKEN KEIKI Co., Ltd.) for pure rrP3ATs and pure $PC_{61}BM$.

7.2.4. Estimation of hole mobility by space-charge-limited current measurement

Hole mobilities of rrP3BT, rrP3HT, and rrP3DDT were estimated in a space-charge-limited current regime at *J-V* characteristics. Hole only devices were composed of ITO 150 nm / PEDOT:PSS 20 nm / rrP3ATs (rrP3BT, rrP3HT, and rrP3DDT) / Al 100 nm. The thickness of rrP3AT layer was 0.24, 0.37, and 0.32 μm for rrP3BT, rrP3HT, and rrP3DDT, respectively. PEDOT:PSS layer was spin-coated on ITO substrate as a hole-injection and electron-blocking layer. rrP3ATs layer were spin-coated on the PEDOT:PSS layer using chloroform as a solvent. The ITO substrates with the PEDOT:PSS and rrP3AT were isothermally annealed at 150 °C for 30 min in vacuum. Subsequently, 100 nm of Al was deposited on the rrP3AT layer by vacuum evaporation at a pressure of 10^{-5} Pa. *J–V* characteristics of the HODs were measured with a source measure unit (Keithley 2400). Personal-computer based software for device characterization was kindly provided by Keithley Instruments K. K. Japan.

7.3. Results and Discussion

7.3.1. Photoelectric conversion characteristics of rrP3AT/$PC_{61}BM$ systems

Fig. 7.2 show current density–voltage characteristics of the polymer BHJ solar cells for

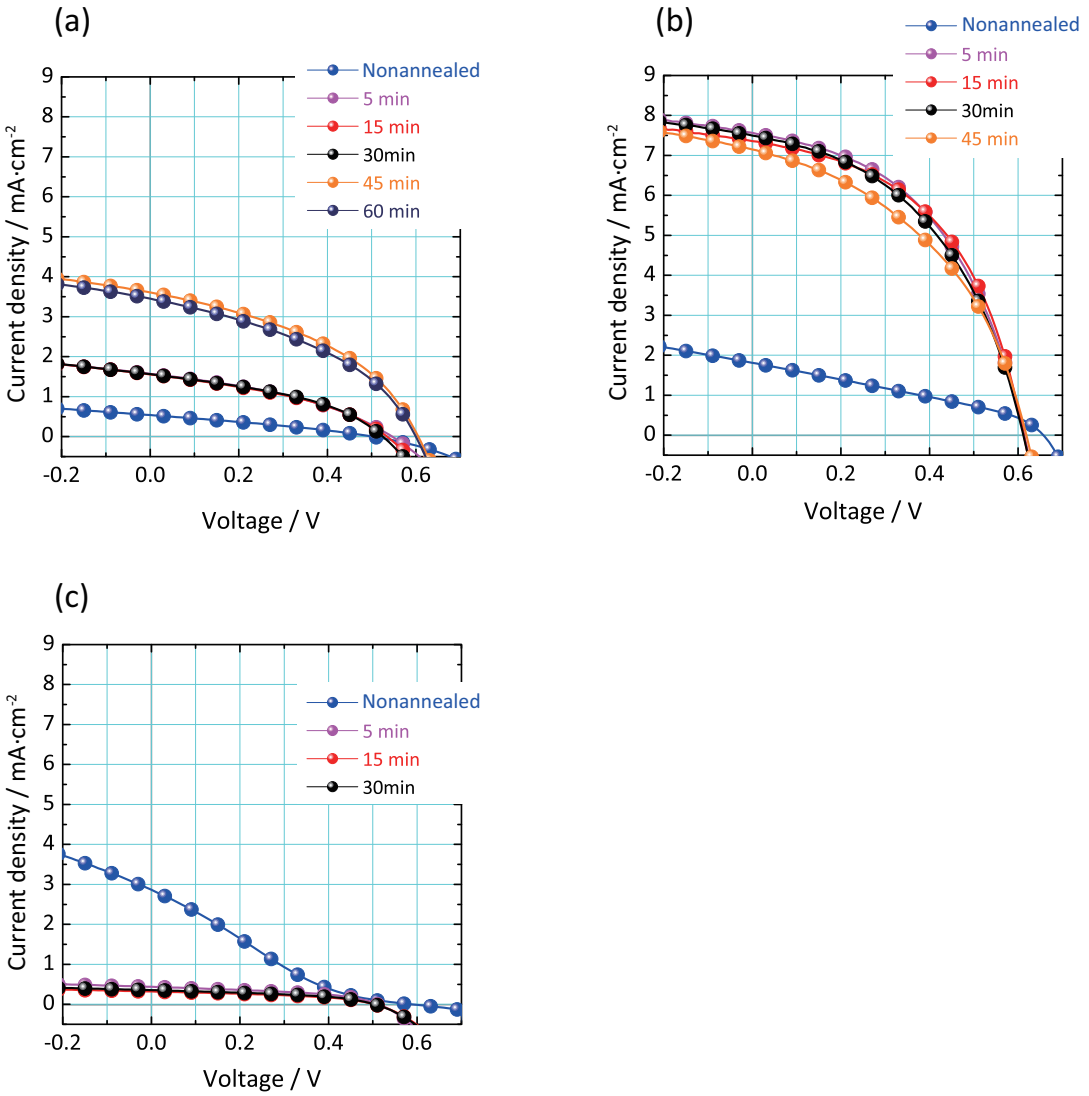

Fig. 7.2. Current density–voltage characteristics of polymer BHJ solar cells obtained from (a) rrP3BT/$PC_{61}BM$, (b) rrP3HT/$PC_{61}BM$, and (c) rrP3DDT/$PC_{61}BM$ mixtures under AM 1.5G illumination at an irradiation intensity of 100 mW/cm^2. The annealing times are shown in the figure.

Table 7.1. Summary of photoelectric conversion characteristics for rrP3AT/$PC_{61}BM$ systems.

rrP3ATs	Annealing time / min	J_{sc} / mA·cm^{-2}	V_{oc} / V	FF	PCE / %
rrP3BT	0 (Nonannealed)	0.54	0.50	0.30	0.08
	5	1.57	0.55	0.38	0.32
	15	1.56	0.53	0.39	0.32
	30	1.56	0.53	0.40	0.33
	45	3.61	0.61	0.42	0.91
	60	3.45	0.6	0.40	0.83
rrP3HT	0 (Nonannealed)	1.81	0.66	0.32	0.38
	5	7.57	0.61	0.47	2.18
	15	7.36	0.61	0.49	2.21
	30	7.49	0.61	0.46	2.09
	45	7.15	0.62	0.43	1.91
rrP3DDT	0 (Nonannealed)	2.86	0.58	0.20	0.33
	5	0.43	0.51	0.44	0.10
	15	0.32	0.50	0.44	0.07
	30	0.36	0.50	0.44	0.08

rrP3BT/$PC_{61}BM$, rrP3HT/$PC_{61}BM$, and rrP3DDT/$PC_{61}BM$ systems under AM 1.5G illumination at an irradiation intensity of 100 mW/cm^2. The performances of polymer BHJ solar cells are summarized in Table 7.1. For rrP3BT/$PC_{61}BM$ system, polymer BHJ solar cells without annealing have a short-circuit current density (J_{SC}) of 0.54 mA/cm^2, an open-circuit voltage (V_{OC}) of 0.50 V, and a fill factor (FF) of 0.30, which results in PCE of 0.08 %. By annealing for 5 min, the PCE increases to 0.32 % mainly due to the increase of J_{SC} of 1.57 mA/cm^2. The PCE values remain almost the same with annealing up to 30 min (0.32 % and 0.33 % with 15 min and 30 min annealing, respectively). Interestingly, the PCE value further increases to 0.91 % by prolonged annealing of 45 min. For rrP3HT/$PC_{61}BM$ system (Fig. 7.2(b)), the characteristics of nonannealed device show J_{SC} of 1.81 mA/cm^2, V_{OC} of 0.66 V, and the FF of 0.32, which results in PCE of 0.38 %. By annealing for 5 min, the photoelectric conversion characteristics drastically change; J_{SC} of 7.57 mA/cm^2, V_{OC} of 0.61 V, and the FF of 0.47. Although the V_{OC} decreases to 0.61, the PCE increases from 0.38 to 2.18 % by the 5 min of annealing. Polymer BHJ solar cells with annealing for 15 min show the highest PCE of 2.21 %. The PCEs are found to decrease by further annealing; the PCE values with annealing for 30 min and 45 min are 2.09 % and 1.91 %, respectively. Different from the above two systems, the increase of the PCE values is not observed for rrP3DDT/$PC_{61}BM$ system (Fig. 7.2 (c)). The PCE of 0.33 % for the nonannealed solar cell nearly the same and larger compared to these for rrP3HT/$PC_{61}BM$ and rrP3BT/$PC_{61}BM$ systems (0.38 and 0.08 %). However, the PCE value decreases for 0.38 to 0.10 % by 5min of annealing and remains low by further annealing. As shown above the difference of alkyl side-chains alters the performance of polymer BHJ solar cells, although the polymer main chains of donor and acceptors in these systems are the same. To reveal the origin of the drastic effect of side-chains, solid-state NMR experiments as well as WAXD, UV-vis absorption, carrier mobility measurements were carried out.

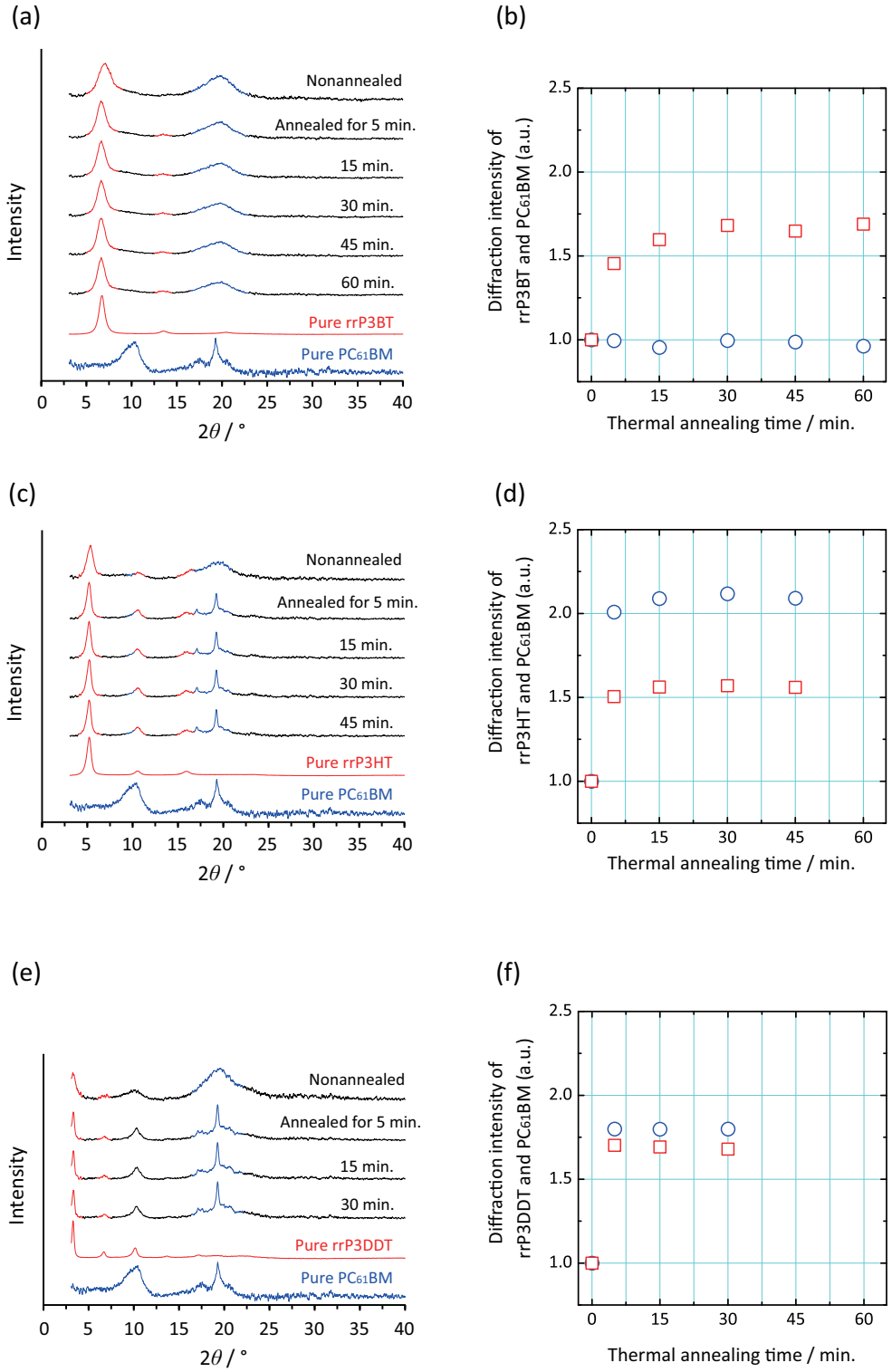

Fig. 7.3. WAXD profiles and change of diffraction intensities in rrP3BT/$PC_{61}BM$ (a, b), rrP3HT/$PC_{61}BM$ (c, d), and rrP3DDT/$PC_{61}BM$ films (e, f) as a function of thermal annealing time; open squares: rrP3AT, open circles: $PC_{61}BM$.

7.3.2. Development of structural order by thermal annealing

Figure 7.3 shows the experimental WAXD profiles of nonannealed and annealed rrP3AT/$PC_{61}BM$ blend samples. The experimental WAXD profiles for pure rrP3ATs and pure $PC_{61}BM$ annealed at 150 °C for 60 min were also shown for comparison. For rrP3BT/$PC_{61}BM$ system (Fig. 7.3 (a)), the diffractions at ~ 7° and ~19° originate from the rrP3BT and the $PC_{61}BM$, respectively. By annealing for 5 min, the diffractions of rrP3BT become narrower; the half-widths are change from 1.84° to 1.22°. Annealing time dependences of diffraction intensities for rrP3BT and $PC_{61}BM$ are shown in Fig. 7.3 (b). The intensity of rrP3BT increases 1.5 times by 5 min of annealing and becomes almost plateau by further annealing. The result indicates that some ordering of rrP3BT occurs in the blend films with 5 min of annealing. In contrast, the diffractions of $PC_{61}BM$ are almost unchanged irrespective of annealing times. Structure orderings of rrP3HT/$PC_{61}BM$ and rrP3DDT/$PC_{61}BM$ systems are different from that of rrP3BT/$PC_{61}BM$ system. As shown in Figs. 7.3 (c) and (d), the diffraction at ~ 5° originate from the rrP3HT becomes narrower and stronger; the half-width and the diffraction intensity are change from 0.84° to 0.56° and increase 1.5 times by 5 min of annealing, respectively. The diffraction of $PC_{61}BM$ drastically changes. The diffraction profile and intensity becomes significantly sharp and increase 2 times by annealing only for 5 min, respectively. For rrP3DDT/$PC_{61}BM$ system (Figs. 7.3 (e) and (f)), the half-width and the diffraction intensity of rrP3DDT at ~ 3° are change from 0.52° to 0.40° and increase 1.7 times by 5 min of annealing, respectively. The intensity of $PC_{61}BM$ becomes increase 1.8 times by annealing. From WAXD experiments, it is found that structure ordering of $PC_{61}BM$ in rrP3BT/$PC_{61}BM$ system does not develop irrespective of annealing times, although ordering of rrP3BT occurs by annealing only for 5 min. Different from the rrP3BT/$PC_{61}BM$ system, structure ordering occurs by 5 min of annealing for both of rrP3HT/$PC_{61}BM$ and

rrP3DDT/$PC_{61}BM$ systems.

7.3.3. Phase-separation behaviors during thermal annealing

Figure 7.4 shows the results of $T_{1\rho H}$ experiments for the nonannealed and annealed samples in rrP3BT/$PC_{61}BM$ system. It is found that rrP3BT and $PC_{61}BM$ have different $T_{1\rho H}$ relaxation behaviors irrespective of annealing times. This result indicated that rrP3BT and $PC_{61}BM$ are phase-separated on the order of several nanometers for all samples. Figures 7.5 and 7.6 show the results $T_{1\rho H}$ experiments of rrP3HT/$PC_{61}BM$ and rrP3DDT/$PC_{61}BM$ systems, respectively. Similar to the case of the rrP3BT/$PC_{61}BM$ system, rrP3HT/$PC_{61}BM$ and rrP3DDT/$PC_{61}BM$ systems are phase-separated irrespective of annealing times. The domain sizes analyzed in $T_{1\rho H}$ experiments can be estimated to be 2–8 nm by the same method in chapter 6, and the details are summarized in Table 7.2.

Figure 7.7 shows the results of T_{1H} experiments for rrP3BT/$PC_{61}BM$ samples. For the nonannealed sample (Fig. 7.7(a)), the T_{1H} relaxation of rrP3BT and $PC_{61}BM$ whose T_{1H} values are 1.03 s and 1.04 s, respectively, agree with each other unlike the results of $T_{1\rho H}$ experiments. The domain sizes analyzed in T_{1H} experiments can be estimated to be 20–40 nm, and the details are summarized in Table 7.3. The above results indicate that rrP3BT and $PC_{61}BM$ are homogeneously mixed in the 20–40 nm size range and no detectable domains larger than those are present in the nonannealed sample. The T_{1H} relaxation behaviors remain the same until 30 min of annealing (Fig. 7.7 (b)–(d)). For 45 min of annealing, the relaxation behaviors change. As shown in Fig. 7.7 (e), rrP3BT and $PC_{61}BM$ in the sample annealed for 45 min show different T_{1H} values, 1.03 and 1.18 s, respectively. This result indicates that a phase-separation start by annealing for 45 min. By 60 min of annealing, the phase-separated structure develops.

Figure 7.8 shows the results of T_{1H} experiments for nonannealed and annealed

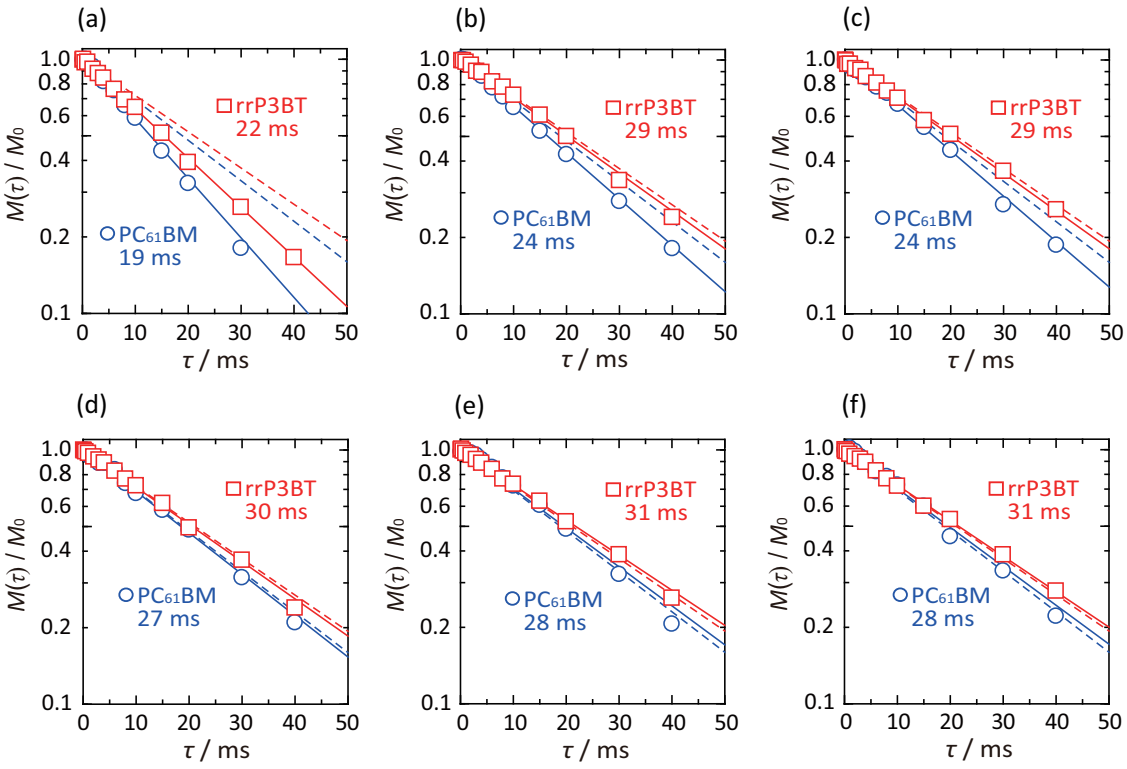

Fig. 7.4. $T_{1\rho H}$ relaxation behaviors of rrP3BT (open squares) and $PC_{61}BM$ (open circles) components in rrP3BT/$PC_{61}BM$ systems; (a) nonannealed, annealed at 150 °C for (b) 5 min, (c) 15 min, (d) 30 min, (e) 45 min, and (f) 60 min. $T_{1\rho H}$ values are written in each figures. $T_{1\rho H}$ relaxation behaviors of pure rrP3BT and pure $PC_{61}BM$ are also shown as broken lines for reference.

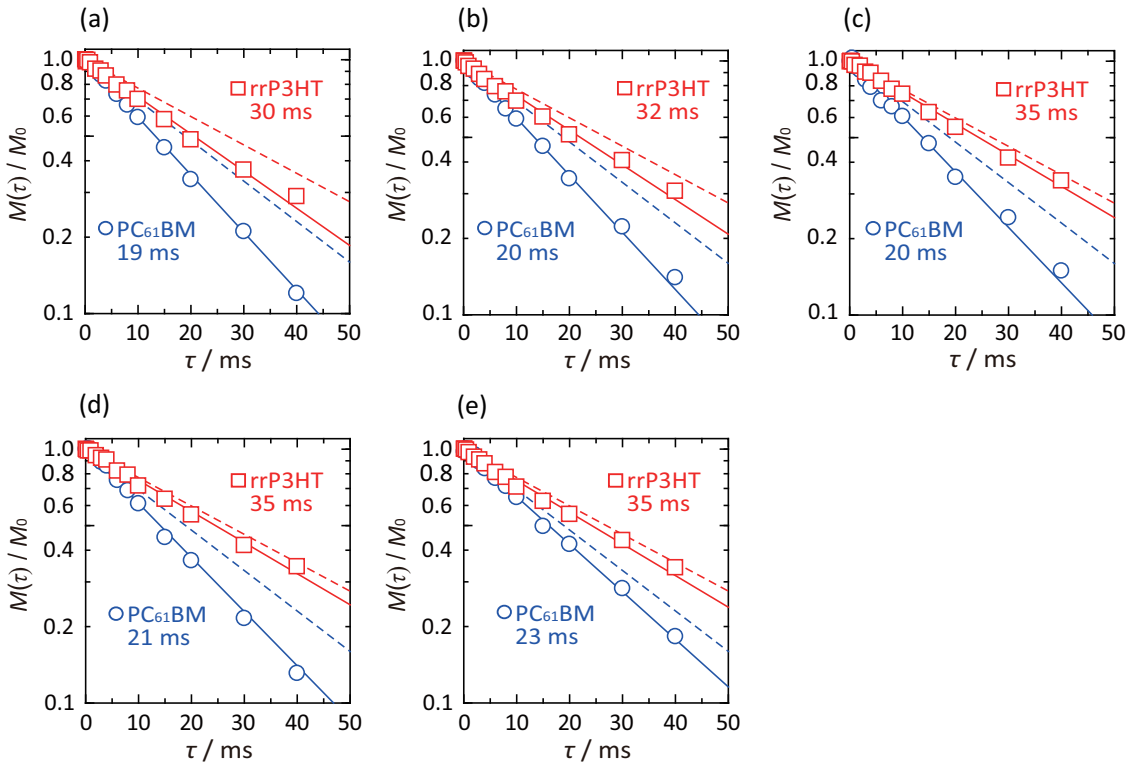

Fig. 7.5. $T_{1\rho H}$ relaxation behaviors of rrP3HT (open squares) and $PC_{61}BM$ (open circles) components in rrP3HT/$PC_{61}BM$ systems; (a) nonannealed, annealed at 150 °C for (b) 5 min, (c) 15 min, (d) 30 min, and (e) 45 min. $T_{1\rho H}$ values are written in each figures. $T_{1\rho H}$ relaxation behaviors of pure rrP3HT and pure $PC_{61}BM$ are also shown as broken lines for reference.

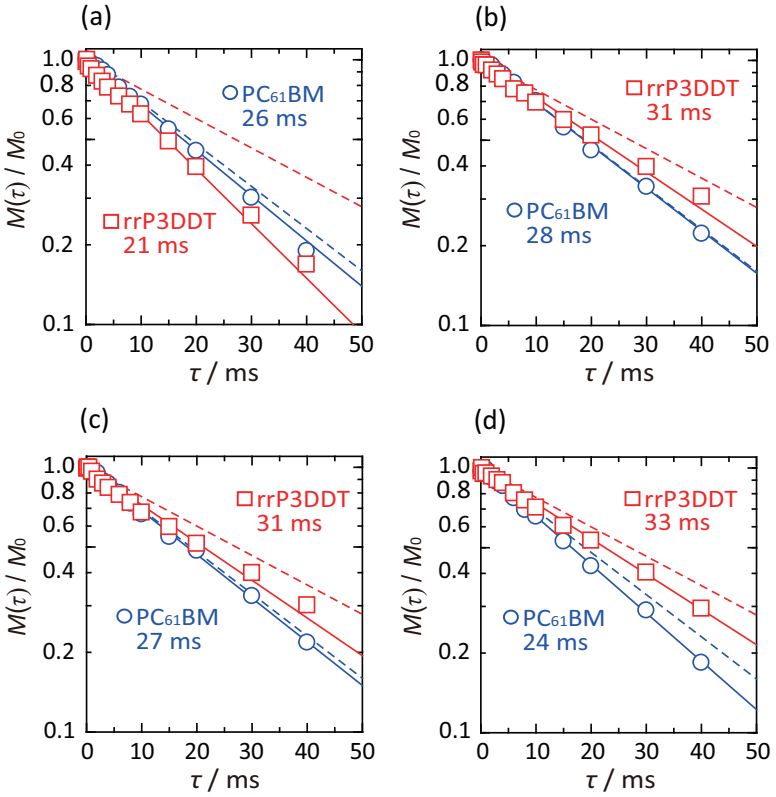

Fig. 7.6. $T_{1\rho H}$ relaxation behaviors of rrP3DDT (open squares) and $PC_{61}BM$ (open circles) components in rrP3DDT/$PC_{61}BM$ systems; (a) nonannealed, annealed at 150 °C for (b) 5 min, (c) 15 min, and (d) 30 min. $T_{1\rho H}$ values are written in each figures. $T_{1\rho H}$ relaxation behaviors of pure rrP3DDT and pure $PC_{61}BM$ are also shown as broken lines for reference.

Table 7.2. Domain sizes observed in $T_{1\rho H}$ experiments.

	Domain size / nm					
	rrP3BT/$PC_{61}BM$		rrP3HT/$PC_{61}BM$		rrP3DDT/$PC_{61}BM$	
Annealed at 150 °C	rrP3BT	$PC_{61}BM$	rrP3HT	$PC_{61}BM$	rrP3DDT	$PC_{61}BM$
0 min (Nonannealed)	6.3	2.4	7.4	2.4	6.2	2.8
5 min	7.2	2.7	7.6	2.5	7.5	2.9
15 min	7.2	2.7	7.9	2.5	7.5	2.9
30 min	7.4	2.9	7.9	2.5	7.7	2.7
45 min	7.5	2.9	7.9	2.6		
60 min	7.5	2.9				

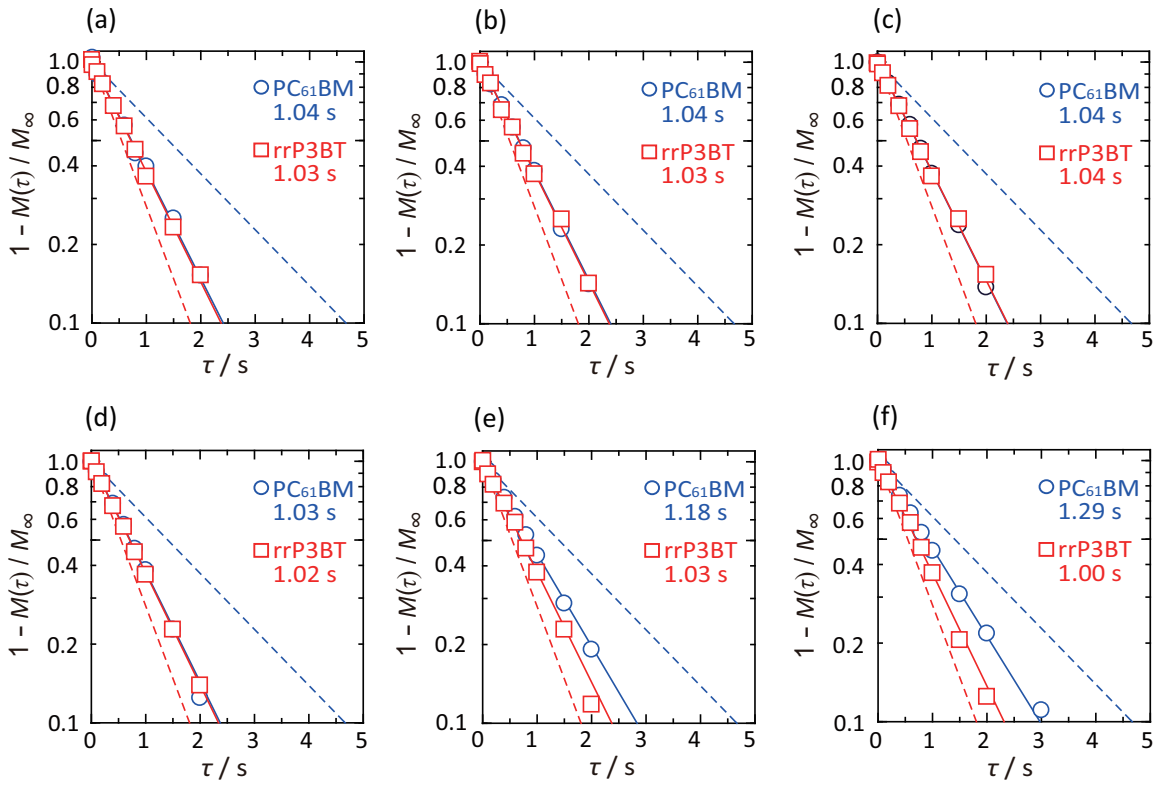

Fig. 7.7. T_{1H} relaxation behaviors of rrP3BT (open squares) and $PC_{61}BM$ (open circles) components in rrP3BT/$PC_{61}BM$ blends; (a) nonannealed, annealed at 150 °C for (b) 5 min, (c) 15 min, (d) 30 min, (e) 45 min, and (f) 60 min. T_{1H} values are written in each figures. T_{1H} relaxation behaviors of pure rrP3BT and pure $PC_{61}BM$ with annealed 150°C for 60 min are also shown as broken lines for references.

Table 7.3. Domain sizes observed in T_{1H} experiments.

	Domain size / nm					
	rrP3BT/$PC_{61}BM$		rrP3HT/$PC_{61}BM$		rrP3DDT/$PC_{61}BM$	
Annealed at 150 °C	rrP3BT	$PC_{61}BM$	rrP3HT	$PC_{61}BM$	rrP3DDT	$PC_{61}BM$
0 min (Nonannealed)	43	18	40	17	40	21
5 min	43	18	40	18	39	23
15 min	43	18	39	19	39	24
30 min	43	18	39	20	38	25
45 min	43	19	39	24		
60 min	42	19				

rrP3HT/$PC_{61}BM$ samples. For the nonannealed sample (Fig. 7.8(a)), the T_{1H} relaxation behaviors of rrP3HT and $PC_{61}BM$ agree with each other; the T_{1H} values of rrP3HT and $PC_{61}BM$ are 0.91 s and 0.93 s, respectively. The domain sizes of rrP3HT/$PC_{61}BM$ are estimated to be 20–40 nm, as shown in Table 7.3. The result in Fig. 7.8 (a) indicates that rrP3HT and $PC_{61}BM$ are homogeneously mixed within the 20–40 nm size range. Different from the above rrP3BT/$PC_{61}BM$ system, the relaxation behaviors change with annealing for only 5 min for the rrP3HT/$PC_{61}BM$ system, as shown in Fig. 7.8 (b); the rrP3HT and $PC_{61}BM$ in the sample annealed for 5 min have different T_{1H} values of rrP3HT and $PC_{61}BM$, which are 0.88 s and 1.14 s, respectively. The phase-separation further develops with annealing for 15, 30, and 45 min (Fig. 7.8 (c), (d), and (e)).

Figure 7.9 shows the results of T_{1H} experiments for rrP3DDT/$PC_{61}BM$ samples. The T_{1H} relaxation behaviors of the nonannealed rrP3DDT/$PC_{61}BM$ system are different from the above two systems; rrP3DDT and $PC_{61}BM$ are phase-separated already in the nonannealed samples on the size of 20–40 nm, as shown in Fig. 7.9. The phase-separation further develops by longer annealing time. The T_{1H} values of rrP3DDT in rrP3DDT/$PC_{61}BM$ system are 0.85, 0.84, and 0.81 s for 5, 15, and 30 min, respectively, and those of $PC_{61}BM$ are also 1.76, 1.84, and 2.04 s for 5, 15, and 30 min, respectively (Fig. 7.9(b)–(d)).

7.3.4. Optical and electrochemical properties of pure rrP3ATs, pure $PC_{61}BM$, and rrP3AT/$PC_{61}BM$ blends

Figure 7.10 shows UV-vis absorption spectra of pure rrP3ATs and pure $PC_{61}BM$. The influence of alkyl side-chain length on optical property is observed in Fig. 7.10 (a). A wavelength of maximum absorption (λ_{max}) in pure rrP3BT is 497 nm. The λ_{max} of rrP3HT and rrP3DDT are almost same, 517 nm. Vibronic progressions are found at ~550 nm and ~620 nm

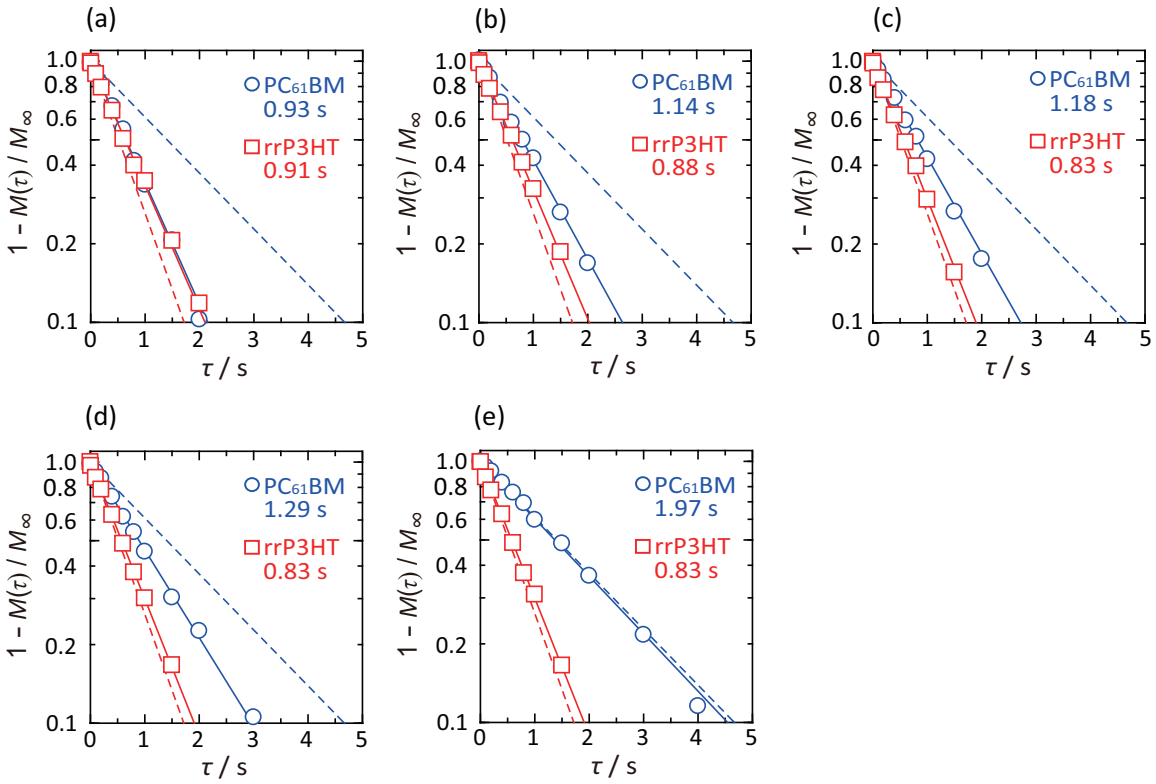

Fig. 7.8. T_{1H} relaxation behaviors of rrP3HT (open squares) and $PC_{61}BM$ (open circles) components in rrP3HT/$PC_{61}BM$ blends; (a) nonannealed, annealed at 150 °C for (b) 5 min, (c) 15 min, (d) 30 min, and (e) 45 min. T_{1H} values are written in each figures. T_{1H} relaxation behaviors of pure rrP3HT and pure $PC_{61}BM$ with annealed 150°C for 60 min are also shown as broken lines for references.

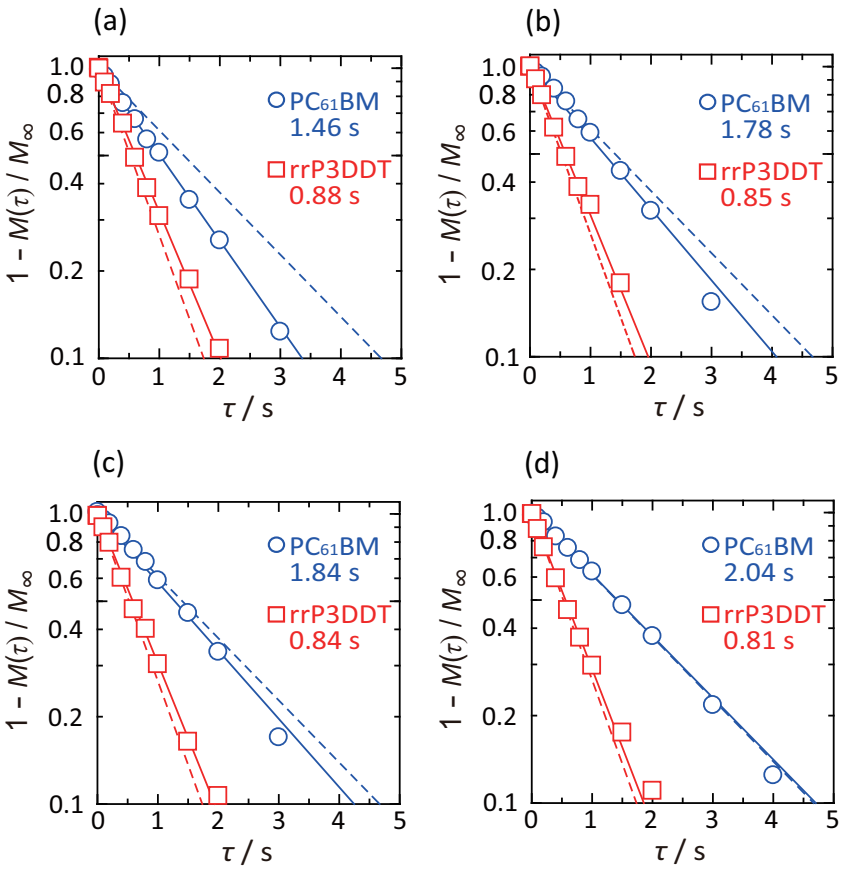

Fig. 7.9. T_{1H} relaxation behaviors of rrP3DDT (open squares) and $PC_{61}BM$ (open circles) components in rrP3DDT/$PC_{61}BM$ blends; (a) nonannealed, annealed at 150 °C for (b) 5 min, (c) 15 min, and (d) 30 min. T_{1H} values are written in each figures. T_{1H} relaxation behaviors of pure rrP3DDT and pure $PC_{61}BM$ with annealed 150°C for 60 min are also shown as broken lines for references.

for both the rrP3HT and rrP3DDT films. Pure $PC_{61}BM$ has absorption band in the wavelength of 200–550 nm. UV-vis absorption spectra of pure rrP3BT, pure rrP3HT, and pure $PC_{61}BM$ are unchanged irrespective of thermal annealing for 60 min (Fig. 7.10 (b), (c), and (e)). For pure rrP3DDT, vibronic progressions at ~550 nm and ~620 nm become clearer (Fig. 7.10 (d)). It was been reported that the vibronic progressions are caused by different π-conjugation length and the magnitude for inter-chain interactions [26, 27]. Energy gaps (Egs) for rrP3BT, rrP3HT, and rrP3DDT are estimated to be ~1.9 eV, and that for $PC_{61}BM$ is estimated to be ~2.2 eV using the absorption edges, respectively. Ips for nonannealed rrP3BT, rrP3HT, and rrP3DDT are estimated to be ~4.8 eV, and that for nonannealed $PC_{61}BM$ is estimated to be ~6.1 eV using AC-3, respectively. The Ips of rrP3ATs remain the same after annealing. In contrast, the Ip of $PC_{61}BM$ slightly decreases to 6.0 eV after annealing. From these results, the electron affinities (Eas) of rrP3ATs are estimated to be ~2.9 eV. The Eas of the nonannealed and annealed $PC_{61}BM$ are also estimated to be ~3.9 eV and ~3.8 eV, respectively.

Figure 7.11 shows the change of UV-vis absorption spectra of rrP3BT/$PC_{61}BM$, rrP3HT/$PC_{61}BM$, and rrP3DDT/$PC_{61}BM$ blend films by thermal annealing at 150 °C. For rrP3BT/$PC_{61}BM$ system (Fig. 7.11 (a)), the absorption spectra in the wavelength of 400–700 nm, which originate from rrP3BT (Fig. 7.10 (b)), change by annealing for 5 min; the vibronic progression appear at ~550 nm and ~600 nm. The absorption spectra remain the same up to 60 min of annealing. The absorption spectra in the wavelength of 200–400 nm, which originate from mainly $PC_{61}BM$ (Fig. 7.10 (e)), do not depend on the annealing time. An amount of light absorption (wavelength range of 400–700 nm) in rrP3BT/$PC_{61}BM$ films increases up to ~15 % by annealing. This is considered to be one of the reasons for improvement of the PCE by annealing. For rrP3HT/$PC_{61}BM$ system (Fig. 7.11 (b)), the light absorption in the wavelength of 400–700 nm increase by 5 min of annealing and remains the same up to 60 min of annealing.

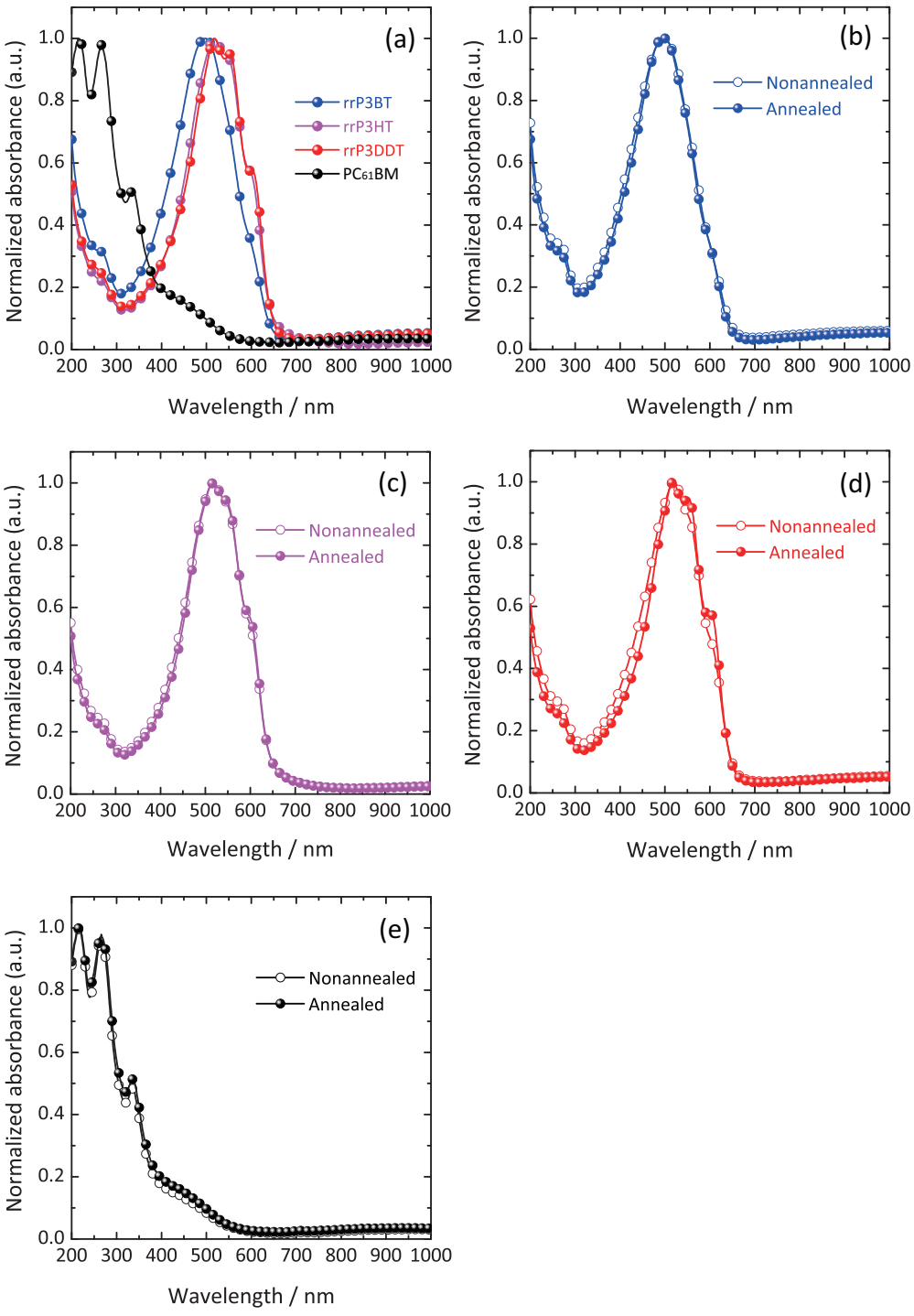

Fig. 7.10. (a) Normalized UV-vis absorption spectra of pure rrP3BT, rrP3HT, and rrP3DDT, $PC_{61}BM$ films with annealing at 150°C for 60 min. Change of UV-vis absorption spectra for (b) pure rrP3BT, (c) rrP3HT, and (d) rrP3DDT, and (e) $PC_{61}BM$ films with/without annealing at 150 °C for 60 min.

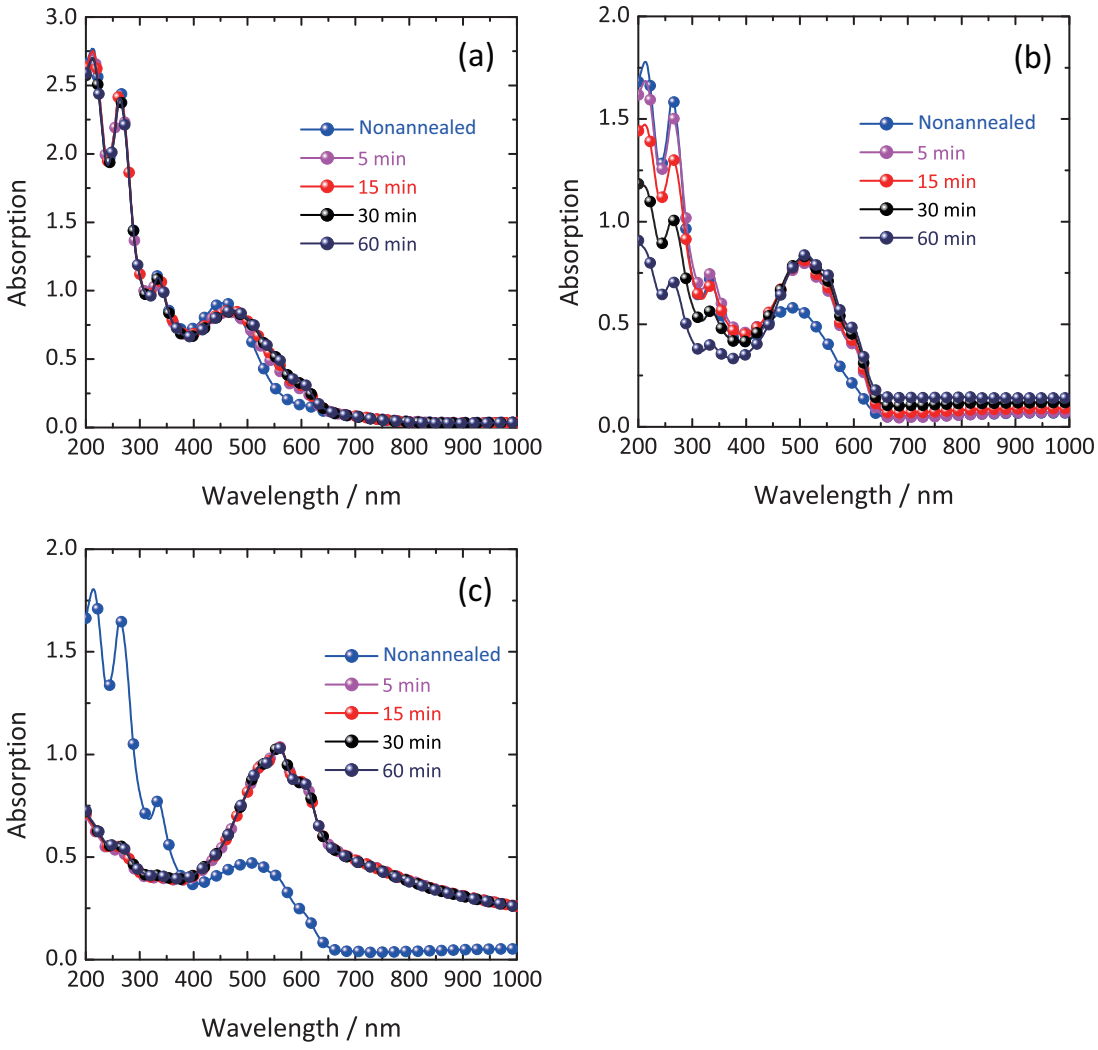

Fig. 7.11. Change of UV-vis absorption spectra for (a) rrP3BT/$PC_{61}BM$, (b) rrP3HT/$PC_{61}BM$, and (c) rrP3DDT/$PC_{61}BM$ blend films with annealing at 150 °C. The annealing times are shown in the figure.

The increment of light absorption by annealing is ~48 % in this wavelength range, which contributes the improvement of the PCE. The absorption of $PC_{61}BM$ in rrP3HT/$PC_{61}BM$ films in the wavelength of 200–400 nm decreases by annealing. However, the decrease does not affect the PCE value, because sunlight under AM 1.5G has wavelength range of 300–3000 nm and emits the highest intensity at the wavelength range of 400–700 nm. That is, the contribution of the light absorption of $PC_{61}BM$ on PCE is small. For rrP3DDT/$PC_{61}BM$ system (Fig. 7.11 (c)), the change of absorption spectra show a similar trend to the rrP3HT/$PCB_{61}M$ system; the light absorption by rrP3DDT increases, and that by $PC_{61}BM$ decreases by 5 min of annealing. The intensities between 700 and 1000 nm do not originate from optical absorption but optical scattering, because rrP3DDT/$PC_{61}BM$ films become translucent by the annealing.

7.3.5. Hole mobilities of rrP3ATs

To evaluate hole mobilities of rrP3ATs, we fabricated the hole only device consisting of ITO/PEDOT:PSS/rrP3AT/Al. The hole mobility can be estimated by a space charge limited current (SCLC) measurement [28-31]. SCLC is expressed as

$$J = \frac{9}{8}\varepsilon\varepsilon_0\mu_{\text{hole}}\frac{E^2}{L}, \tag{7.1}$$

where J is current density, μ_{hole} is hole mobility, E is the electric field, ε and ε_0 are the relative dielectric constant and the permittivity of the free space, respectively, and L is the thickness of the organic layer. Carrier mobility depends on the electric field. The dependence of electric field on carrier mobility is expressed as [32, 33]

$$\mu_{\text{hole}} = \mu_0 exp(\beta\sqrt{E}), \tag{7.2}$$

where μ_0 is the zero-field mobility and β is the Poole-Frenkel factor. From the combination of eqs. (7.1) and (7.2), the field dependence on carrier mobility under SCLC is expressed as

$$J = \frac{9}{8}\varepsilon\varepsilon_0 \frac{E^2}{L}\mu_0 exp(\beta\sqrt{E}). \tag{7.3}$$

This equation can be rewritten as

$$\ln\left(\frac{J}{E^2}\right) = \beta\sqrt{E} + \ln\left(\frac{9}{8}\varepsilon\varepsilon_0 \frac{\mu_0}{L}\right). \tag{7.4}$$

We estimate the hole mobility by fitting the slope of the $\ln\left(\frac{J}{E^2}\right) - \sqrt{E}$ plots, which are governed by SCLC. The fitted lines agree with the experimental data (Fig. 7.12). The μ_0 and β are given by the slope and intercept of fitted lines, respectively. The relative dielectric constant ε is presumed to be 3 [34] and the permittivity of the free space ε_0 is 8.85×10^{-14} C/cm. The field dependence of hole mobilities are obtained from the above fittings. The calculated parameters of μ, μ_0 and β are summarized in Table 7.4. The hole mobility of rrP3BT is almost equal to that of rrP3HT (~10^{-4} cm^2/Vs). In contrast, the mobility of rrP3DDT is one order of magnitude lower than that of rrP3HT. The β of rrP3BT, rrP3HT, rrP3DDT are estimated to be 1.5–2.1×10^{-3}. The μ_0 of rrP3BT and rrP3HT are close (4.1–4.2×10^{-5} cm^2/Vs). The μ_0 of rrP3DDT is lower (8.1×10^{-5} cm^2/Vs). The results indicate that low hole mobility of rrP3DDT is another origin of the low PCEs in the rrP3DDT/PC_{61}BM system.

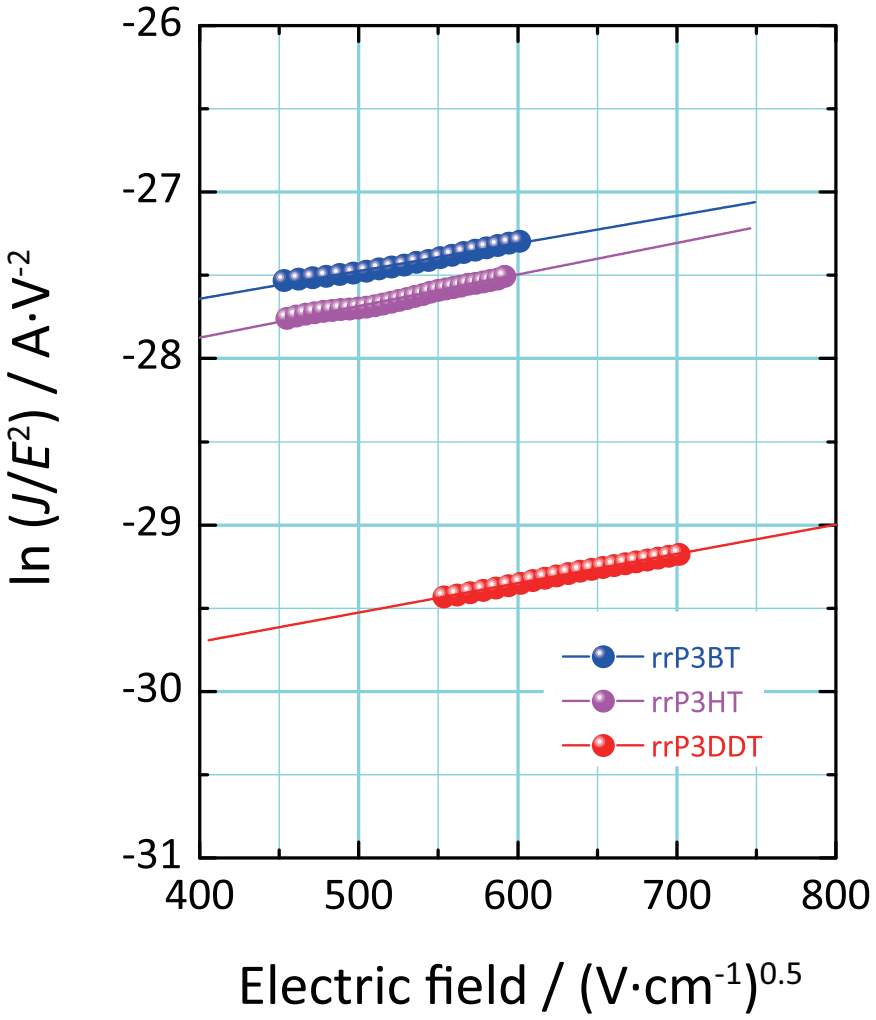

Fig. 7.12. Space-charge-limited currents for ITO/PEDOT:PSS/rrP3ATs/Al devices. The solid lines are fitted by SCLC theory.

Table 7.4. Zero field mobility, Poole-Frenkel factor, and hole mobility at 3.6 MV/cm of rrP3ATs.

rrP3ATs	μ_{hole} / $cm^2 \cdot V^{-1}s^{-1}$	β	μ_0 / $cm^2 \cdot V^{-1}s^{-1}$
rrP3BT	1.1×10^{-4}	0.0017	4.1×10^{-5}
rrP3HT	1.5×10^{-4}	0.0021	4.2×10^{-5}
rrP3DDT	2.0×10^{-5}	0.0015	8.1×10^{-6}

7.4. Conclusions

The effect of alkyl side-chain lengths in rrP3AT on photoelectric conversion characteristics and on donor-acceptor structures was investigated. For polymer BHJ solar cells in the rrP3BT/PC_{61}BM system, the PCEs change in two stages. The PCEs increase from 0.08 to 0.32 % and from 0.33 to 0.91 % with 5 and 45 min of annealing, respectively. From structural analyses, the increases of PCEs at 5 min and 45 min annealing for rrP3BT/PC_{61}BM system can be explained by structure ordering of rrP3BT and by phase-separation on the order of several tens of nanometers, respectively. Different from the two stage increase of PCEs for the rrP3BT/PC_{61}BM system, the rrP3HT/PC_{61}BM system provides only one stage increase (from 0.38 to 2.18 % by 5 min of annealing). The increase in the PCE for rrP3HT/PC_{61}BM system can be explained also by simultaneous occurrences, which is structure ordering of rrP3HT and PC_{61}BM and phase-separation. The rrP3DDT/PC_{61}BM system does not show any increase of PCEs; rather, decrease from 0.33 to 0.10 % by 5 min of annealing. This result is probably caused by the decrease in interfacial areas. From this study, it is found that the alkyl side-chain length significantly affects the donor-acceptor structures. The phase-separated structures

between rrP3AT and $PC_{61}BM$ on the order of several tens of nanometers are crucial factors to determine the performance of polymer BHJ solar cells

Acknowledgments

This study was conducted using the solid-state NMR spectrometer in the Joint Usage/Research Center (JURC) at the Institute for Chemical Research, Kyoto University.

References

[1] J.Y. Kim, S.H. Kim, H.H. Lee, K. Lee, W. Ma, X. Gong, A.J. Heeger, Adv. Mater., 18 (2006) 572.

[2] Y. Kim, S. Cook, S.M. Tuladhar, S.A. Choulis, J. Nelson, J.R. Durrant, D.D.C. Bradley, M. Giles, I. McCulloch, C.-S. Ha, M. Ree, Nat. Mater., 5 (2006) 197.

[3] D. Mühlbacher, M. Scharber, M. Morana, Z. Zhu, D. Waller, R. Gaudiana, C. Brabec, Adv. Mater., 18 (2006) 2884.

[4] P.W.M. Blom, V.D. Mihailetchi, L.J.A. Koster, D.E. Markov, Adv. Mater., 19 (2007) 1551.

[5] L.H. Nguyen, H. Hoppe, T. Erb, S. Günes, G. Gobsch, N.S. Sariciftci, Adv. Funct. Mater., 17 (2007) 1071.

[6] B.C. Thompson, J.M. Frechet, Angew. Chem., 47 (2008) 58.

[7] H.Y. Chen, J.H. Hou, S.Q. Zhang, Y.Y. Liang, G.W. Yang, Y. Yang, L.P. Yu, Y. Wu, G. Li, Nat. Photonics, 3 (2009) 649.

[8] S.H. Park, A. Roy, S. Beaupré, S. Cho, N. Coates, J.S. Moon, D. Moses, M. Leclerc, K. Lee, A.J. Heeger, Nat. Photonics, 3 (2009) 297.

[9] P.A. Troshin, H. Hoppe, J. Renz, M. Egginger, J.Y. Mayorova, A.E. Goryochev, A.S. Peregudov, R.N. Lyubovskaya, G. Gobsch, N.S. Sariciftci, V.F. Razumov, Adv. Funct. Mater., 19 (2009) 779.

[10] E. Verploegen, R. Mondal, C.J. Bettinger, S. Sok, M.F. Toney, Z. Bao, Adv. Funct. Mater., 20 (2010) 3519.

[11] P.M. Beaujuge, J.M. Frechet, J. Am. Chem. Soc., 133 (2011) 20009.

[12] T.Y. Chu, J. Lu, S. Beaupre, Y. Zhang, J.R. Pouliot, S. Wakim, J. Zhou, M. Leclerc, Z. Li, J. Ding, Y. Tao, J. Am. Chem. Soc., 133 (2011) 4250.

[13] Z. He, C. Zhong, X. Huang, W.Y. Wong, H. Wu, L. Chen, S. Su, Y. Cao, Adv. Mater., 23

(2011) 4636.

[14] L.Y. Lin, Y.H. Chen, Z.Y. Huang, H.W. Lin, S.H. Chou, F. Lin, C.W. Chen, Y.H. Liu, K.T. Wong, J. Am. Chem. Soc., 133 (2011) 15822.

[15] Y.Y. Liang, Y. Wu, D.Q. Feng, S.T. Tsai, H.J. Son, G. Li, L.P. Yu, J. Am. Chem. Soc., 131 (2009) 56.

[16] Z. Li, J.F. Ding, N.H. Song, J.P. Lu, Y. Tao, J. Am. Chem. Soc., 132 (2010) 13160.

[17] M. Helgesen, R. Søndergaard, F.C. Krebs, J. Mater. Chem., 20 (2010) 36.

[18] Z. Li, S.W. Tsang, X.M. Du, L. Scoles, G. Robertson, Y.G. Zhang, F. Toll, Y. Tao, J.P. Lu, J.F. Ding, Adv. Funct. Mater., 21 (2011) 3331.

[19] N. Camaioni, G. Ridolfi, G. Casalbore-Miceli, G. Possamai, M. Maggini, Adv. Mater., 14 (2002) 1735.

[20] F. Padinger, R.S. Rittberger, N.S. Sariciftci, Adv. Funct. Mater., 13 (2003) 85.

[21] M. Al-Ibrahim, O. Ambacher, S. Sensfuss, G. Gobsch, Appl. Phys. Lett., 86 (2005) 201120.

[22] W.L. Ma, C.Y. Yang, X. Gong, K. Lee, A.J. Heeger, Adv. Funct. Mater., 15 (2005) 1617.

[23] M. Reyes-Reyes, K. Kim, D.L. Carroll, Appl. Phys. Lett., 87 (2005) 083506.

[24] L.H. Nguyen, H. Hoppe, T. Erb, S. Gunes, G. Gobsch, N.S. Sariciftci, Adv. Funct. Mater., 17 (2007) 1071.

[25] M. Helgesen, R. Sondergaard, F.C. Krebs, J. Mater. Chem., 20 (2010) 36.

[26] J. Cornil, D. Beljonne, C.M. Heller, I.H. Campbell, B.K. Laurich, D.L. Smith, D.D.C. Bradley, K. Mullen, J.L. Bredas, Chem. Phys. Lett., 278 (1997) 139.

[27] J. Cornil, D.A. dos Santos, X. Crispin, R. Silbey, J.L. Bredas, J. Am. Chem. Soc., 120 (1998) 1289.

[28] M. Abkowitz, D.M. Pai, Philos. Mag. B, 53 (1986) 193.

[29] P.W.M. Blom, M.J.M. deJong, J.J.M. Vleggaar, Appl. Phys. Lett., 68 (1996) 3308.

[30] A.J. Campbell, D.D.C. Bradley, H. Antoniadis, M. Inbasekaran, W.S.W. Wu, E.P. Woo, Appl. Phys. Lett., 76 (2000) 1734.

[31] M. Giulianini, E.R. Waclawik, J.M. Bell, N. Motta, J. Appl. Phys., 108 (2010).

[32] G.G. Malliaras, J.R. Salem, P.J. Brock, J.C. Scott, Phys. Rev. B, 59 (1999) 10371.

[33] G.G. Malliaras, J.C. Scott, J. Appl. Phys., 85 (1999) 7426.

[34] T. Yasuda, Y. Yamaguchi, D.C. Zou, T. Tsutsui, Jpn. J. Appl. Phys., 41 (2002) 5626.

Summary

This thesis described the analysis of local and aggregated structures of materials for organic semiconductors mainly by solid-state NMR in order to understand the performance of the devices. The results and findings in the respective chapters are summarized as follows.

In Chapter 2, the local structure of an electron-transport and light-emitting material, tris(8-hydroxyquinoline) aluminum(III) (Alq_3), was analyzed by two-dimensional ^{27}Al multi-quantum magic-angle spinning (MQMAS) NMR experiments. Three crystalline Alq_3 samples in α-, γ-, and δ-Alq_3, and one melt-quenched amorphous sample (amorphous-Alq_3) were used in this chapter. From the MQMAS experiments, it is found that the γ- and δ-Alq_3 with blue photoluminescence (PL) emission consist of the facial isomers with well-defined local structures. In contrast, α- and amorphous-Alq_3 with green PL emission are found to consist of the meridional isomers with disordered local structures. It is also found that α-Alq_3 has distinct two sites. This is clearly different from the local structure of amorphous-Alq_3 consisting of a disordered single site. The difference has not been observed in standard ^{27}Al one-dimensional MAS and ^{13}C cross-polarization (CP)/MAS spectra. These studies demonstrate the availability of MQMAS experiments to clarify the local structures of organic materials.

In Chapter 3, organic light-emitting diodes (OLEDs) fabricated from three different types of Alq_3, α-Alq_3, δ-Alq_3, and a mixture of α-, γ-, and δ-Alq_3 (αγδ-Alq_3), were characterized. The α-Alq_3 and αγδ-Alq_3 powder samples show green PL emission before device fabrications, and the δ-Alq_3 powder sample exhibits blue PL emission before device fabrications. For the αγδ-Alq_3 powder sample, an energy transfer is found to occur from γ- and δ-Alq_3 domains to α-Alq_3 domains. Different from these powder samples, PL emissions were almost

indistinguishable for vacuum-deposited films prepared by the three types of Alq_3; all the maximum wavelengths are ~530 nm. The results suggest that some facial isomers in γ- and δ-Alq_3 become meridional isomers during Alq_3 are in the vacuum-deposited process, and that the isomeric state of Alq_3 in the vacuum-deposited films is predominantly the meridional state. Similarly with the PL emission, the electroluminescence (EL) spectra are also indistinguishable for the OLEDs fabricated from the three types of powder samples. However, EL efficiency of OLEDs depends on the Alq_3 crystalline polymorphs; the OLEDs fabricated from δ-Alq_3 and that from αγδ-Alq_3 demonstrated 1.1 and 1.4 times EL efficiency enhancements, respectively, compared with the case for α-Alq_3.

In Chapter 4, a sensitivity enhancement method in solid-state NMR is proposed. Solid-state NMR analysis for organic thin-film semiconductors is quite limited, although the analysis is considered to be useful to clarify the origin of device performance. The main reason is the low sensitivity of solid-state NMR compared to other analytical methods. To overcome this problem, a sensitivity enhancement method was investigated using paramagnetic relaxation. Copper phthalocyanine (CuPc), a commonly used carrier-injection material in OLEDs, was used for the paramagnetic reagent. Solid-state NMR experiments were carried out using CuPc/phenyldipyrenylphoshine oxide ($POPy_2$) bilayer thin films. $POPy_2$ has good carrier transport property and has often been used for OLEDs. By using CuPc layer, a 1.7 times ^{31}P CP/MAS signal enhancement is attained. This enhancement is comparable to that by the increase of the static magnetic field of NMR from 600 to 800 MHz (the enhancement factor is 1.5).

In Chapter 5, a formation condition of self-assembled monolayer (SAM) at indium-tin oxide (ITO) cathode/organic layer interface was investigated to improve the performance of OLEDs. The SAM formation of pentyltriethoxysilane (PTES) under acidic conditions

provides homogeneous coverage of silane layers on ITO substrates, which results in the improvement of hole-injection property from the ITO electrodes. This is in sharp contrast to the use of basic conditions, which results in inhomogeneous coverage of silane layers on ITO substrates and decrement of hole-injection property. Hole-injection property also depends on the H_2O/PTES ratios, r, and PTES concentration in a THF, C_{PTES}. The highest hole-injection was achieved when SAM formation was performed under r = 15 and C_{PTES} = 250 mM, with 0.01 M HNO_3 as a catalyst. The optimized SAM formation also improves the device performance of OLEDs.

In Chapter 6, the improvement of power conversion efficiency (PCE) in organic solar cells (OSCs) with isothermal annealing at 150 ºC was investigated by phase-separation analysis of solid-state NMR. Regioregular poly(3-hexylthiophene-2,5-diyl) (rrP3HT) and [6,6]-phenyl-C_{61}-butyric acid methyl ester ($PC_{61}BM$) were used as a donor and an acceptor, respectively. The donor-acceptor structures on the order of several nanometers and that of several tens of nanometers, which are considered to be related to the photoelectric conversion process, were analyzed by ^{1}H spin-lattice relaxation experiments in the rotating frame ($T_{1\rho H}$) and the laboratory frame (T_{1H}) in solid-state NMR, respectively. From $T_{1\rho H}$ experiments, it is found that rrP3HT and $PC_{61}BM$ are already phase-separated in the nonannealed film and remain unmixed irrespective of annealing times. From T_{1H} experiments, it is found that the donor-acceptor structures change from mixed to phase-separated states with 5 min of annealing. The analysis in this study demonstrates that the thermal annealing induces a structural change, which results in the formation of effective percolated carrier paths. The structural change contributes the improvement of PCE from 0.7 % to nearly 3 %.

In Chapter 7, the effect of alkyl side-chain lengths in poly(3-alkylthiophene-2,5-diyl) (rrP3AT) on the donor-acceptor structure in rrP3AT/$PC_{61}BM$ system during thermal annealing at

150 ºC was investigated by wide-angle X-ray diffraction (WAXD) and solid-state NMR experiments. As donors, three types of rrP3AT with different alkyl side-chain lengths were used: regioregular poly(3-butylthiophene-2,5-diyl) (rrP3BT), rrP3HT, and poly(3-dodecylthiophene-2,5-diyl) (rrP3DDT). From WAXD experiments, it is found that structure ordering of $PC_{61}BM$ in rrP3BT/$PC_{61}BM$ system does not develop irrespective of annealing times, although ordering of rrP3BT occurs by annealing only for 5 min. Different from the rrP3BT/$PC_{61}BM$ system, structure ordering of $PC_{61}BM$ as well as rrP3ATs occurs by 5 min of annealing for both of rrP3HT/$PC_{61}BM$ and rrP3DDT/$PC_{61}BM$ systems. From T_{1H} experiments in solid-state NMR, it is found that the phase-separations occur with 45 min and 5 min of annealing for rrP3BT/$PC_{61}BM$ and rrP3HT/$PC_{61}BM$ systems, respectively. For rrP3DDT/$PC_{61}BM$ system, the two constituents are already phase-separated in the nonannealed sample and remain unmixed irrespective of annealing times. The results show that longer alkyl side-chain length promotes phase-separation between rrP3AT and $PC_{61}BM$. Reflecting the structural change, PCEs change. For rrP3BT/$PC_{61}BM$ system, the PCEs change in two stages. The PCEs increase from 0.08 to 0.32 % and from 0.33 to 0.91 % with 5 min and 45 min of annealing, respectively. From the structural analyses, the increases of PCEs at 5 min and 45 min annealing for rrP3BT/$PC_{61}BM$ system can be explained by structure ordering of rrP3BT and by phase-separation on the order of several tens of nanometers, respectively. PCEs in rrP3HT/$PC_{61}BM$ system drastically increase from 0.38 to 2.18 % by 5 min of annealing. The increase in the PCE for rrP3HT/$PC_{61}BM$ system can be explained by simultaneous occurrences of structural ordering and phase-separation. The performance of rrP3DDT/$PC_{61}BM$ system is low compared to the above two systems; the PCEs decrease from 0.33 to 0.10 % with 5 min of annealing. This result is probably caused by the decrease in interfacial areas. The low carrier mobility of rrP3DDT is also the origin of the low PCEs in

the rrP3DDT/$PC_{61}BM$ system. From this study, it is found that the alkyl side-chains significantly affect the donor-acceptor phase-separated structures, which result in the change of photoelectric conversion characteristics.

List of Publications

Chapter 2

"Characterization of local structures in amorphous and crystalline tris(8-hydroxyquinoline) aluminum(III) (Alq_3) by solid-state ^{27}Al MQMAS NMR spectroscopy"

Yusuke Nishiyama, Tatsuya Fukushima, Kousuke Takami, Yasunari Kusaka, Toshio Yamazaki, and Hironori Kaji

Chemical Physics Letters 471 (2009) 80-84.

Chapter 3

"Green- and blue-emitting tris(8-hydroxyquinoline) aluminum(III) (Alq_3) crystalline polymorphs: Preparation and application to organic light-emitting diodes"

Tatsuya Fukushima and Hironori Kaji

Organic Electronics 13 (2012) 2985-2990.

Chapter 4

"Sensitivity boosting in solid-state NMR of thin organic semiconductors by a paramagnetic dopant of copper phthalocyanine"

Yusuke Nishiyama, Tatsuya Fukushima, Masashi Fukuchi, Subaru Fujimura, and Hironori Kaji

Chemical Physics Letters 556 (2013) 195-199.

Chapter 5

"Enhanced hole injection in organic light-emitting diodes by optimized synthesis of

self-assembled monolayer"

Yasuaki Tokudome, Tatsuya Fukushima, Atsushi Goto, and Hironori Kaji

Organic Electronics 12 (2011) 1600-1605.

Chapter 6

"Solid-state nuclear magnetic resonance analysis of phase separation behavior of regioregular poly(3-hexylthiophene) and [6,6]-phenyl-C_{61}-butyric acid methyl ester in bulk heterojunction organic solar cells"

Tatsuya Fukushima, Hironobu Kimura, Yurie Shimahara, and Hironori Kaji

Applied Physics Letters 99 (2011) [223301-1]-[223301-3].

Chapter 7

"Solid-state NMR analysis of donor/acceptor bulk heterojunction structures in organic solar cells: Importance of side chain lengths in donor polymers"

Tatsuya Fukushima, Subaru Fujimura, and Hironori Kaji

To be submitted

Other Publications

"Fusion of Phosphole and 1,1'-Biacenaphthene: Phosphorus(V)-Containing Extended π-Systems with High Electron Affinity and Electron Mobility"

Yoshihiro Matano, Arihiro Saito, Tatsuya Fukushima, Yasuaki Tokudome, Furitsu Suzuki, Daisuke Sakamaki, Hironori Kaji, Akihiro Ito, Kazuyoshi Tanaka, and Hiroshi Imahori

Angewandte Chemie International Edition 50 (2011**)** 8016-8020.

"Acenaphtho[1,2-c]phosphole P-oxide: A Phosphole-Naphthalene π-Conjugated System with High Electron Mobility"

Arihiro Saito, Tooru Miyajima, Makoto Nakashima, Tatsuya Fukushima, Hironori Kaji, Yoshihiro Matano, and Hiroshi Imahori

Chemistry - A European Journal 15 (2009) 10000-10004.

"Comparative study of the Synthesis, Structures, and Optical and Electrochemical Properties of Bithiophene-Fused Benzo[*c*]phospholes"

Yoshihiro Matano, Tooru Miyajima, Tatsuya Fukushima, Hironori Kaji, Yoshifumi Kimura, and Hiroshi Imahori

Chemistry - A European Journal 14 (2008) 8102–8115.

"Refined Structure Determination of Blue-Emitting Tris(8-hydroxyquinoline) Aluminum(III) (Alq_3) by the Combined Use of CP/MAS ^{13}C Solid-State NMR and the First-Principles Calculation"

Furitsu Suzuki, Masashi Fukuchi, Tatsuya Fukushima, and Hironori Kaji

To be submitted

"Investigation of aggregated structures in organic light-emitting diodes: approach from solid-state NMR"

Hironori Kaji, Tatsuya Fukushima, Masashi Fukuchi, Takeshi Komino, and Chihaya Adachi

Proceedings of SPIE, 8476 (2012) [84760F-1]-[84760F-5]. (Refereed Proceedings)

"Origin of the different emission wavelengths in Alq_3 analyzed by solid-state NMR"

Hironori Kaji, Tatsuya Fukushima, Kousuke Takami, and Yasunari Kusaka

Proceedings of SPIE, 6655 (2007) [665504-1]-[665504-10]. (Refereed Proceedings)

Acknowledgments

The studies presented in this thesis were carried out under the direction of Professor Hironori Kaji at Institute for Chemical Research, Kyoto University. The author would like to express his gratitude to Professor Hironori Kaji for his invaluable suggestion and kind guidance throughout the study.

Sincere appreciation is due to Dr. Yusuke Nishiyama, Dr. Masashi Fukuchi, and Dr. Yasuaki Tokudome for their active collaborations in this study. Thanks are also due to Dr. Toshio Yamazaki at RIKEN institute for his collaboration.

The author is grateful to Professor Hiroshi Imahori and Professor Hirofumi Sato, Department of Molecular Engineering, Graduate School of Engineering, Kyoto University, for their guidance in preparing this thesis.

Thanks are due to Associate Professor Atsushi Goto, Ms. Kyoko Ohmine, Ms. Ayaka Maeno, and Ms. Ruiko Iida, Institute for Chemical Research, Kyoto University, for their helpful advice and encouragement. The author acknowledges to his colleagues, Mr. Yasunari Kusaka, Mr. Kosuke Takami, Mr. Hironobu Kimura, Ms. Yurie Shimahara, and Mr. Subaru Fujimura, for their useful discussion and encouragement.

Thanks are also given to other staffs and students in Institute for Chemical Research, Kyoto University, for their kindness during this study.

This study was supported by a Grant-in-Aid for Scientific Research (A) (No. 21245044) and the Japan Society for the Promotion of Science (JSPS) through the “Funding Program for World-Leading Innovative R&D on Science and Technology (FIRST Program)” initiated by the Council for Science and Technology Policy (CSTP). This work is also supported by the New Energy and Industrial Technology Development Organization (NEDO) of the Ministry of

Economy, Trade, and Industry (METI). This study was conducted using the solid-state NMR spectrometer in the Joint Usage/Research Center (JURC) at the Institute for Chemical Research, Kyoto University.

Finally, the author heartily wishes to express his thanks to his parents, Hiromitsu Fukushima, Sachiko Fukushima, and all his relatives.

Tatsuya Fukushima